UNIVERSITÀ
DEGLI STUDI
FIRENZE

PhD in
Atomic and Molecular Photonics

CYCLE XXXIV

COORDINATOR
Prof. Diederik Wiersma

Reading and writing the neuronal activity: enhanced light-sheet microscopy and AOD-based volumetric photostimulation for all-optical applications

Academic Discipline (SSD) FIS/03

Doctoral Candidate
Pietro Ricci

Supervisor
Prof. Francesco S. Pavone
Francesco Saverio Pavone

Coordinator
Prof. Diederik Wiersma

Years 2018/2021

A Dante e Maddalena

Abstract

In recent years neuroscientists looked for optical systems enabling simultaneous imaging of extensive neuronal samples and cellular manipulation. For probing neuron activity, all-optical approaches are the most valuable alternative to traditional electrophysiology methods, which are limited by low-throughput, lack of cell-specificity and invasiveness. The main goal of this thesis is the implementation of a better solution for an all-optical interrogation of the brain of small mammals or zebrafishes. At the same time, I proposed several approaches to overcome common limitations inherent to the involved techniques.

For what concerns optical imaging, light-sheet fluorescence microscopy (LSFM) has become in the last decades a cornerstone technology. This technique improved image quality, contrast and acquisition speed with respect to other confocal-like alternatives, reducing sample photo-damage and photo-bleaching. However, images acquired with LSFM are often affected by light absorption or scattering effects, leading to uneven illumination and striping artifacts. In this thesis, I provided an optical solution to this problem, based on the use of an acousto-optical deflector (AOD). I implemented this device in a digital scanned laser light-sheet microscope to pivot the illumination beam along the beam propagation direction in front of the camera sensor. I also implemented a novel method to double the maximum attainable frame rate in confocal detection, exploiting the specific rolling shutter modality of our camera. The last parameter enhanced in LSM acquisitions was the fluorescence signal detected, by an evaluation of the effect of the excitation light polarization state over different fluorophore populations.

For what regards optogenetic manipulation, the state-of-the-art fastest scanning dynamics and the briefest refresh rate are provided by AODs. Nonetheless, their applicability to 2P photostimulation in large volumes has been limited by an efficiency inhomogeneity during axial scanning.

In this thesis, I presented a new method that allows increasing the power delivered to the different planes addressed. This approach has been used in a 2P AOD-based scanning setup to photostimulate an optogenetic actuator in zebrafish larvae. We demonstrated efficient axial scanning by observing uniform responses and activation probabilities from neuronal clusters addressed in the volume.

List of contents

List of figures

Relevant publications

Some of the thesis contents, artworks, figures and methods have been published also in the following research papers:

- **Ricci, P.**, Marchetti, M., Sorelli, M., Turrini, L., Resta, F., Gavryusev, V., de Vito, G. Sancataldo, G., Vanzi, F., Silvestri, L., Pavone, F.S., 2022. Power-effective scanning with AODs for 3D optogenic applications. J. Biophotonics e202100256. https://doi.org/10.1002/JBIO.202100256

- **Ricci, P.**, Gavryusev, V., Müllenbroich, C., Turrini, L., de Vito, G., Silvestri, L., Sancataldo, G., Pavone, F.S., 2021. Removing striping artifacts in light-sheet fluorescence microscopy: A review. Prog. Biophys. Mol. Biol. https://doi.org/10.1016/J.PBIOMOLBIO.2021.07.003

- **Ricci, P.**, Sancataldo, G., Gavryusev, V., Franceschini, A., Müllenbroich, M.C., Silvestri, L., Pavone, F.S., 2020. Fast multi-directional DSLM for confocal detection without striping artifacts. Biomed. Opt. Express 11, 3111. https://doi.org/10.1364/boe.390916

- de Vito, G., **Ricci, P.**, Turrini, L., Gavryusev, V., Müllenbroich, C., Tiso, N., Vanzi, F., Silvestri, L., Pavone, F.S., 2020. Effects of excitation light polarization on fluorescence emission in two-photon light-sheet microscopy. Biomed. Opt. Express 11, 4651. https://doi.org/10.1364/boe.396388

- Gavryusev, V., Sancataldo, G., **Ricci, P.**, Montalbano, A., Fornetto, C., Turrini, L., Laurino, A., Pesce, L., de Vito, G., Tiso, N., Vanzi, F., Silvestri, L., Pavone, F.S., 2019. Dual-beam confocal light-sheet microscopy via flexible acousto-optic deflector. J. Biomed. Opt. 24, 1. https://doi.org/10.1117/1.jbo.24.10.106504

1. Preface

The main goal of neuroscience is to discern and interpret brain functions in healthy and diseased conditions. Over one billion people worldwide are affected by neurological disorders and their consequences, according to the World Health Organization[1]. Among the others, ischemic stroke - a neurological deficit that affects 15 million people worldwide every year - is one of the leading causes of long-term disability and represents one of the major causes of death. Improvements in the understanding of the mechanisms and risk factors have contributed to preventing vascular and infectious diseases of the nervous system. For addressing most of the other neurological diseases, it is still necessary to develop new scientific and epidemiological techniques to establish therapies and interventions. To address this challenge, experimental and theoretical analyses are nowadays continuously dealing with quantitative and qualitative insights on individual neurons or clusters[2–4]. However, the whole human brain mapping, and the comprehension of its inner functional mechanisms are still extremely ambitious goals to reach due to the high number of cells and the large scale that characterizes this organ. For example, in an adult, about a hundred billion neurons are distributed over an extended volume of around 1300 cm^3. The neural puzzle and the accessibility are naturally simpler in different model organisms that involve much fewer neurons and interconnections[5–7]. Furthermore, understanding the neuronal mechanisms of vertebrates and mammals and correlating them to pathological conditions and environmental surroundings is helpful to clarify typical human neural dynamics[8]. For example, zebrafish are commonly used as study subjects because they share about 70% of the human genome and most of the neurotransmitters, with a quite similar nervous system architecture[9,10]. The knowledge acquired on these model organisms therefore could be transposable on humans. In addition, even if advanced optical imaging techniques have been recently applied to *ex vivo* human brain tissues[11,12], these procedures cannot be straightforwardly adopted *in vivo*, for up-scaling technical complications and the optical inaccessibility of the structures.

Even though the complexity and the scale dimensionality are reduced in the mentioned models, to disentangle the causality between neural activation of specific networks in dislocated areas and triggered external behaviours, researchers need appropriate instruments and methods of investigation[13].

In this regard, patch-clamp electrophysiology is one of the most used and versatile tools for understanding the electrical dynamics in individual isolated living cells, tissue sections, or cell membrane[14,15]. In particular, this technique is especially diffused for the study of excitable cells such as neurons where the transmembrane ionic currents can be measured by recording the voltage difference, in form of action potentials.

On the other hand, each patch has to be applied by means of a different microelectrode directly on the cellular membrane, making this method highly invasive for the tissue. This steric hindrance and the numerically limited applicability of the patch clamps made necessary the development of novel technologies in the last years, opening to new application scenarios through the advance in high-resolution imaging and optogenetic photostimulation[16–18]. These so-called all-optical electrophysiology practices are indeed the most promising approach to shed light on the field, being not invasive for those model animals which allow optical, genetic and neurophysiological approaches *in vivo*[19,20]. Moreover, those methods responded to a call of an approach able to be highly selective while simultaneously ensuring the access to large areas within the brain. For this reason, those all-optical techniques properly combine specific reporters for neuronal electrical activity and optical tools for cell photostimulation.

In particular, the time-scale of the neuronal events dictates the need for calcium indicators that allow to monitor fast functional processes and to record synaptic inputs[21–23]. Nonetheless, to exploit the potentialities of calcium imaging and visualize cellular structures with high resolution and contrast, or to capture fast events *in vivo*[24,25], further advancements have been required also in optical methods of investigation, such as laser scanner microscopy.

A turning point involving both imaging and photostimulation is represented by the adoption of the multiphoton excitation in the sample illumination process[26–28]. With respect to one-photon excitation (1PE), two-photon (2P) illumination has provided unprecedented results in biological samples observation and stimulation, pushing further the optical access[29] and improving the spatial resolution to submicrometric standard[30–32].

On behalf of optical imaging, the full potential of optogenetics stimulation and genetically encoded photosensitive tools resides rather in eliciting neuronal signals and modulating global activity by addressing light directly on specifically targeted neurons[33,34]. By combining novel genetic tools with the optical access and selectivity achieved today in advanced microscopy, several light-based cell perturbation experiments have been proposed[16,35–37].

In light of the above considerations, the first chapter of the following introduction regards the advantages carried by the two-photon excitation processes in optical microscopy applications. At this point, a particular imaging technique is introduced - the light-sheet fluorescence microscopy (LSFM)[38–41] - together with a discussion about its superior technical benefits provided in the neuroscience panorama with respect to other standard microscopes. LSFM common practices and problems have been described, especially focussing on three aspects, then faced and detailed all through the thesis: the striping artifacts generally present in this kind of microscopy and the possible solutions; the contrast enhancement obtained by implementing a confocal detection; the effect of the illumination light polarization on the signal detection.

To conclude the optical imaging section, the last part looks inside the features and uses of calcium indicators in imaging applications from a spectroscopic point of view.

Subsequently, optogenetics and genetically encoded photosensitive tools mechanisms have been illustrated, explaining how they are involved in photostimulation experiments. Finally, the state-of-the-art of light-addressing methods has been reported, summarizing the main applications and the major limitations affecting these practices. Regarding this, commonly adopted scanning methods suffer from slow dynamics and long refreshing rates for the illumination pattern modulation. This performance can be drastically enhanced by acousto-optic deflectors (AODs), to which is completely dedicated the last section of the introduction, highlighting their potentialities in several imaging applications and quasi-simultaneous cell stimulation.

2. Optical imaging and LSFM

Advanced optical imaging capabilities are required to better understand neuronal mechanisms at the microscopic level by selecting single cells deep in the brain. Anatomical 3D reconstruction with subcellular resolution and whole-brain functional analysis are some of the greatest goals for microscopists working in neuroscience. Thus, novel developments in imaging methods are crucial for better observation and deeper analysis of the biological processes.

Optical microscopy is nowadays one of the reference methods to have insights within the tissues and capture fast dynamics events in a non-invasive fashion. In particular, fluorescent markers and fluorescence microscopy became essential tools for researchers interested in quantitative investigation and selective imaging of such biological processes *in-vivo*[42]. Fluorescence microscopy results extremely useful in this field since the specificity in selecting and labelling only the desired targets.

However, commonly used confocal microscopy techniques guarantee only limited optical access in biological tissues, low contrast and signal-to-noise ratio (SNR) because of the out-of-focus fluorescence contributions not intrinsically avoided during imaging. A turning point is represented by the introduction of the two-photon microscopy, which pushed up these technical limits improving optical imaging performance. As further developed in the next chapter, this approach exploits the two absorption effect for fluorophores excitation offering several advantages without resorting to advanced illumination schemes[7,43–47].

Then, in order to reconstruct the sample entirely, optical sectioning is then performed. For this purpose, frequently in confocal microscopy, a light beam is focussed on the sample and then translated, scanning the whole field of view (FOV). However, the resulting point scanning approach results too slow to image the whole brain. LSFM represented a game-changer in this regard, solving this drawback and reducing sample photodamage.

2.1. Two-photon microscopy

In the last years of the millennium, two-photon microscopy changed optical microscopy[48], exceeding precedent limits of tissue optical depth penetration and image contrast[28,49–51]. However, the two-photon absorption (TPA) - the phenomenon at the base of this game-changer - was originally predicted by Maria Goeppert-Mayer in 1931[52] and verified for the first time in tests over europium-doped crystal[53].

The TPA is a non-linear process involving the simultaneous molecular absorption of two photons, a phenomenon characterized by a low probability proportional to the square of the light intensity of excitation. As shown in **Fig.2.1_1a**, in order to generate a two-photon transition to the excited state of a fluorophore, two quanta carrying half of the energy level difference are required. That corresponds to two photons having a double wavelength with respect to the one which would excite the transaction alone, i.e., as in the linear absorption process. For this reason, the wavelengths adopted in this kind of microscopy rely often on the near-infrared region (NIR).

Since the low probability of triggering this non-linear process, a high photon density is required to initiate the process. In particular, there are two requisites to enhance the two-photon excitation (TPE) of a molecule from its ground state: the temporal and spatial confinement of light excitation. For the temporal confinement, femtosecond pulsed lasers are particularly suited, concentrating a high number of photons in short time intervals. On the other hand, spatial confinement is easily achieved by focussing light through a high numerical aperture (NA) optical lens or an objective. Consequently, the excited fluorescent dyes will be probabilistically only those confined to the focus, where the photon spatial density is maximum. **Fig.2.1_1b** shows those requirements schematically.

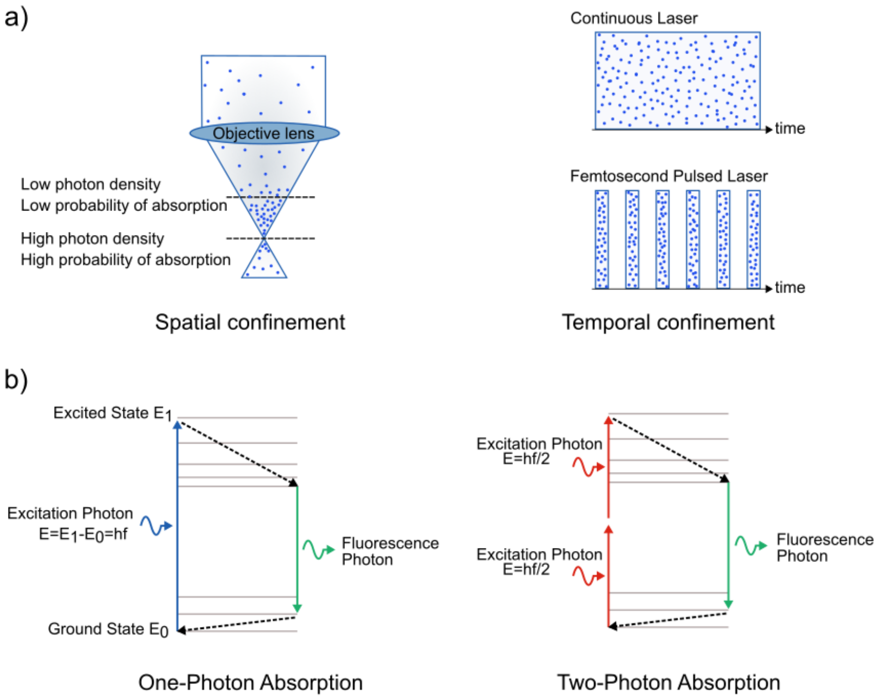

Figure 2.1_1: Two-photon absorption and fluorescence. **a)** The difference between one-photon and two-photon excitation processes stands on the number of photons simultaneously absorbed by the molecule to achieve the electronic transition between the ground state E_0 and the proper excited state E_1. In the former case, the energy gap is provided by means of only one photon carrying the energy of $E=E_1-E_0$, while in the second case the jump is covered by the simultaneous absorption of two photons carrying half the energy (at double wavelength). After molecular vibrational relaxation (black arrows) a new photon carrying less energy is emitted at a different wavelength. **b)** The spatial confinement guaranteed by the light focussing through the objective provides high photon density spatially; the temporal confinement can be achieved with femtosecond pulsed lasers where a high number of photons are concentrated in short time intervals. Both the processes increase the quantum probability of multiphoton absorption.

The advantages carried by TPE are numerous[54]. First of all, in fluorescence microscopy it is of notable importance to filter out background fluorescence contributes that come from out-of-focus areas. Moreover, a prolonged and unnecessary excitation of these areas can cause photobleaching and photodamage throughout the specimen, which can cause significant problems, especially in live samples.

The problem arises from the light that passes through a high NA objective illuminating a conic volume before converging in a small spot in the focus. If several fluorescent spots are distributed at different axial positions, they all will be excited similarly, even those outside or before the focal plane. These spots will result defocused and blurred, contributing to a reduction in the contrast and details in the image taken. Those terms do not encode indeed any spatial information.

In order to divide the source of the different responses throughout the volume, the sample is optically separated into slices by optical sectioning. In standard confocal microscopy this is achieved by directing the emission light through a tiny aperture, or pinhole, placed in the detection path before a sensing element that records the signals. The pinhole allows removing all emissions not originating from the focal plane, filtering the out-of-focus contributes.

In contrast, TPA releases from the need for a confocal pinhole in the light path. Since the excitation intensity falls outside the focus, and the probability of TPA goes with the square of excitation intensity, also the fluorescence intensity will fall, by a corresponding quadratic factor. For these reasons, the TPE is particularly used for optical sectioning and high contrast imaging with respect to other linear excitation strategies. In addition, in contrast to confocal microscopy, Due to a low probability of photon absorption, TP microscopy provides lower photobleaching and phototoxicity above and below the plane of focus, resulting less perturbing to live samples.

Another aspect that is important to highlight, is that by going deeper within the sample, the excitation intensity tends to decrease by the scattering - the deviation of ballistic photons caused by light-matter interaction. In confocal microscopy many photons are absorbed before reaching the target, decreasing the excitation intensity at greater imaging depths. Under TPE, no intermediate absorption will occur, and thus the full excitation power will reach the focus, increasing image depths.

Furthermore, even though the scattered photons provide a reduction of the amount of fluorescence generated at the focus, none of the scattered light will provide TPE, because of the low probability of the process. Indeed, there is a quasi-zero chance that two excitation photons will be deviated to the same position at the same time, necessary to generate the TPA.

On the other hand, the scattering affects also the emitted photons, but all the fluorescence signals generated at the focus can be collected with no limitations because carrying the right spatial information.

Ultimately, it is well known that in Rayleigh light scattering there is a strong dependency on the illumination wavelength[55]. In detail, the scattered light results inversely proportional to the fourth power of the light's wavelength ($1/\lambda^4$). Thus, the use of a longer wavelength, rather than visible ones typically used in linear excitation methods, usually reduce the scattering.

In this regard, a certain range of NIR illumination (between 650 nm and 1200 nm) matches a particularly biological window where autofluorescence is low and haemoglobin, water, and protein absorption are depressed. Nevertheless, due to the light absorption of the material (e.g., water absorption increased in IR), it is not always valid the correlation between larger optical penetration with longer excitation, but a wavelength trade-off between the two processes has to be researched.

2.2. Light-Sheet Fluorescence Microscopy

Light-sheet fluorescence microscopy (LSFM) revolutionised optical imaging since the nineties[56] to be then widely used in several high-resolution observations[57,58], from fast cellular processes[40,59] to long-term biological dynamics[60,61], embryonic development[62–66] and large scale mapping of neuronal projections[67].

With respect to confocal microscopy, LSFM allows much faster data collection, higher SNR and reduced sample photodamage[68], together with a higher axial resolution even with moderate NA optics[69]. In this approach, a thin sheet of light is projected through the sample in the focal plane of the detection objective[70]. The light sheet is commonly generated employing a cylindrical lens[71] or by rapidly scanning a light beam[72] (digitally scanned laser light-sheet fluorescence microscopy - DSLM).

As schematically represented in **Fig.2.2_1**, the detection direction is orthogonal with respect to the illumination plane, combining an intrinsic optical sectioning excitation scheme with a wide-field detection. As a result, the fluorescence is excited only in a thin slice, consequently achieving a high SNR and imaging contrast, while simultaneously reducing photo-damage and photo-bleaching of the remaining parts, differently from confocal microscopy.

In LSFM the illumination and detection paths result entirely decoupled from each other, such as the radial and axial resolution achievable. Indeed, assuming an illumination with Gaussian beam, in a LSFM the radial and axial point spread functions (PSFs) are respectively[73]:

$$PSF_{radial} = \frac{0.61 \cdot \lambda_{em}}{NA_{det}} \qquad (2.2\_1) \qquad\qquad PSF_{axial} = \frac{0.63 \cdot n \cdot \lambda_{ill}}{NA_{ill}} \qquad (2.2\_2)$$

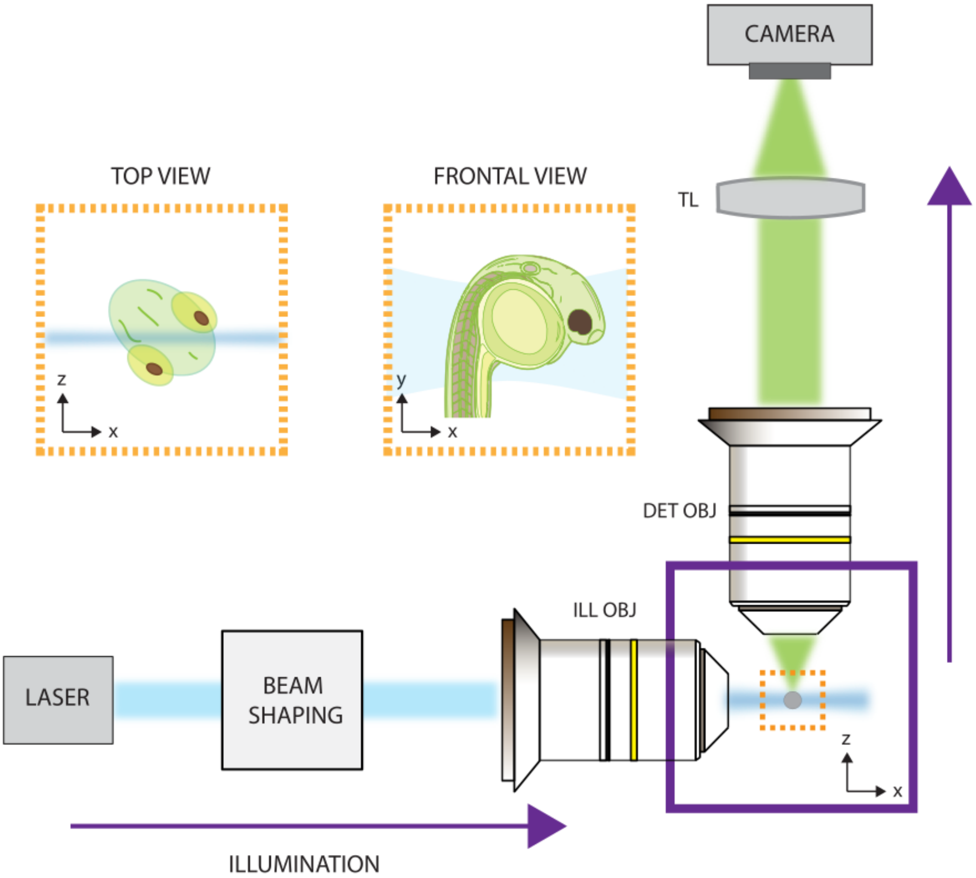

Figure 2.2_1: Optical Scheme of LSFM. In light-sheet microscopy, the illumination and the detection are split into two separate light paths. The illumination axis is perpendicular to the detection axis. An objective lens is used to collect fluorescence from the complete field of view and maps it on a camera. Modified from[74].

Where λ_{em} and λ_{ill} are respectively the fluorophore emission wavelength and the laser illumination wavelength; n is the medium refractive index; NA_{det} and NA_{ill} are the numerical apertures of the detection objective and illumination objective respectively. Then, depending also on the sample geometry, objectives with different NA_{det} and NA_{ill} are often used, with optimized working distances.

With this particular illumination conformation, for each camera exposure, this technique produces 2D images of the sample, which is usually placed in the overlapping area of illumination and detection focus. To acquire three-dimensional image stacks and reconstruct the entire sample, the relative position of the observation volume is translated. The collected signal is usually recorded by a multi-pixel detection device, as a CCD or a sCMOS camera.

To further increase the image contrast, confocal detection has been introduced in LSFM (CLSFM)[75–77]. Like in DSLM, for this method the light sheet is usually created by rapidly scanning a Gaussian beam in front of the detection area and, differently from a widefield detection, the emitted fluorescent signal is recorded through a confocal slit placed in the detection path.

With scientific complementary metal-oxide-semiconductor (sCMOS) cameras, this slit can be obtained by exploiting the line-by-line sensor readout, nowadays commonly implemented. In detail, in rolling shutter mode, a line-by-line exposition is provided by activating single or few rows of pixels simultaneously, as a function of the integration time. The active slit then rolls up and down sequentially covering the whole sensor. Confocal detection is reached by properly synchronizing the rolling virtual slit with the light beam position and scanning rate: the sequential pictures acquired are then finally fused to reconstruct the whole image. In such a way, it is possible to collect fluorescence contributes only from corresponding illuminated areas.

This approach is fundamentally different from another widely exploited modality - the global shutter mode - where all photosensors displaced on the matrix of pixels of the camera are simultaneously activated at once for widefield acquisitions.

Today, in typical sCMOS cameras there are two rolling shutters, one for each half of the sensor; in **Fig.2.2_2** the different sCMOS acquisition modalities are schematically shown and compared. However, in most DLSM setups a single beam is scanned by a galvanometric mirror. This requires the use of a single rolling shutter moving from the top to the bottom of the sensor (or vice versa) to obtain confocal detection, leading to a halving of the maximum frame rate.

This limitation becomes important when investigating fast events such as calcium transients or very large volumes but can be overcome by generating two independent parallel light-sheets within the field of view (FOV) and by synchronizing them with the two rolling shutters.

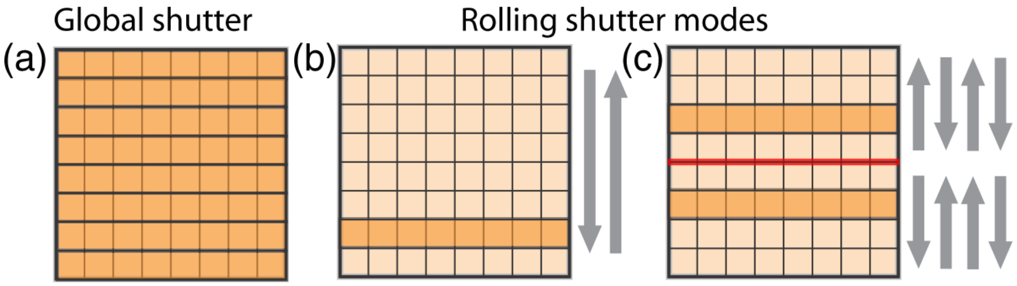

Figure 2.2_2: CMOS image acquisition schemes. **(a)** In global shutter mode all pixels are exposed at once (orange colour), while in **(b)** single- or **(c)** dual rolling shutter modes only one or two sets of neighbouring pixel rows are concurrently active, before sequentially enabling the next ones in the direction indicated by the arrows. The red line in (c) demarcates the sensor halves. Modified from[78].

In conclusion, in account of the mentioned benefits, the relative implementing simplicity and the outstanding performance, LSFM has been adopted with no distinction for imaging of thin and extended samples such as fruit flies, larval fish, and small mammals[79]. In this regard, for thick and large specimens, chemically treatments are commonly required before the volumetric acquisition, by means of specific optical clearing methods to reduce refractive index mismatch within the sample[80–82].

2.2.1. Striping artifacts in LSFM

Despite the multiple mentioned benefits attributed to LSFM, conventional light sheet-based techniques suffer from a drawback, commonly indicated as striping. Those artifacts appear in the collected images as shadows – or stripes indeed – all along the illumination direction. The presence of such artifacts is intrinsic of this excitation scheme, deriving directly from the side illumination of samples. The striping arises from scattering and/or absorption of light by small structures (e.g., impurities, air bubbles, erythrocytes or pigmentation spots) along the single-side illumination light path, occluding the light sheet and leading to uneven exposure and reduced fluorescence, as shown schematically and experimentally in **Fig.2.2.1_1a** and **Fig.2.2.1_1b** respectively.

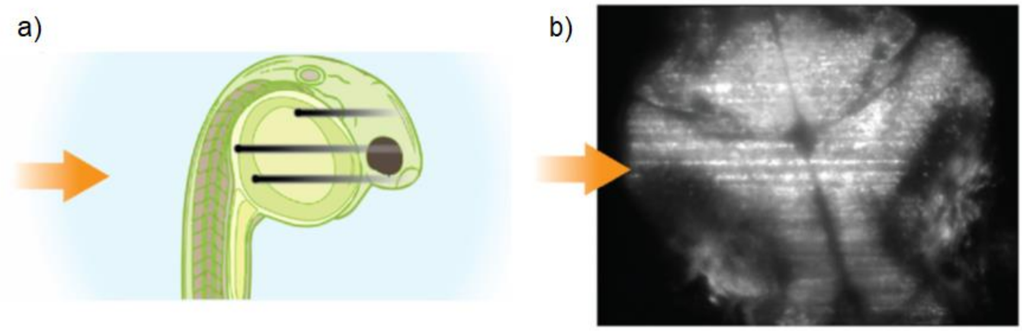

Figure 2.2.1_1: Striping artifacts. **(a)** Cartoon of a typical sample containing optically opaque structural elements illuminated by a single-side illumination approach. Inhomogeneities in the sample (represented by small black dots) lead to artifacts and alterations in LFSM images, resulting in shadows/stripes. **(b)** Typical one-photon LSFM image of a zebrafish larva where striping artifacts and shadowing are visible. The arrow indicates the direction of light propagation. Modified from[74].

Usually, scattering is more relevant in living specimens, where the refractive index is naturally inhomogeneous, while in ex vivo samples, clearing methods can be used to reduce these scattering effects[81]. However, light absorption by natural pigments is not affected by most clearing methods[83].

However, both in live and clarified specimens, the size of scatterers/absorbers is typically quite larger than the wavelength of the illumination laser since the stripes appear visible in spite of the diffraction-limited resolution of the microscope. Consequently, such stripes contribute to poor image quality and lower the SBR. Since these shadows hide relevant information, the image analysis, time-correlation investigation, functional mapping and monitoring of biological processes can be negatively affected by striping. Reducing the fluorescence variations and spurious features observed during detection allows avoiding incorrect quantitative conclusions or mistakes in biological activity studies.

To mitigate or remove these artifacts, in the last decade, different methods and effective solutions have been proposed[74], including fully optical approaches, computational post-processing techniques or a hybrid combination of both.

When Gaussian illumination is employed in LSFM, the beam propagates straight in the sample impinging on the obstacles. Otherwise, if the light entered tilted enough through the sample the beam would be able to surmount the obstacle and recover the spatial information hidden behind. Hence, several strategies aim to increase the angular diversity of the beam propagation. The two pure optical solutions which more promisingly faced this drawback are the Bessel beams and multidirectional illuminations.

The former solution has been demonstrated to be successful to attenuate striping attenuation[84]. In addition to being easily implementable[85,86], Bessel beam brought several advantages for optical microscopy as increased resolution isotropy and an extended depth of field[87–89]. The transverse intensity distribution of Bessel beams is described by concentric rings[90]. This defines a peculiar conical propagation that guarantees to the beam a sufficient angular dispersion. Indeed, since this conic propagation, external rays will be able to overcome the obstacles. Hence, except if the obstacle has too large dimensions, the Bessel beam – or self-reconstructing beam – can reform after a small distance, recovering a uniform propagation intensity.

The second most used solution to alleviate the problem is the light sheet pivoting – or multidirectional illumination[91] – where the beam is made swung[91] in the detection focal plane. In this regard, several approaches have been proposed aiming at fast pivoting dynamics[92,93].

Indeed, to average out efficiently the shadows over time and to result in an enhanced uniform illumination, the beam must rotate at a much larger rate compared to the framerate of the imaging camera.

Commonly to each optical method, they do not require any data post-processing to remove the stripes from the images, at the only cost of a hardware implementation which often requires specific optical designs, sometimes demanding and expensive (e.g., galvo-mirrors, AODs).

Alternatively, artifact correction provided by digital elaboration can be applied to any microscopy setup since it can be carried out in post-processing. Moreover, competitive results with the ones obtained with pure optical methods have been shown[94–96].

However, the integration of the image processing pipeline is not always straightforward and the handling and processing of terabyte-sized datasets, as often produced by LSFM, is time- and hardware-expensive.

For what concerns hybrid solutions, which require both hardware and software modifications to face the striping, it is worth mentioning the multiview fusion approach[97]. With this technique, the sample is volumetrically imaged from different angles by means of a mechanical rotator stage. Volumes from each view are then merged to create an improved comprehensive representation of the sample, and recover information typically obstructed in single side illumination.

Dedicated fusion and deconvolution algorithms are required to fuse together the images in a high-resolution volume with improved SNR[98]. However, even if the overall merged image quality is greatly enhanced compared to single view methods this technique is strongly limited by the acquisition rate caused by the slow rotation speed of stage motors, and by photobleaching since the sample is cumulatively exposed to several illumination sessions.

In conclusion, the biological scope of the research should drive the choice of the method to be implemented in LSM to suppress the striping. For instance, imaging fast in-vivo biological processes require approaches that do not impair the measurement rate and cause increased photobleaching.

On the other hand, such methods are perfectly suitable approaches for imaging slowly evolving systems or obtaining structural reconstructions of fixed ex-vivo samples.

2.2.2. Effect of polarization in LSFM

The polarization state of the excitation light plays a significant role both in 1P[99] and 2P[100] absorption and emission processes exploited in microscopy[101–103], especially in LSFM[104], where the illumination and detection directions are forced to be orthogonal. Indeed, the fluorescence emission from single dipoles is spatially anisotropic and preferentially orthogonal to the excitation dipole transition moment[105].

As already seen for 2P excitation, the fluorescence phenomenon can be described into two steps separated in time. First of all, the molecule absorbs one or more incident photons going into the excited state. After the time delay necessary for molecular relaxation to its lowest excited level, the spontaneous emission of a single photon occurs, usually carrying lower energy. If the emission is assumed to be incoherent with no phase correlation preserved, these two phenomena and the effects of polarization on them can be discussed separately[106]. Under this hypothesis, the fluorescence intensity from a single molecule results proportional to the simple product between the N-photon absorption probability and the emission probability:

$$I^N \propto P_{Abs}^N \cdot P_{Em} \qquad (2.2.2\_1)$$

Where the proportionality coefficient contains only efficiency and normalization factors. In turn, the N-photon absorption probability for a two-level system can be expressed as:

$$P_{Abs}^N \propto \left|\vec{\mu}_{ge} \cdot \vec{E}_{Ex}\right|^{2N} \qquad (2.2.2\_2)$$

where the dot denotes the scalar product between the polarization direction of the excitation electric field $\vec{E}_{Ex}$ and the absorption transition dipole moment between the molecular ground state and the excited state $\vec{\mu}_{ge}$.

Now, considering that the incident intensity is $I_{Ex} \propto \left|\vec{E}_{Ex}\right|^2$ and calling θ the angle between the polarization of the exciting electric field and the dipole moment of the molecule, it results that the 2P absorption probability is proportional to[106]:

$$P_{Abs}^{2} \propto \left|\vec{\mu}_{ge}\right|^{4} I_{Ex}^{2}\, cos^{4}(\theta) \qquad (2.2.2\_3)$$

The dependency on the angle encodes the polarization effect, which is referred to as angular photoselection: absorption is most likely if the direction of the electric field of the photons is aligned with the absorption transition dipole. This probability is steered towards narrower distributions for multi-photon processes (see N photons dependence expressed in **Eq.2.2.2_2**), meaning that the photoselection effect is more pronounced in 2P microscopy with respect to 1P.

Another difference stands between the light polarization types used to illuminate the sample. In the case of 2P excitation, the sum of angular momenta of the absorbed photons is required to be zero, since the total angular momentum change related to the electronic state transition is null. It is more probable to fulfil this condition with linear rather than circular polarization, leading to a higher excitation rate, because in the former configuration there is a 50% probability for the fluorophore to interact with photons with opposite handedness that can reciprocally compensate their angular momenta.

For what concerns the emission probability of a single photon along a certain observation direction $\hat{\imath}$, it can be related to the emitted intensity I_{Em} or equivalently to $\left|\vec{\mathrm{E}}_{\mathrm{Em}} \cdot \hat{\imath}\right|^{2}$. $\vec{E}_{Em}$ is the emanated field by the molecular emission dipole between an excited state and the ground state μ_{eg}. Since this field comes from the radiation from the dipole source, its component along the propagation direction k will be

$E_{Em}(k) \propto k \times (k \times \mu_{eg}) = \mu_{eg}^{\perp}$, where $\mu_{eg}^{\perp}$ is the projection of the emission dipole on the direction perpendicular to the emission direction k[106].Then it follows:

$$P_{Em}(\hat{\imath}) \propto \left|\mu_{eg}^{\perp} \cdot \hat{\imath}\right|^{2} \qquad (2.2.2\_4)$$

It means that the emitted field is distributed anisotropically, presenting a cylindrical symmetry relative to the emission dipole moment orientation axis. Consequently, both the degree of polarization and radiation intensity will be highest in the plane orthogonal to this symmetry axis and zero in the parallel direction.

It is important to note that μ_{em} and μ_{ab} can be different, involving different states and molecular conformations. However, here it's assumed that these dipoles are along the same orientation excluding any rotational process between the two processes.

Finally, combining the absorption and emission probabilities, we can conclude that the 2P fluorescence intensity from a single molecule along the observation direction $\hat{\imath}$ is proportional to[106]:

$$I^{2} = \left|\mu_{eg}^{\perp} \cdot \hat{\imath}\right|^{2} \left|\vec{\mu}_{ge}\right|^{4} I_{Ex}^{2} \, cos^{4}(\theta) \qquad (2.2.2\_5)$$

Combining the excitation photoselection effects due to polarized illumination and the cylindrically symmetric output distribution related to the emission dipole moment.

In LSFM, the orthogonal geometry between the excitation and detection optical axes makes the presence of this anisotropy even more significant, as depicted in three different configurations in **Fig.2.2.2_1**. In the described configuration, the best performance in terms of signal detection was expected when all the fluorophores have their dipole moment oriented all along the $\hat{y}$ axis and the excitation light polarization is strictly polarized along the same axis **(c)**. In this case, indeed, all fluorophores will be excited, but due to the cylindrical symmetry of the dipole emission, they will emit mostly in the $\widehat{xz}$ plane and the fluorescence will reach the camera.

The photoselection effect induced by linearly polarized excitation light, effective on the population of excited dyes, would affect the emitted fluorescence direction. Thus, it could be beneficial to experimentally orient the polarization orientation of excitation light to maximize the light emitted toward the direction of the detection objective in a LSM maximizing the fluorescent intensity collection.

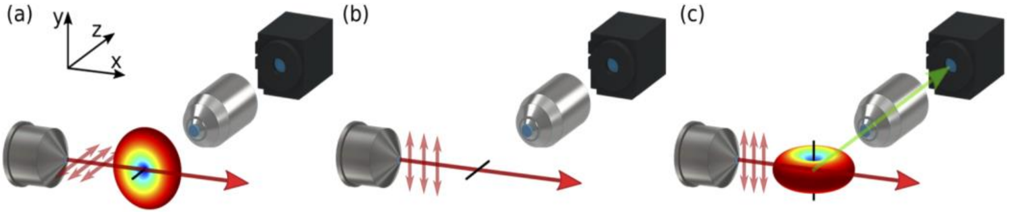

Figure 2.2.2_1: Schematic of the polarization-dependent effects in 2P LSM. **(a)** It assumes a fixed orientation of the fluorophore transition dipole moment (black line) and the linear polarization plane (indicated by short red arrows) both aligned with the detection axis; the fluorophores are excited, but the fluorescence light (coloured distribution) is emitted predominately on the xy-plane. **(b)** If the polarization plane of the excitation light is parallel to the y-axis while the transition dipole is perpendicular to it, then no fluorescence light is generated. **(c)** If both the polarization plane and the transition dipole are aligned with the y-axis, then the fluorescence light is emitted predominately on the xz-plane and therefore part of it (green arrow) can be collected by the detection objective (on the z-axis). Modified from[104].

Finally, within a material (solid, liquid or gas) every molecule can be oriented differently, ranging from a co-aligned condition, as in a crystal, to a fully random angular distribution, as in a non-viscous liquid or ideal gas. The photoselection will entail that only the fraction of fluorophores with a non-zero projected component of their absorption transition dipole moment along the illuminating beam polarization direction will be excited. However, the cumulative fluorescent signal detected by the objective in a LSFM is the sum of all the molecule emission patterns. Even though the excitation light is polarized, the rotational diffusion of the molecule affects the dipole fluorescent emission direction - or fluorescent depolarization -. The typical lifetime τ between the photon absorption and the subsequent fluorescent emission is on the order of 1÷10 ns, a time interval where the molecule can undergo the rotational diffusion and a Brownian motion caused by thermal interaction with the environment. This effect can be evaluated quantitatively considering the macroscopic properties of the solution where the molecules are embedded. The fluorescent anisotropy is introduced in the following[105]:

$$r = \frac{I_{\parallel} - I_{\perp}}{I_T} \qquad (2.2.2\_6)$$

As the ratio between the different components of the intensity of the emission field, parallel or perpendicular to the polarized excitation respectively, and the total intensity emitted. In particular, the measured fluorescent anisotropy *r* can be related proportionally to the fundamental anisotropy r_0 at t=0 following Perin's equation[105]:

$$r = \frac{r_0}{1+\frac{\tau}{\alpha}} = \beta \cdot r_0 \qquad (2.2.2\_7)$$

Where τ is the fluorescent lifetime and α is the rotational correlation time, in turn, defined as:

$$\alpha = \frac{\eta V}{RT} \qquad (2.2.2\_8)$$

Where η is the viscosity, T is the temperature, V is the volume of the rotating unit and R is the gas constant. This equation indicates that small molecules diluted in a low viscosity medium can rotate very rapidly (10÷100 ps timescales), completely randomizing the emission distribution toward an isotropic pattern. On the other hand, rotational diffusion is limited in viscous media, by large molecular size or by strong inter-molecular bounding to a much larger structure. For instance, for a protein like the GFP with a molecular weight of 27 kD has an expected rotational correlation time near to 10 ns.

2.3. Calcium imaging and indicators

Calcium ions (Ca^{2+}) play an important role in several cellular and neuronal functions[107]. This cation is the major actor in numerous intracellular processes, such as the hormone secretion and the releasing of neurotransmitters from synaptic vesicles[108,109]. In addition, Ca^{2+} can be used also as an indicator of cellular activity[110]. The relative calcium concentration within the cell is highly dynamic due to the presence of pumps that selectively transport these ions in and out of the cell in response to a variety of signals. The calcium flux that accompanies these processes in living cells can be optically monitored by imaging of calcium indicators[111], synthetic molecules that change their properties following intracellular calcium concentration.

To understand how calcium indicators work, it is important to define their molecular structure[112]. Those are modified chelator molecules that are composed of two main parts. The first is the chelator site that selectively binds calcium ions, while the second is a fluorescent site. A fluorescent molecule - or fluorophore - can absorb specific excitation light once illuminated and then, in turn, emit light at different wavelengths. The binding of calcium to the indicator alters its fluorescence properties, which provides a way to quantify the relative changes in calcium concentration. Thus, by collecting the emitted fluorescent signals and registering the intensity difference, calcium imaging allows measuring the intracellular activity[113].

In the last fifty years, these indicators have been continuously developed to improve their intrinsic properties[114], selectivity and calcium affinity. One of the main advancements in this field concerns the development of genetically encoded calcium indicators (GECIs), currently used worldwide for imaging applications, thanks to their non-invasiveness and selective cell labelling[23,115]. Furthermore, GECIs are widely exploited for their easy expression through virus-delivery methods[22]. It is also possible to create transgenic animals[116] expressing the indicator in all cells or selectively in certain cellular subtypes, making those tools extremely selective and useful for activity analysis.

A GECI deserving a particular mention is the GCaMP family[21,117]. GCaMPs are proteins realized by the synthetic fusion of a calmodulin (CaM) domain, a calmodulin-binding domain and a circularly permutated green fluorescent protein (GFP), commonly excited at 480 nm, with an emission peak at 510 nm. **Fig.2.3_1** shows schematically how the GCaMP indicators work while binding calcium ions. In the absence of Ca^{2+}, the GFP chromophore stands in a protonated state with minimal fluorescence intensity. In presence of calcium ions, the CaM module binds the ions (forming Ca^{2+} - CaM complex) and undergoes a conformational change; then the complex binds, in turn, the calmodulin-binding domain. As a result, the chromophore is deprotonated, making the two GFP halves closer. Finally, once excited, it will result in a brighter emitted fluorescence.

This tool has been used for both *in vitro* and *in vivo* applications to measure increases in intracellular Ca^{2+} in neurons in several animal models, including mice and zebrafish[118].

For example, this indicator has been used for large-scale neural recordings to map whole-brain activity[2,119]. Being the molecular fluorescence characterized by fast dynamics, this technique is particularly exploited to investigate the highly synchronous network activity of hundreds of neurons and their inner correlations[120].

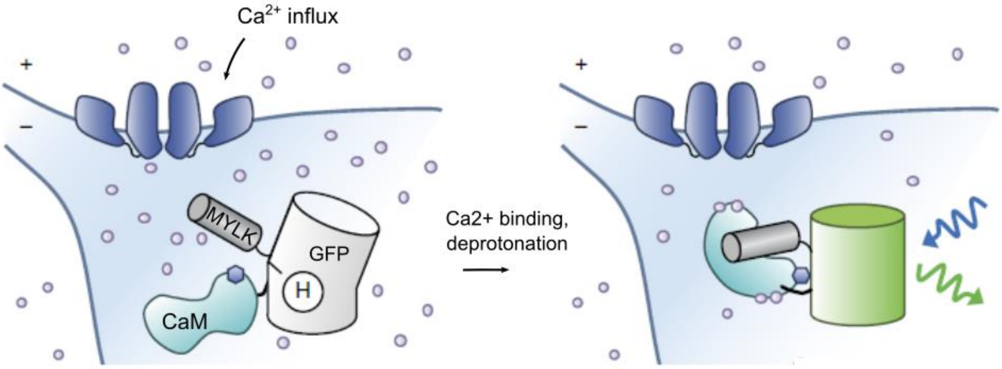

Figure 2.3_1: GCaMP structure and working mechanism. GCaMP consists of three main domains: a calmodulin-binding domain (or myosin light-chain kinase domain, MYLK, dark grey complex), a calmodulin domain (CaM, light blue complex) and a GFP domain in the centre (first light grey and then green complex, in the middle. Upon Ca^{2+} binding, the calmodulin domain undergoes a conformational change and tightly binds to the MYLK binding domain. Then fluorophore then is deprotonated (it loses the hydrogen H) making the two GFP halved closer. It results in a brighter fluorescence once excited with proper light wavelength. Adapted with permission from[121].

3. Optogenetics and optical manipulation

3.1. Optogenetic actuators

Optogenetics represents today an essential tool for non-invasive cell manipulation, combining the potentialities of genetic engineering and the technological advancements in optical stimulation[16]. This interdisciplinary approach enables the use of light to control the activity of genetically modified neurons. Indeed, these transmembrane proteins - called opsins - work as light-opened ion channels. In detail, when the opsin is illuminated with proper wavelength, the channel changes conformation leading to ions transition, as shown in **Fig.3.1_1**. In other words, these neurons are made photo-responsive, allowing their activation or inhibition with an external light trigger[34]. In this field, examples of specific optogenetic actuators used for neuromodulation are Channelrhodopsins[122–124] and Halorhodopsins[125].

This optogenetic approach allows to overcome the common constraints of neuronal electrophysiological stimulation methods in living tissues and freely moving animals. Indeed, the use of electrodes or clamps is strongly invasive and limiting when a large neuronal population has to be addressed. Furthermore, through the use of proper targeting mechanisms, genetic manipulation techniques guarantee the selectivity required to manipulate only specific neural populations cell-type defined[126].

By photostimulation, it has been demonstrated the optogenetic control of well-defined biochemical events within behaving animals[16,17]. In this regard, to stimulate superficial brain areas such as the cerebral cortex, optical fibers or light-emitting diodes (LEDs)[127] have been applied directly to the skull of small mammals. Nonetheless, other optical approaches are required to deliver light deeper in the sample and in dislocated areas. Light targeting science is indeed an open research field, looking for improved stimulation flexibility and optimized modulability for simultaneous - or near-simultaneous - stimulation of several cells. To ensure a fast control of neural circuits by optogenetic activation, light addressing strategies must be developed to achieve the required temporal resolution. This time bottleneck for photostimulation is biologically determined by the time required to photoactivate optogenetic actuators and proper kinetics (5÷30 ms)[128].

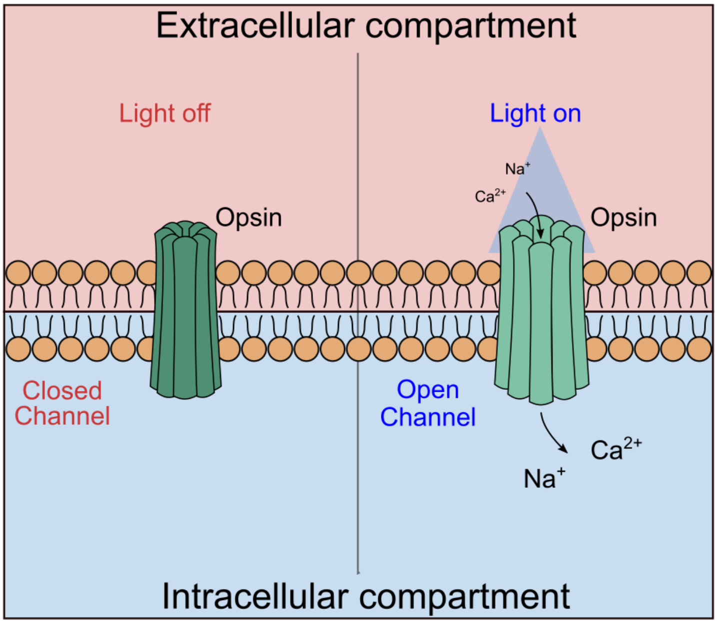

Figure 3.1_1: Optogenetic activation mechanism. Genetically modified neurons can express opsins in the transmembrane domain. Once excited by a specific wavelength, those light-sensitive proteins change their morphological conformation allowing the transition of Ca^{2+} in the intracellular compartment. The voltage difference triggers the action potential transmission and the neuronal cell activation.

Anyway, the continuous improvements in light-base cell perturbation methods not only regard the temporal dynamics. Even if the optogenetic activation dynamic is independent - or at least not strictly correlated - on the number of targets simultaneously addressed, the capability of addressing multiple cells or of quickly jumping between different targets would help to open interesting neuroscience scenarios. For instance, this capacity would enable the probing of the causal role of specific action potential patterns in defined populations processing fast biological sygnals[129,130].

3.2. Optical manipulation methods

Several optical approaches of light targeting have been developed in the last years. However, mechanical constraints, low efficiency in light delivery and slow dynamics have often limited the applicability of several devices in optogenetics. For example, galvanometer mirrors (GMs) are mainly used in 1P optogenetic investigations[3,131] because strongly affected by their mechanical inertia (tens of micrometers in ∼100 μs[132]). Indeed, GMs are employed rarely in 2PE photostimulation experiments, essentially for slow 2D raster scans[133]. It is because their slow sweeping rate[16] make them not suited to rapidly access neurons spanning over extensive volumes. A possible solution is represented by the use of resonant scanners to increase the temporal resolution but due to their resonant cycling, they cannot provide the necessary flexibility for arbitrary excitation trajectories, like spiral scans. Alternatively, GMs require to be coupled to other optical devices, such as spatial light modulators (SLM), to obtain concurrently patterned distributions[36].

An unspecific stimulation approach is represented by the wide-field-based illumination, where at the cost of the spatial selectivity, all the volume is illuminated at once, exciting all together target and nontarget cells. In this regard, several steps forward have been moved to parallelize the light delivery and to address light to preselected target regions at once. The main difference with respect to a widefield illumination is illustrated by the cartoon reported in Fig.3.2_1.

Multisite stimulation is obtained by means of intensity or phase modulation of a coherent beam. In detail, light amplitude modulation concerns the selective blocking of off-target illumination. On the other hand, the phase modulation approach is more efficient because the design and the modulation of the light pattern are easily obtainable by redirecting the beam.

Particularly, many early parallel photostimulation experiments adopted micro-LEDs[127], digital micromirrors devices (DMSs)[134,135] or liquid crystals displays (LCD)[136]. However, even if they guarantee fast refresh rates (~kHz) all of these share the general drawback of poor stimulation efficiency when addressing sparsely distributed targets.

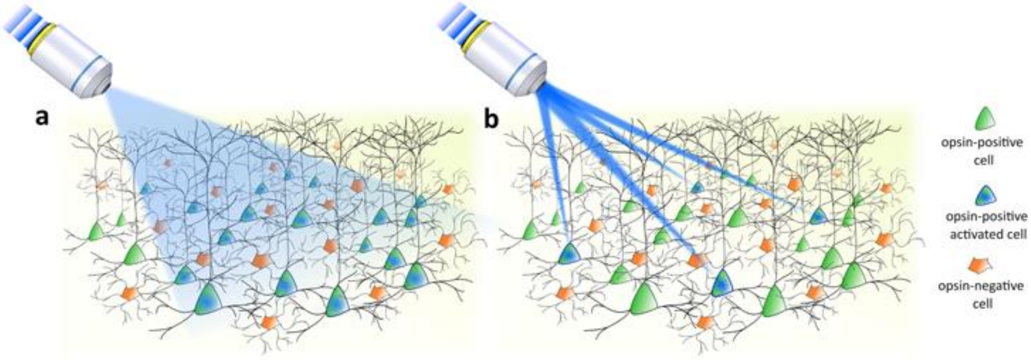

Figure 3.2_1: Optical approaches for optogenetic stimulation. **(a)** Cell-type genetically targeted investigations enabled by all opsin-expressing neuron activation via wide-field illumination. **(b)** Targeted investigations are enabled by selective activation of a specific pool of neurons via parallelized light-targeting strategies. Adapted with permission from[16]

Conversely, efficient light stimulation has been demonstrated with other parallel illumination methods as computer-generated holography (CGH)[137], which takes advantage of liquid-crystal-based spatial light modulators (LC-SLMs). Here, a Fourier-based iterative algorithm is usually exploited to compute desired phase pattern, subsequently sent to a LC-SLM that modulates the phase of the input beam wavefront. The so modulated light pattern is then redirected to the back pupil of the objective and finally, the light is focused onto the sample with the desired template. However, the iterative modulation of the wavefront phase intrinsically generates speckle patterns at the sample plane, affecting the precision of the light targeting. This effect is especially pronounced in 2P CGH since 2PE photoactivation is proportional to the square of the excitation intensity[16].

Alternative 2P optogenetics applications have been achieved with precise control of speckle-free light distribution with an interferometric method called generalized phase contrast (GPC)[138].

Commercially available SLM-based instruments offer a maximum refresh rate of 100 Hz. This fits the time bottleneck for continuous optogenetic stimulation, i.e. the optogenetic actuator closing rate (10÷100ms)[128]. However, the opening rate is usually faster (1÷2ms)[128]: thus, the use of SLM limits the possibility of studying the dynamics of neuronal circuits by stimulating multiple actuators. Furthermore, this approach shares with the other parallel illumination techniques a low efficiency, since the laser power is split among all preselected targets[20]. Anyway, the power levels commonly needed for photostimulation experiments are easily available with high-power commercial laser sources, allowing in principle the simultaneous addressing of large numbers of cells under 2PE. However, the maximum power that could be delivered to the sample – and thus the maximum number of addressable spots – is limited by the heating damage threshold[139]. Indeed, by increasing the number of targets illuminated at once, the total energy released on the sample is increased as well, enhancing the sample photodamage probability. In addition, the limited refresh rate of SLM prevents customizing the radiation delivery time to reduce phototoxicity.

Moreover, a faster dynamic could be necessary also for closed-loop experiments, in which the displayed stimulation pattern should be updated in real-time response to the dynamics of the neuronal circuit or other experimental feedback. For instance, coupling these photostimulation methods to a whole-brain imaging system would allow understanding the causality between optogenetic activations and outcome behaviours recorded by calcium imaging.

3.3. Random access illumination with acousto optic deflectors

Acousto-optic deflectors (AODs) represent one of the most valuable alternatives to improve the stimulation refresh rate with respect to all the aforementioned techniques[140]. This technology can be used to rapidly sweep the light beam and change its focusing without any mechanical movement or intrinsic inertia[141], reaching MHz-order dynamics and potentially fulfilling the temporal requirements for the concurrent activation of spatially distributed neurons.

Indeed, even if AODs cannot reach the simultaneity guaranteed by parallel approaches, in the latter methods the rate for the illumination pattern reconfiguration is at least two orders of magnitude worse (ms) than the dwell time obtainable with AODs (10-30 µs). For this reason, by using AODs a quasi-simultaneous activation of multiple targets is potentially achievable within the same time required by a parallel approach to perform an equivalent stimulation pattern.

Most importantly, the AOD response time is constant, as it does not depend on whether subsequent points are contiguous or not. Thus, AODs provide high precision and reproducibility in beam positioning, offering high flexibility in targeting non-sequential regions of interest (ROIs), enabling 3D random-access scanning. With AOD is possible to make the light jump between distant spots or to generate independent multiple beams, by using rapidly changing or multiple synchronous radio-frequencies (RF) to drive them[92,142,143]. In this regard, AODs are conveniently used for imaging applications involving subsequent multisite neuronal activity recording, which require near-microsecond temporal resolution[25,144–149].

The fundamental mechanism of light deflection of an AOD resides on a periodical change of the refractive index of its internal crystal. It is induced by a propagating sound wave, created by an oscillating piezo at a frequency of MHz[27]. The transparent crystal behaves like an optical grating, which diffracts an impinging laser beam (first diffracted order). A residual undiffracted beam will pass straight instead (zero diffracted order).

When the piezo of the AOD is driven by a single frequency, it allows controlling the deflection and the intensity of a single beam. Interestingly, when the piezo is driven by multiple frequencies, the crystal behaves like a linear combination of gratings, allowing it to generate simultaneously different beams from a single one. Each beam can be independently regulated in terms of spatial direction and intensity.

In the case of a single driving frequency, since the light interaction with the crystal can be described as the one with a diffraction grating, the first-order angle of deviation will be[150]:

$$\theta = \frac{\lambda}{\Lambda} = \frac{\lambda f}{v} \qquad (3.3\_1)$$

Where λ is the laser wavelength and Λ is the acoustic wavelength, that can be written in terms of sound frequency f and velocity v (**Fig.3.3_1a**). In this case, since the frequency addressed to the AOD is static, even if the light beam has a finite transversal extension, usually filling the whole optical aperture of the crystal, all the different portions of the spot will be deflected of the same amount.

However, if the driving frequency changes in time, the same will do the sound wave while interacting with the impinging light and the whole optical beam will be deflected differently. Thus, if the driving frequency is $f(t)$, it will make the deflection to be time-dependent $\theta(t)$. The effect can be described instantaneously as a function of the time t and position x in the AOD crystal where the sound wave is travelling:

$$\theta(x,t) = \frac{\lambda}{v} \cdot f\left(t - \frac{x}{v}\right) \quad (3.3\_2)$$

Where $x=0$ is the centre of the crystal. Now, if the frequency linearly changes as:

$$f(t) = f_{min} + \alpha t \qquad (3.3\_3)$$

Where α is the slope - or chirp - of the ramping frequency and f_{min} is the lowest value of the frequency bandwidth, it follows:

$$\theta(x,t) = \frac{\lambda}{v} \cdot (f_{min} + \alpha t) - \frac{\lambda\alpha}{v^2} x \qquad (3.3\_4)$$

The first term indicates how the central propagation axis sweeps between a minimum deflection angle $\theta_{min} = \frac{\lambda f_{min}}{v}$ at the beginning of wave propagation at *t=0* up to $\theta(t) = \frac{\lambda f(t)}{v}$ at time *t*. The second term describes a converging cylindrical lens with a focal length of $F = \frac{v^2}{\lambda\alpha}$. So, the focal length can be fully determined by the chirp parameter, but the central optical axis results time-varying when the AOD is driven with a chirped frequency, determining a lateral drift (**Fig.3.3_1b**). To counterpose this effect and have a stable focus in space, a counterpropagating sound wave has to interact with the beam at the same time driving a second AOD with an analogous chirped frequency $f_2(t)=f_1(t)$, synchronized with the first one (**Fig.3.3_1c**). It is important to note that telecentrically relaying the two AOD apertures, the deflection angle generated by the second device will be geometrically inverted with respect to the first one. The total deflection affecting the impinging beam results to be:

$$\theta(x,t) = \frac{\lambda}{v}\left[-f_1(t + \frac{x}{v}) + f_2(t - \frac{x}{v})\right] \qquad (3.3\_5)$$

Now recalling **eq.3.3_3** and substituting the terms, it results:

$$\theta(x,t) = -\left(\frac{2\lambda\alpha}{v^2}\right) x \qquad (3.3\_6)$$

Completely cancelling the lateral shift. This cylindrical lens has now a central propagation axis and a focal length stable in time. If we introduce the ramping time of the chirped frequency Δt_{chirp} and the frequency bandwidth Δf, such that $\alpha = \frac{\Delta f}{\Delta t_{chirp}}$ the focal length can also be described as follows:

$$F_{AOD} = \frac{v^2}{2\lambda\alpha} = \frac{v^2}{2\lambda} \cdot \frac{\Delta t_{chirp}}{\Delta f} \qquad (3.3\_7)$$

However, in this way, there is no control in the lateral light addressing. Thus, let's introduce a frequency off-set, such that $f_1(t) = f_{min} + \alpha t + f_1^{offset}$ and $f_2(t) = f_{min} + \alpha t + f_2^{offset}$. Inserting those expressions in **Eq.3.3_2**, the deflection generated by the two AODs globally reads:

$$\theta(x,t) = -\left(\frac{2\lambda\alpha}{v^2}\right)x + \frac{\lambda}{v}(f_2^{offset} - f_1^{offset}) \qquad (3.3\_8)$$

Here, the second term indicates the induced light beam lateral deflection, completely independent of the focal length and the axial focal position. It is also possible to set properly the offset frequencies of $f_1(t)$ and $f_2(t)$ to reformulate **Eq. 3.3_8** as:

$$\theta_{Lateral} = \frac{\lambda}{v}(f_{2C} - f_{1c}) \qquad (3.3\_9)$$

Where f_1c and f_2c are the center acoustic frequencies of the ramp sent to the first and second deflectors, respectively.

To summarize, with two AODs is possible to control independently the lateral deflection in one direction and the axial positioning of the beam. To extend to three dimensions, other two additional AODs are required, respectively telecentrically relayed (for a total of four).

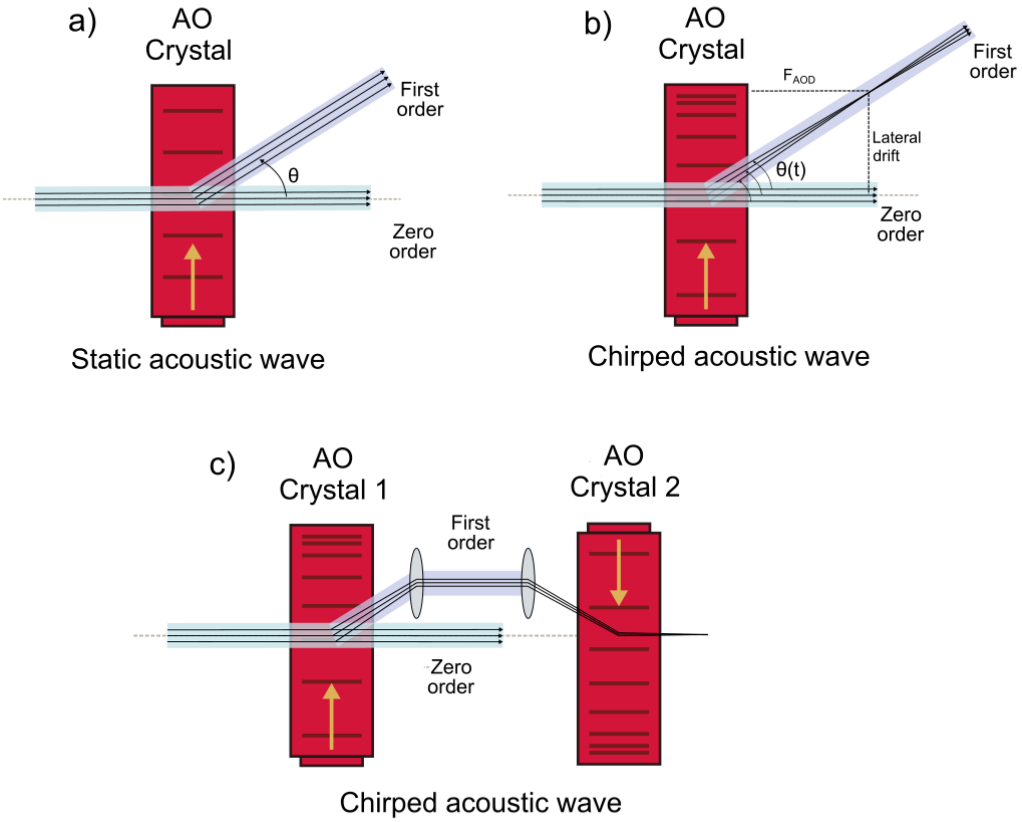

Figure 3.3_1: Operating principle of the acousto-optic deflector. At the base of the AO crystal is placed a piezo-electric compound, driven by a radiofrequency and generating a sound wave that propagates through the material. The periodic change in the refractive index induced by the propagating sound wave is seen as a diffraction grating by the input beam. The deflection felt by the imping beam is proportional to the static frequency **(a)**, or results time-dependent in the case of a linearly changing frequency **(b)**. In this case, different portions will be deflected correspondingly of different amounts, globally determining a beam focussing or defocussing and lateral drift. **(c)** Telescopically relaying two devices and driving the second one with a counterpropagant wave counterposes the lateral drift.

4. Thesis proposal

All-optical approaches represent today the avant-garde for the neuroscientists who aim to manipulate and control the neuronal activation or inhibition of specific neuronal clusters, and to monitor the behavioural outcome through specific calcium imaging methods. Coupling advanced microscopy methods with a photostimulation setup enabling large volumetric access and selective and fast light addressing would enable to optically control larger brain areas.

On the optical imaging side, a cornerstone microscopy technique is the LSFM, enabling fast high-contrast volumetric acquisition of biological mesoscale samples. Thus, the first purpose of this thesis is to investigate the ways to obtain optical improvements of LSFM setups, in order to reach artifact-free imaging[142], faster acquisition[78] and enhanced signal detection[104]. On the other hand, the second part of my PhD project regarded the development of a 3D photostimulation system carrying technological advancements with respect to the state-of-the-art in the field.

Starting from the imaging by LSFM, the main drawback of this technique has been taken into account for first in this project: the striping artifacts (**chapter 6.1**). Samples containing absorbing objects produce shadows behind the obstructions, which appear as stripes in the images acquired orthogonally. The un-even illumination provided by light absorption or scattering effects can be avoided by pivoting the illumination beam before the sample, which means increasing the angular diversity of the excitation beam to recover information behind the obstacle. This multi-directional illumination has represented in many cases a viable alternative to attenuate the problem and improve imaging conditions. In detail, if the beam rotates faster than the image acquisition rate, i.e., the integration time of the detector, it is possible to average out over time the shadow attenuation at different angles and prospectives after the obstacles. Light-sheet pivoting is usually realized using galvanometric mirrors that operate at slow sweeping rates (200 Hz for closed-loop mirrors and 12 kHz for resonant ones). For this reason, they are not optimal for a confocal detection regime where, with advanced sCMOS sensors, the line exposure times in the rolling shutter modality can be lower than 10 μs, corresponding to sweeping rates over 100 kHz. Furthermore, it has been demonstrated that image artifacts are still evident using slow sweeping rates, while they are greatly reduced at higher rates[92]. For this reason, a method to speed up the pivoting dynamic has been proposed in this thesis and implemented in a DSLM: it is based on the use of AOD. Its features have been exploited to illuminate the sample in several modalities, spanning from multiple beams at different angles (static multi-angle illumination) to a single beam rapidly swept (MHz rates).

Another issue for signal detection in LSFM is represented by scattered emitted photons because their trajectories and intensity contribution cannot be distinguished from that of ballistic ones, consequently reducing the image SNR and contrast. For this reason, confocal detection has been introduced in LSFM allowing to reject out-of-focus contributions and scattered light. Thus, the potentialities of the proposed pivoting approach have been demonstrated in combination with confocal detection, obtained by a digital slit setting the camera sensor in rolling shutter acquisition mode.

The second point addressed in this work regards the acquisition speed enhancement in a confocal detection regime in a DSLM (chapter 6.2). Most modern CMOS have two rolling shutters to achieve selective line detection, but usually, only a single beam is used to illuminate the sample, halving the maximum obtainable frame rate. The capability to recover the full image acquisition rate can be achieved via dual confocal DSLM, which means a dual illumination simultaneously addressed in front of the detector. AODs can be used in this regard as fast laser beam deflectors to create multiple beams, generating them from a single impinging one by addressing more than one driving frequency at once to the device. In such a way, they enable independent control and synchronization of two beams with the two rolling slits on the camera, doubling the imaging speed without affecting the confocal detection and the high contrast guaranteed. In particular, to demonstrate this claim, this high-speed confocal LSFM has been used to explore the mouse brain structure with subcellular resolution and to record zebrafish larvae's brain activity, which are typical LSFM applications.

For last, the light polarization state of the excitation light has been studied and perfectioned to obtain a larger detected signal (chapter 6.3). Polarization indeed plays a significant role in LSFM, especially when 2P absorption processes are involved. Therefore, as the first point in this thesis, the effects of different polarization states have been tested to observe how they can affect the detected signal levels while imaging typical biological samples with a spatially unordered dye population. In particular, several fluorescence signals have been recorded, obtained using different polarization states with various fluorophores (fluorescein, EGFP and GCaMP6s) and different samples (liquid solution and fixed or living zebrafish larvae), then compared with what we estimated a priori by a theoretical model.

On the photostimulation side, a method that guarantees high-speed accessibility to large volumes and flexibility in light-targeting - to quasi-simultaneously stimulate multiple sites - is still lacking. Furthermore, even if notable advancements in terms of optical access and illumination selectivity have been achieved by combining two-photon (2P) excitation with laser scanning microscopy, 2P optogenetics has been limited by the long commutation times and refresh rates of traditional scanning methods, such as galvanometric mirrors and SLM.

An aim of this PhD project was the development of a 3D 2P photostimulation scheme that guarantees a faster scanning refresh rate and enables to fulfil the temporal requirements for the concurrent activation of spatially distributed neurons. To reach this goal, AODs have been exploited once again in this thesis as a viable alternative with respect to parallel methods. This technology has been used properly to rapidly sweep the light beam and change its focusing, for optimized light addressing strategies. In detail, a setup with a scanning head composed of four

AODs has been designed and implemented for independent fast axial and lateral focal positioning (**chapter 7.1**).

Despite fundamental advantages, state of the art AOD-based optogenetic applications has been so far limited to 1P neuronal photostimulation in 2D[151,152]. Indeed, the intrinsic dependency of the Acousto-Optic (AO) cell diffraction efficiency on the drive acoustic frequency has so far limited the suitability of these devices for 3D optostimulation experiments. More specifically, the power transmission of these devices drops rapidly when moving the scanning spot away from the original focal plane. This issue is less critical when performing in-vivo calcium imaging, as only measurements of the relative fluorescence expression with respect to baseline ($\Delta F/F$) are necessary. However, it is demanding for 3D photostimulation applications. One possible approach to overcome this lack of uniformity in the axial power distribution is applying a pre-calibrated tuning of the driving signal frequency and intensity for each point addressed and illuminated within the FOV, flattening the peak power value achieved at the inherent objective focal plane down to the level delivered at the most axially dislocated plane[25].

Alternatively, in this thesis (**chapter 7.2**), a novel approach has been proposed to face this major drawback, improving the delivered axial power homogeneity, while still achieving a uniform lateral illumination range. In particular, the excitation power has been raised in all the addressable points within the accessible stimulation volume, differently from what has been done in[25].

The 3D photostimulation performance of this 2P-microscope has been proved through the volumetric activation of an optogenetic actuator in zebrafish larvae (**chapter 7.3**). In this context, electrophysiological recordings (local field potential, LFP) were used as a global activity readout of neuronal clusters displaced in different planes, demonstrating efficient axial scanning by observing uniform responses and activation probabilities in the volume investigated.

5. Methods and procedures

5.1. Sample methods and operations

This chapter is dedicated to the methodologies and the procedures relative to each sample analysed in the experiments reported in this thesis. The preparation, maintenance, transgenesis and processing of zebrafish larvae and ex vivo mouse brain are treated in detail and reported separately. The title of each subchapter also indicates the experiment where they have been used:

I. Fast multidirectional DSLM
II. Dual beam confocal detection
III. Effect of light polarization in LSFM
IV. Fast 2P 3D photostimulation

5.1.1. Mice-tdTomato (I)

Male FosTRAP mice (B6.129 (Cg) - Fos$^{tm1.1(cre/ERT2)Luo}$/J x B6.Cg - Gt (ROSA) 26Sor$^{tm9(CAG\text{-}tdTomato)Hze}$/J, n=3) were used for this work. Adult mice were handled and injected with a saline solution daily for at least 3 days prior to the 4-hydroxytamoxifen (4-TMX) injection, always leaving them in their own homecage. 4-TMX (Sigma H6278) was first dissolved in ethanol to a concentration of 20 mg mL^{-1}. This stock was then melted with corn oil at 37 °C to obtain an injectable oil formulation.

On the last day, 50 mg kg^{-1} of 4-TMX was given intraperitoneally to all mice. All experimental procedures were approved by the Italian Ministry of Health (Authorization n. 512-2018_FC)[153].

5.1.2. Ex-vivo mice processing (I)

One week after the tamoxifen injection, animals were deeply anaesthetized and transcardially perfused with 50 mL of ice-cold 0.01M phosphate-buffered saline (PBS) solution (pH 7.6) followed by 75 mL of freshly prepared paraformaldehyde (PFA) 4% (pH 7.6). The extracted brains were then processed according to the CLARITY/TDE protocol[80]. In detail, specimens were left in PFA at 4 °C over night. The following day, samples were incubated in the hydrogel solutions (containing 10% acrylamide (wt/vol), 2.5% bis-acrylamide (wt/vol) and 0.25% VA044 (wt/vol) in PBS) at 4 °C for 3 days to allow a sufficient diffusion into the tissue. Samples were then degassed, replacing oxygen inside the vials with nitrogen, and the hydrogel was polymerized by incubation in a water bath at 37 °C for 3 hours. Later, embedded brains were then placed in a clearing solution (full of sodium dodecyl sulfate, SDS) at 37 °C. Specimens were gently shaken throughout the whole period. After clearing, samples were incubated for 1 day in PBS with 0.1 Triton-X (pH 7.6) and 1 day in PBS (pH 7.6), removing the excess SDS. Finally, murine brains were immersed in a mixture of 40% 2-2' Thiodiethanol (TDE) in PBS (vol/vol) for imaging, that has a refractive index $n_{refr} = 1.41$.

5.1.3. Zebrafish maintenance (II)

Adult and larval zebrafish (Danio Rerio) were maintained for breeding at 28°C on a 14 h/10 h light/dark cycle according to standard procedure. Embryos and larvae were raised up to 5 dpf (days postfertilization) in fish water [150 mg/L instant ocean, 6.9 mg/L NaH2PO4, 12.5 mg/L Na2 HPO4 (pH 7.2)] in a Petri dish kept at 28°C. We used 5 dpf transgenic Tg(elavl3:H2B-GCaMP6s) zebrafish larvae in the homozygous albino background to avoid the presence of skin pigments. Each sample was transferred into a 2-mL tube containing 1.5% w/v low gelling temperature agarose (A9414, Sigma) dissolved in fish water, kept at 38°C, and then introduced into a glass capillary (O.D. 1.5 mm) with a pipette. After gel polymerization, the head portion of the larva was extruded from the capillary. To minimize movement artifacts, larvae were preincubated 10 min in 2 mM d-tubocurarine (T2379, Sigma) dissolved in fish water. The capillary containing the larva was then mounted in a custom-made holder and immersed in the fish water-filled cuvette. Fish rising and experiments were carried in accordance with European and Italian law on animal experimentation (D.L. 4 March 2014, no. 26), under authorization no. 407/2015-PR from the Italian Ministry of Health.

5.1.4. Cleared mouse maintenance (II)

One C57Bl6 mouse was anaesthetized with isoflurane and perfused transcardially with ice-cold 4% paraformaldehyde. The brain was post-fixed overnight at 4°C and then cleared using the passive CLARITY technique. The fixed mouse brain was incubated in hydrogel solution [4% (wt/vol) acrylamide, 0.05% (wt/vol) bis-acrylamide, 0.25% (wt/vol) VA044] in 0.01 M PBS at 4°C for 3 days. The sample was then degassed and incubated at 37°C for 3 h to allow the hydrogel polymerization. The brain was then extracted from the polymerized gel and incubated in a clearing solution [200 mM sodium borate buffer, 4% (wt/vol) sodium dodecyl sulphate (pH 8.5)] at 37°C for 1 month while gently shaking. The sample was then washed with PBST (0.1% Triton X-100 in 1× PBS) twice for 24 h each at room temperature. The cell nuclei were stained by incubation in PBS at RT for 24 h with Sytox-Green (Thermofisher). The next day, the sample was washed with PBS and imaged. Mouse experiments were carried in accordance with European and Italian law on animal experimentation (D.L. 4 March 2014, no. 26), under authorization no. 790/2016-PR from the Italian Ministry of Health.

5.1.5. Transgenic zebrafish: GCaMP6 and EGFP (III)

Two strains of transgenic zebrafish larvae were used: 3 Tg(elavl3:H2B-GCaMP6s) larvae[154,155] in the homozygous *albino* background and 6 Tg(actin: EGFP) larvae[156]. The former expressed, with nuclear localization, the fluorescent calcium sensor "GCaMP6s" under a pan-neuronal promoter, while the latter expressed enhanced GFP (EGFP) in all tissues owing to a ubiquitous promoter. Zebrafish strains were maintained according to standard procedures[157]. To avoid skin pigment formation, Tg(actin: EGFP) larvae were raised in 0.003% N-phenylthiourea (P7629, Sigma-Aldrich). All larvae were observed at 4 dpf. Fish maintenance and handling were carried out in accordance with European and Italian law on animal experimentation (D.L. 4 March 2014, no. 26), under authorization no. 407/2015-PR from the Italian Ministry of Health.

Five of the larvae were subjected to live imaging. Immediately before the acquisition, each larva was anaesthetized with a solution of tricaine (160 mg/L; A5040, Sigma-Aldrich), included in 1.5% (w/v) low gelling temperature agarose (A9414, Sigma-Aldrich) in fish water (150 mg/L Instant Ocean, 6.9 mg/L NaH_2PO_4, 12.5 mg/L Na_2HPO_4, pH 7.2) and mounted on custom-made glass support immersed in fish water thermostated at 28.5 °C, as described in[118]. The other 4 larvae were fixed (2h in 4% paraformaldehyde in PBS at room temperature) before undergoing the same mounting procedure.

5.1.6. Zebrafish transgenesis: ReaChR-TagRFP and GCaMP6s (IV)

A zebrafish Tg(elavl3:ReaChR-TagRFP) line was generated using a tol2 plasmid with elavl3 promoter which drives the expression of the red-shifted light-gated cation channel ReaChR in all differentiated neurons[123,158]. The plasmid vector was injected along with transposase mRNA into one-cell stage zebrafish embryos. Mosaic transgenic larvae displaying strong TagRFP fluorescence at 48h post-fertilization were selected and raised to adulthood. Offspring from one single selected founder was finally used to establish the new stable transgenic line used for the experiments.

Larvae used in the experiments - Tg(elavl3:ReaChR-TagRFP) and Tg(elavl3:H2B-GCaMP6s), slc45a2$^{b4/b4}$ [154,155], *albino* background - were maintained at 28.5 °C in fish water (150 mg/L Instant Ocean, 6.9 mg/L NaH_2PO_4, 12.5 mg/L Na_2HPO_4; conductivity 300 μS/cm, pH 7.2) under 14/10 h light/dark cycle, according to standard procedures[157]. Larvae of the Tg(elavl3:ReaChR-TagRFP) were raised in 0.003% N-phenylthiourea (P7629 Sigma-Aldrich) to inhibit melanogenesis, avoiding the formation of skin pigments.

Zebrafish larvae were mounted as previously described[118]. Briefly, every 5 dpf larva was transferred into a reaction tube containing 1.5% (w/v) low gelling temperature agarose (A9414, Sigma-Aldrich) in fish water, maintained fluid at 38 °C. The larva was then placed inside a glass capillary (I.D. 0.86 mm; B150-86-10, Sutter Instrument). Upon gel polymerization, it was extruded and laid on a microscope slide, with the dorsal portion facing upwards. A drop of melted agarose was used to block larva orientation. Using a scalpel, the part of the gel was removed, leaving the left or the right half of the head accessible to the electrode, while keeping the animal embedded in agarose. To avoid movement artifacts during measurements, the larva was then paralyzed by 10 min treatment with 2 mM d-tubocurarine (93750, Sigma-Aldrich), a neuro-muscular blocker. After drug wash-out, the mounted larva was placed inside a Petri dish (Ø 90 mm) filled with fish water kept at 28.5 °C throughout the whole experiment.

5.2. Fast beam pivoting in CDSLM

In this work, a pre-existent DSLM setup was slightly modified to introduce an AOD in the optical path. The potentialities of the AOD were exploited to provide different pivoted illumination strategies, spanning from a single beam rapidly pivoted in front of the illumination objective to multiple beams simultaneously addressed at different angles.

The original DSLM configuration is described in[159], from which an excitation arm was modified, and schematically represented in **Fig.5.2_1**. This adaptation introduced an alternative optical path, as indicated in the red dashed rectangle, properly adopted for the beam shaping and pivoting. This pathway was easily addressable through a pair of flip-flop mirrors placed between the laser unit and the galvo head. This was used as a scanning system to digitally sweep the beam and create the light sheet in DSLM.

With this particular conformation, this setup allowed also to easily change the flip-flops configuration leading the beam to pass straight toward the galvo head, without being modelled or pivoted.

In detail, a visible light beam generated by a laser diode (Cobolt AB, Jive 561 nm, 50 mW, s-polarized) was first expanded 5× by a telescope (Thorlabs AC080-020-A F_L = 20 mm and Thorlabs AC254-200-A F_L = 200 mm) and was then guided through a second telescope made by two cylindrical lenses (Thorlabs ACY254-150-B F_L = 150 mm and Thorlabs LJ1878L2-A F_L = 10 mm) to collapse one beam dimension by a factor of 15.

Afterwards, the light went through a half-wave plate and enters into an AOD (AA Opto Electronic, DTSX-400, TeO2, aperture 7.5×7.5 mm^2) that was driven by a RF multi-channel driver (MDSnC, 8 channels, centred at 92 MHz, bandwidth 56 MHz). The pivoted light was then collected and collimated by a Thorlabs AC508-500-A F_L = 500 mm, which formed a 1:1 telescope with the first lens F_L = 500 mm placed after the second flip-flop mirror. The following galvo head digitally generated the light sheet and was positioned in a conjugated plane with the back focal plane of the excitation objective Plan Flour EPI, 10×, 0.3 NA, WD 17.5 mm, Nikon, Japan. An Olympus XLPlan N 10×/0.60 SVMP Objective, paired with a F_L = 200 mm tube lens in turn used to detect the fluorescence emitted by the samples. The signal was then filtered by a bandpass filter (FF01-609/54-25, Semrock) and, finally, collected by a sCMOS camera (Orca Flash4.0 v2.0, Hamamatsu) with a pixel size of 6.5×6.5 μm^2 and an active area of 13.3×13.3 mm^2.

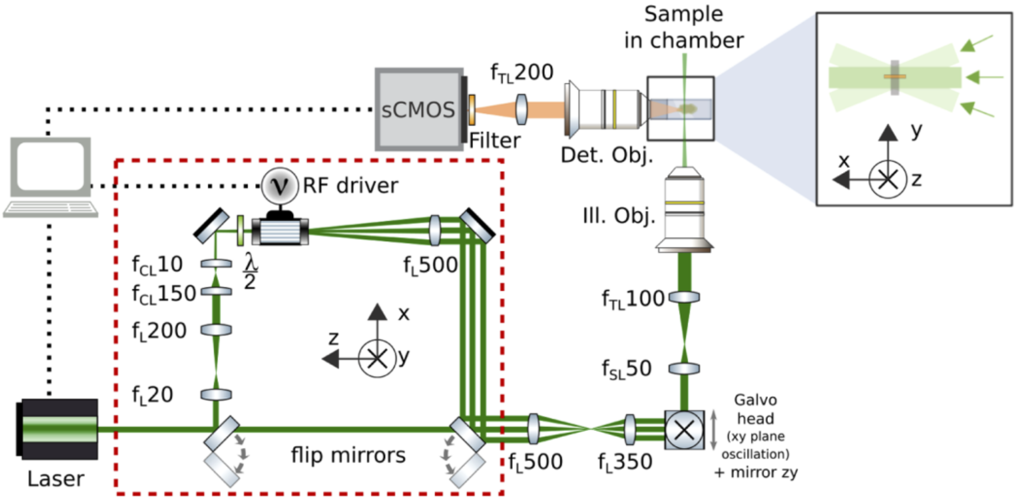

Figure 5.2_1: Multi-directional DSLM setup. Schematic of the excitation line, beam forming and imaging path. The red dashed rectangle contains the alternative light path, selectable via flip-flop mirrors: two cylindrical lenses CL shape the circular Gaussian beam into an elliptical profile that is then pivoted by an AOD. Modified from[142].

In **Fig.5.2_1**, the beam propagation direction, the pivoting direction (and light sheet width) and the detection direction (light sheet thickness) are indicated respectively with $\hat{x}$, $\hat{y}$ and $\hat{z}$.

5.3. Dual beam generation for confocal detection LSM

In this work, an AOD was used to generate two Gaussian beams and sweep them independently but simultaneously in a DLSM. The crystal was inserted in the illumination path providing a dual illumination which covered the FOV in front of the camera.

Two main sensor readout modes were used for the acquisitions. First, in single rolling shutter mode, the slit was continuously swept from the top edge to the bottom one or vice versa. Second, in double rolling shutter mode, the sensor was divided into two halves that were jointly recorded via two rolling shutters moving from the middle out to the top (or bottom) edges or in the same direction. To benefit from the confocal detection modality enabled by the rolling shutter modes on sCMOS cameras, the illuminating beams had to be spatially overlapped and synchronized with the moving virtual slit positions on the sensor (**Fig.5.3_1a**).

Fig.5.3_1b displays the schematic of the DSLM implemented for single- and dual-confocal detection. The optical architecture was based on a DSLM where the usually exploited galvo mirror was replaced by an AOD. A visible light beam from a diode laser (488 nm, Coherent Sapphire 300) was expanded and collimated by a pair of achromatic lenses (Thorlabs AC254-30-A and AC254-150-A). Then, the beam was guided into the AOD (AA Opto Electronic DTSX-400, TeO2, aperture 7.5×7.5 mm^2) that was driven by a radio frequency (RF) system (four-channel signal generator Analog Devices AD9959PCBZ followed by a Minicircuits power combiner ZMSC-2-1W+ and an amplifier ZHL-1-2W-S+). A scanning lens (Thorlabs AC508-200-A, F_L 200 mm), placed after the AOD, converted the angular deflection into a lateral displacement of the incident light. The beam was then directed by the excitation tube lens (Thorlabs AC508-100-A, F_L100 mm) to the pupil of an illumination objective lens (Nikon N10X-PF 10X, 0.3 NA, 16 mm WD).

The sample, embedded in a cylinder of 1% agarose gel, was immersed in a water-filled cuvette sized 10×12 mm^2. The fluorescence emitted from the sample was collected with an imaging objective (Nikon N10X-PF 10X, 0.3 NA, 16 mm WD), and a tube lens of focal length of 200 mm (Thorlabs TTL200-A) created an image on an sCMOS camera (Hamamatsu Orca-Flash4.0 V3, 2048 × 2048 pixels of 6.5×6.5 μm^2 size).

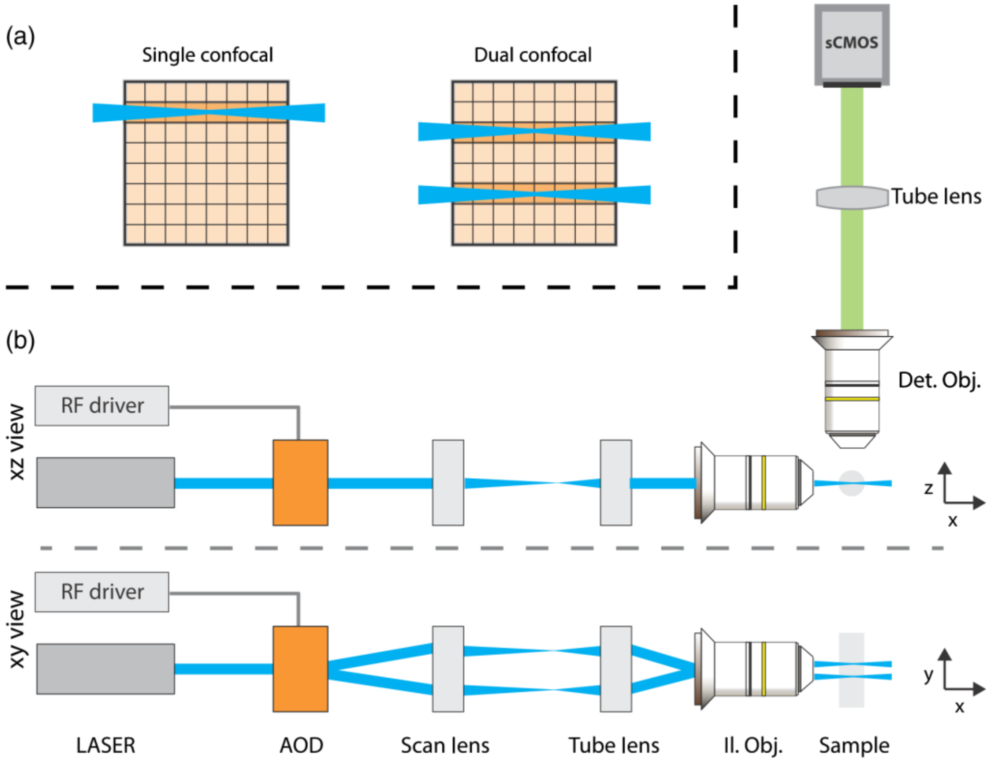

Figure 5.3_1: Schematic of dual beam CLSFM. **(a)** sCMOS camera operating in single - or dual- rolling shutter mode with the illuminating beam - or beams - matching the position and synchronized with the scan rate of the virtual slit - or slits -. **(b)** The excitation and imaging paths from the side and top views. Modified from[78].

The experimental lateral and axial resolutions were 1.5 and 9.0 μm, respectively, while the light-sheet FWHM waist was 10 μm in order to be within one Rayleigh range over the FOV of 1.33×1.33 mm^2. The *xyz* coordinate system was chosen as follows: the light sheets were created in the *xy* plane with the *x*-axis along the beam propagation direction, and the *z*-direction was along the imaging optical axis.

A trigger emitted by a National Instruments PXIe-6738 card started the single - or dual - confocal sample illumination and image acquisition processes, by activating one or two RF ramps on the signal generator that governed the AOD deflection of the laser beams and by synchronously moving the virtual slits across the camera sensor, as shown in the timing diagrams in Fig.5.3_2.

In the dual diverging or converging rolling shutter modes, if the sample presents a significant background level, cross-talk between the two light sheets could be observable when they overlapped in the centre of the sensor. To preventively minimize this effect, which did not affect the parallel modes, the timing and the starting and ending frequencies of the RF ramps were tailored to avoid physically overlapping the two light sheets at any time on the sensor.

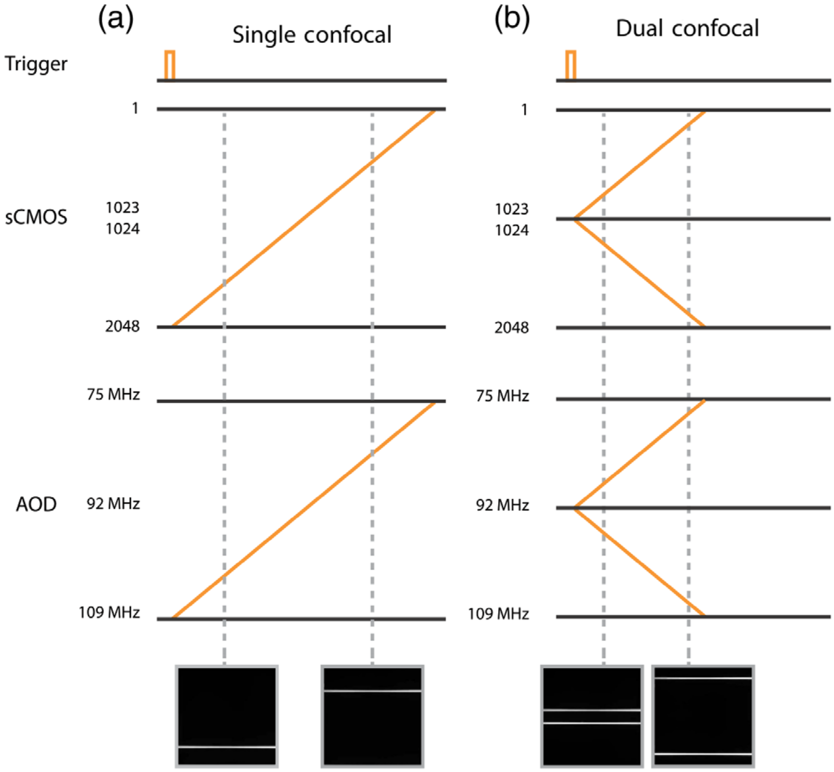

Figure 5.3_2: Timing diagrams for single - and dual - beam CLFM. A common trigger starts the camera acquisition and tailored RF ramps on the signal generator that drives one **(a)** or two **(b)** simultaneous AOD illumination sweeps. The image insets are frames from video acquisitions (MPEG, 0.1 MB [URL: https://doi.org/10.1117/1.JBO.24.10.106504.1]), at the times marked by the dotted lines, of a uniform fluorescent 1% agarose gel in water, imaged with the corresponding rolling shutter readout mode. Modified from[78]

.

5.4. Effects of light polarization 2P-LSFM: imaging design

The optical imaging of the samples was performed with a custom-made 2P LS microscope (**Fig.5.4_1**). The source was a pulsed Ti:Sa laser (Chameleon Ultra II, Coherent) which generated light at 930 nm, initially pre-compensated (PreComp, Coherent) for the group delay dispersion and power-attenuated by means of a half-wave plate and a Glan–Thompson polarizer.

The beam then passed through an Electro-Optical Modulator used to rotate its linear polarization plane by 90°. Moreover, a combination of a half-wave plate and a quarter-wave plate was used to align the light polarization plane with the reference system. The beam was then scanned by a fast resonant galvanometric mirror (CRS-8 kHz, Cambridge Technology), used to generate the digitally-scanned light-sheet along the larval rostro-caudal direction, while a closed-loop galvanometric mirror (6215H, Cambridge Technology) was used to scan the light sheet along the larval dorso-ventral direction. The beam was finally relayed to an excitation dry objective (XLFLUOR4X/340/0,28, Olympus), placed at the lateral side of the larva, by a scan-lens (F_L 50 mm), a tube-lens (F_L 75 mm) and a pair of relay lenses (F_L 250 mm and F_L 200 mm) that underfill the objective pupil. When desired, the light polarization state was converted from linear to circular by placing a removable quarter-wave plate on the optical path between the tube lens and the first relay lens.

The emitted green fluorescent light, coming either from GCaMP6s or EGFP, was collected by a water-immersion objective (XLUMPLFLN20XW, Olympus) placed dorsally above the larva. The objective was scanned along the axial dimension by an objective scanner (PIFOC P-725.4CD, Physik Instrument) synchronously with the closed-loop galvanometric mirror movements. The optical image formed by the detection-objective tube lens (F_L 300 mm) was then demagnified by exploiting a second pair of tube lenses (F_L 200 mm) and objective (UPLFLN10X2, Olympus), bringing the final magnification to 3×. Finally, the green fluorescence was spectrally filtered (FF01-510/84-25 nm BrightLine® single-band bandpass filter, Semrock) and relayed to a sCMOS camera (ORCA-Flash4.0 V3, Hamamatsu).

Imaging was performed with a pixel size of about 2×2 μm^2, and a FOV of about 1×1 mm^2. The acquisitions in fluorescein solution were performed on a single transversal plane with an exposure time of 100 ms. The larvae instead were imaged with volumetric acquisitions composed of 31 planes spaced by 5 μm and with an exposure time of 26 ms for each plane and a volumetric acquisition frequency of 1 Hz. Each acquisition lasted 1 minute and then the 60 acquired volumetric stacks were averaged to obtain one final z-stack.

The laser power used for the acquisitions, measured at the excitation objective pupil, was 100 mW for the Tg(actin: EGFP) larvae both in living and fixed preparations, 200 mW for the live imaging of Tg(elavl3:H2B-GCaMP6s) larvae, 180 mW for the fixed Tg(elavl3:H2B-GCaMP6s) larvae and 162 mW for the fluorescein solution acquisition. The excitation power was kept constant and far from the fluorescence saturation regime when imaging.

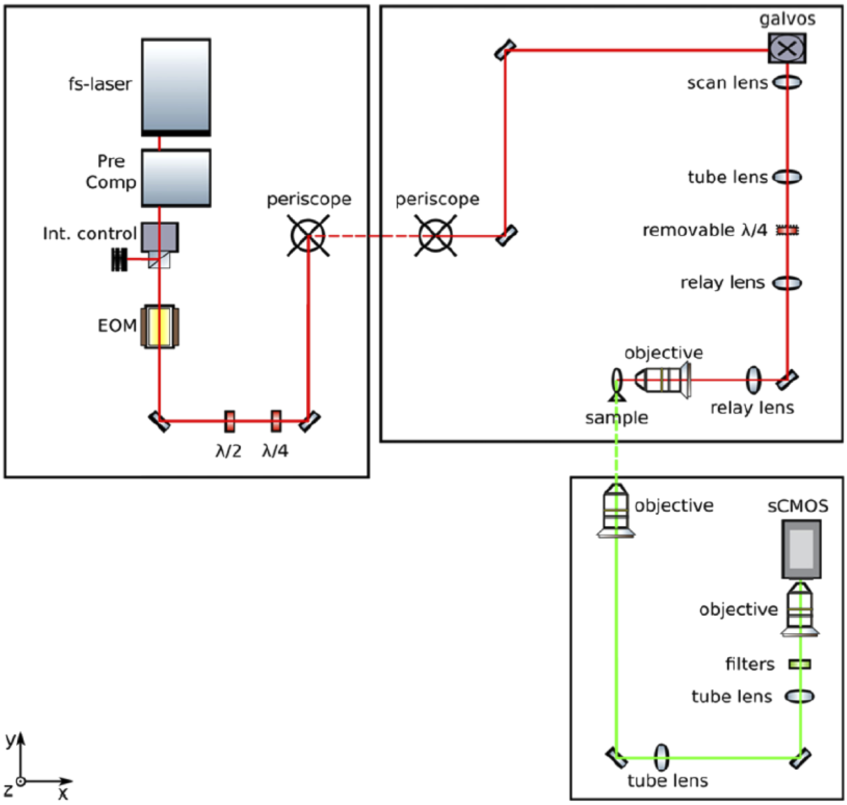

Figure 5.4_1: 2P LSM schematic for polarization studies. Fs-laser: femtosecond laser. Pre Comp: pulse compressor. Int. control: intensity control assembly, composed of a half-wave plate and a Glan–Thompson prism. EOM: Electro-Optical Modulator. λ/2: half-wave plate. λ/4: quarter-wave plate. Galvos: galvanometric mirror assembly, composed of a resonant mirror and a closed-loop mirror. Red line: excitation light. Green line: fluorescence light. The dashed lines indicate vertical paths. Modified from[104].

5.5. 2P 3D photostimulation with AODs

To achieve a laser scanning system that guarantees deep optical access, large areas of light addressability and fast dynamics for illumination pattern configuration, a hybrid solution composed of four AODs and a GM head have been implemented. The proper use of four AODs enabled precise light targeting of any point in the volume and a quick modulation of the stimulation pattern. Furthermore, even if with slower dynamics with respect to the AO scanning, a larger optical FOV was obtained by coupling the former device with a GM scanning head. The integration of the two scanning heads, achieved with a dedicated optical design, allowed the visualization of each macro-ROI selected in the GM's FOV and to record and fast manipulate neurons over areas defined by the AOD scanning range with high temporal resolution.

The system was developed as a stand-alone add-on module for coupling with standard microscopes. To validate the performance of the scanning head, it has been coupled with a Leica DM LFSA Microscope (Leica Microsystems GmbH, Wetzlar, Germany) for 2P imaging and photostimulation tests. Analogously to what debated for the lateral scanning, a slow but wide axial scanning was provided by the Leica objective stepper motor, whereas fast-axial displacement is achieved using the AODs. The whole setup is schematically represented in **Fig.5.5_1a**.

The light source consisted of a 1064-nm pulsed laser (FP-1060-5-fs Fianium FemtoPower, NKT Photonics, Birkerød, Denmark), characterized by a pulse duration shorter than 200 fs, a repetition rate of 80 MHz, and a maximum power of 5 W. The laser beam was first directed through a half-wave waveplate (10RP02-34 Newport Corp., Irvine, CA, USA) to shift its polarization, and then it was conveyed through a Glan-Taylor polarizer (GTH5-B Thorlabs Inc., Newton, NJ, USA). The waveplate was positioned in a software-controlled rotator (MDL NSR1 Newport) allowing adjustment of the outgoing beam power, without altering its polarization.

The beam was then expanded by a factor 1.66× using a telescope (AC254-075-B-ML Thorlabs F_L mm and AC254-125-B-ML Thorlabs F_L 125 mm), and its polarization orientation was optimized by a second $\lambda/2$ waveplate (10RP02-34 NewPort), before reaching the first pair of AODs (DTSXY-400 AA Opto Electronic, Orsay, France). Then, to optically couple two AOD stages, the outgoing beam was first directed into two 1:1 relay systems, respectively (AC254-050-B-MLThorlabs F_L 50 mm) and (PAC19AR.16 Newport F_L 75 mm). In this way, independently of the RF applied to the first couple (and therefore regardless of the outgoing beam direction), light reached a pivot at the centre of the second AOD stage.

From the second AOD stage, the beam was expanded 2× by a 1:2 relay (PAC17AR.16 Newport F_L 50 mm and PAC12AR.16 Newport F_L 100 mm) and conveyed to the centre of the GMs (GVS112 Thorlabs), preceding the scan lens (AC254-050-B Thorlabs). This was optically coupled with the tube lens of the Leica DM LSFA, producing a further 4x magnification of the beam size. A dichroic short pass mirror (NENIR20A Thorlabs), positioned inside the Leica DM LSFA before the objective, was used to reflect the excitation light towards the objective (20X XLUMPLFLN Olympus Corp., Tokyo, Japan) and to transmit the fluorescence emitted by the sample onto the PMT detector (H7422P-40 Hamamatsu Photonics, Hamamatsu, Japan), through a NIR absorptive filter.

The combined use of four AODs is necessary for fast axial scanning. The designed system took advantage of them, arranged as two pairs of orthogonally oriented identical devices, each having the first and second AOD assigned to the x and y lateral axes, respectively. The two coupled stages are driven by counter-propagating waves, characterized by a linearly changing frequency $f(t) = f_{min} + \alpha t$, where α is the frequency ramp slope - or chirp parameter. This arrangement, which globally works as a variable AO lens (AOL), has a focal length F_{AOL} dependent on the chirp (**Eq.3.2_7**), affecting the light beam divergence and the total magnification of the optical path. It determines an axial displacement *ΔZ* that propagates up to the image plane under the objective (**Fig. 5.5_1b**) equal to:

$$\Delta Z = \frac{F_1^2 \cdot M^2}{F_{AOL}} = k \cdot \alpha \qquad \text{with} \qquad k = \frac{2\lambda \cdot F_1^2 \cdot M^2}{\nu^2} \qquad (5.5\_1)$$

Where *v* is the propagation speed of the acoustic wave in the crystal, *λ* is the wavelength of the laser, F_1 is the focal length of the first lens after the second stage and *M* is the optical magnification factor regarding the subsequent optics.

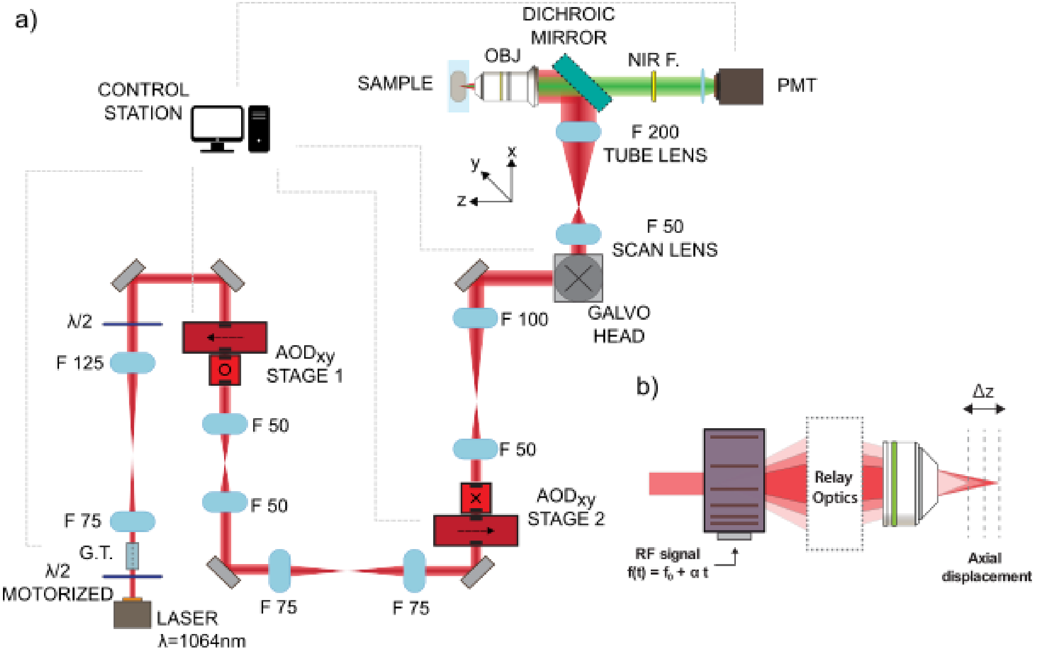

Figure 5.5_1: Schematic the AOD-based scanning head. **(a)** Optical setup with hybrid galvo-AOD scanning head implemented for 2P excitation; F: Focal length; NIR F.: Near-Infrared Filter; G.T.: Glan-Taylor polarizer. **(b)** Optical diagram of the AOL focusing performance and the induced axial displacement with respect to the inherent objective focal plane. Modified from Ricci et al. 2021.

It is worth noting that the AOD crystals and the optical configuration proposed in this work slightly differed from the most common implementations[25,27]. Here, each stage exploited two tellurium dioxide (TeO_2) crystals, through which the acoustic wave anisotropically interacted with the light beam, offering high transmission efficiency and a large acoustic and optical bandwidth. In particular, when the directions of the input optical wave vector and the driving acoustic wave were maintained constant, these devices provided a large scan angle, with a resolution up to 400 dots over an optical aperture of 7.5 mm. In detail, these AODs had a collinear design for the central frequency (f_c) with respect to the whole frequency bandwidth available. It meant that when the input beam entered right in the middle and orthogonally to the first aperture, the deflected beam at (f_c, f_c) resulted collinear to the input beam; thanks to their particular wedge design, the 0th order beam was therefore rejected with a specific angle. Each AOD stage was mounted on a compact 5-axis stage (PY005, Thorlabs Inc., Newton, NJ, US) to increase the degrees of freedom of the apparatus, allowing their horizontal and vertical translation, and 2-axis rotation. This led to optimization in terms of transmission through the coupling with the higher efficient diffracted order.

However, when the acousto-optic coupling was not stationary and the angle of incidence of the input wave vector became less tangential to the acoustic one, a drop in the optical transmission power occurred. It was then important a trade-off between transmission efficiency and acceptance angle in order to maximize the axial range while providing a uniform intensity distribution. For this goal, in the configuration presented, the first stage frequencies chirped around $f_{1c} = f_c$, while the second stage pivoted the beam covering the full range to increase the FOV size (see **chapter 7.1** for the optical characterization of the system).

A second precaution regarded the optimization of the chromatic dispersion, caused by the interaction between the femtosecond-pulsed laser with the AO crystal. The pulsed signal generated by the broadband laser is indeed composed of several frequencies that propagate at once; however, the crystal response in terms of beam deflection strictly depends on the input wavelength, and therefore on its frequency, as:

$$\Delta\theta = \frac{\Delta\lambda \cdot f}{2v} \qquad (5.5\_2)$$

where λ is the laser wavelength, f is the RF driving the AOD and *v* represents the sound wave propagation velocity within its internal crystal.

The light beam which left the first AOD stage resulted for this reason slightly deformed, elongated and oblong. The spatial dispersion undergone by the diffracted beam was partially compensated by placing the second pair of AODs symmetrically opposite to the first one. In such a way the dispersion effect was counterbalanced thanks to an inverted deflection of the broadband laser, which increased the symmetry of the beam profile. The reason for the additional relay in the optical path after the first stage was to compensate for the first geometrical inversion due to the telescopic relay (the output image from an optical relay is indeed the mirror image of the input one). Furthermore, the half-wave plate before the first AOD stage was used to provide the optimum input light polarization.

5.5.1. Digital and electronic design: operation rates and signalling

A graphical user interface (GUI) was developed in LabVIEW (National Instrument Corp., Austin, TX, USA) to operate the system. The software employed two National Instrument boards (PCI-6251 and PXIe-6738) to record the fluorescence signals collected by the PMT, and to interface with an Arduino Due microcontroller used to program a four-channel direct digital synthesizer radio-frequency generator (DDS, AD9959 PCBZ Analog Devices Inc., Norwood, MA, USA) which drove the AODs. By integrating the control drivers of the waveplate rotator and the GMs, the software also enabled the remote adjustment of laser power transmission, FOV size and resolution. Moreover, the LabVIEW GUI allowed the efficient and user-friendly design of suitable optogenetic stimulation patterns without directly exposing the configuration parameters of the AOD scanning unit. This software stack was optimized to achieve the minimum encoding error and ensure the robust and precise execution of the AOD driving modalities, thus ensuring accurate positioning of the AOL focus.

The Arduino board communicated with the computer via USB through a Python-to-LabView software layer, while it concurrently directly programs the DDS registers via a single-bit serial port interface (SPI). In particular, the desired trajectories were interpreted by a dedicated Python node, which transmitted to the Arduino microcontroller board the corresponding sequence of encoded data words, tuning the discrete-time and frequency steps of the generated chirps. Furthermore, the developed software made efficient use of the limited 96 kB SRAM available on the Arduino Due board to provide the maximum number of addressable spatial coordinates during a single scanning cycle, i.e., the highest number of scanned targets and their local scanning resolution. The maximum number of target spots that could be addressed by means of a quasi-simultaneous multi-site stimulation pattern is defined by:

$$N_{spot} = \frac{N_{word}}{Max(N_x, N_y) \cdot N_z} \qquad (5.5.1\_1)$$

where (N_x, N_y, N_z) represent the shape of the 3D raster scan localized on each target of interest, and N_{word} is the maximum size of the data word buffers allowed by the available SRAM ($N_{word} \approx 2000$ for the Arduino Due).

Finally, the Arduino software was engineered to configure at the maximum possible rate the DDS channels in each implemented beam-scanning modality in order to achieve the minimum switching time of the AOL focus position. In detail, fast 2D raster scans within the inherent focal plane of the objective could be achieved by taking advantage of the single-tone (i.e., unchirped) operation mode of the DDS and by dynamically updating only the two four-byte data words responsible for tuning the stationary frequencies in the second pair of AODs. In this scanning configuration, the longest beam-positioning time corresponding to the simultaneous change of the driving RFs applied to the x- and y-axes were 7 µs. On the other hand, chirped scan modalities supporting 3D targeting patterns were implemented using the linear sweep operation mode of the DDS. In this configuration, however, more tuning words had to be communicated via the SPI port between each I/O update pulse, increasing the programming time. Specifically, 3D random-access positioning of the laser beam was achieved by sequentially setting the lower and upper frequencies of the chirps generated on each RF channel (i.e., two four-byte words per channel). Together to them, the data words needed to adapt the discrete-time and frequency step sizes of the linear sweeps (two bytes plus two four-byte words transferred in a single communication, as all channels share the same chirp value) were sent. This resulted in an increase of the minimum beam-positioning time to 20 µs for 3D random-access scans.

5.5.2. Electrophysiology recording

The photostimulation performance was tested through the volumetric activation of an optogenetic actuator in zebrafish larvae while the neuronal cluster activity was read by means of LFPs. These were recorded using a borosilicate glass microelectrode (8–10 MΩ), back-filled with a filtered solution of 2 M NaCl and 0.1 mM Sulforhodamine 101 (S7635, Sigma-Aldrich) to allow the electrode tip imaging. The microelectrode was placed under visual guidance into the larval hindbrain at 150-200 µm depth. Voltage signals were recorded using an Axopatch 200B amplifier (Molecular Devices, San Jose, CA, USA), low-pass filtered at 2 kHz, and digitized at 10 kHz using a USB-621 interface (National Instruments)

5.6. Data Analysis

In this chapter the different data analysis techniques and data evaluation methods used in this thesis are reported and described in detail. The different strategies are described separately, indicating the work where they have been exploited:

I. Fast multidirectional DSLM
II. Dual beam confocal detection
III. Effect of light polarization in LSFM
IV. Fast 2P 3D photostimulation

5.6.1. General linear mixed model (III)

General linear mixed models[160] were used to analyse the results for larvae acquisition. In detail, the fluorescent signal was used as a dependent variable, the polarization state as a fixed effect and the fish as a random effect. A linear regression model implemented in R language was used instead to analyse the results for the living GCaMP6s larva. In this case, the fluorescent signal was used as a dependent variable and the polarization state and the ROI as independent variables. In both cases, linear contrast was used to compare the polarization groups and the Sidak method was exploited for the multiplicity correction. Fluorescein solution data were compared by computing 95% Confidence Intervals (C.I.) using the Student's t-distribution.

5.6.2. LFP data analysis (IV)

The whole dataset was analysed with Origin Pro (Version *2019*, OriginLab Corporation, Northampton, MA, USA). LFP signals were detrended using a 0.1 Hz high-pass filter and segmented in a 1 s peristimulus window. For each stimulus, the

LFP response peak amplitude was evaluated. For each larva, we calculated the mean value of the peak amplitudes collected in the unchirped configuration (α=0 MHz/µs), and the datasets were separately normalized with respect to this value. Mean and relative standard errors were calculated for each chirp value subset.

For the volume scanning dataset, two subsets were defined, i.e., single-trigger and multi-trigger configurations, which were normalized with respect to single-trigger subsets.

Regarding probability analysis, the background baseline of the traces was first processed, evaluating its mean and standard deviation for each examined trigger modality and chirp value. Once calculated LFP peak amplitudes and normalized with respect to the unchirped subset as previously described, the positive events were deemed as the evoked LFP with amplitudes passing a threshold equal to three times the baseline standard deviation. Finally, the activation probability was defined as the ratio between positive evoked events to the totality of the cases.

5.6.3 Statistical analysis (IV)

Statistical analysis was performed exploiting linear mixed-effects models[160] implemented with the statistical programming language R (R Core Team. R: A Language and Environment for Statistical Computing. R Foundation for Statistical Computing, 2015.). In all the models the animals were defined as the random factor. Statistical significance was assessed by computing the p-values and confronting them to a threshold of 0.05. In particular, to confront the response amplitudes in different conditions, a general linear mixed model was employed using the “lmerTest” package. In the comparison between the volume-averaged responses with respect to the trigger modalities, the latter was defined as a fixed factor and the observed amplitude as a response variable. In the comparison between the single-plane responses, the chirp value and its interaction with the trigger modality was defined as fixed factors and the normalized amplitude as a response variable. In this case, posthoc analysis was performed with the package “emmeans” by computing linear contrasts for all pairwise comparisons among estimated marginal means[161]. Multiplicity adjustment was carried out with Tukey’s method.

For the analysis of the probability of response occurrence to the optogenetic stimulation, a logistic regression (generalized linear mixed model) was employed using the “lme4” package.

The occurrence of an electrophysiological response was defined as a dichotomous response variable, while fixed effects were: the modulus of the chirp value (numeric variable), its interaction with the trigger mode, and its interaction with a dichotomous variable indicating the sign of the chirp value. The effects were quantified in logits (logistic units), i.e., the natural logarithm of the odds of observing the event[162].

6. Results for Enhanced Light-Sheet Microscopy

6.1. Multi-directional DSLM: standard-, pivoted- and multi-beam

In this thesis, it has been proposed a solution to avoid striping artifacts in DSLM acquisitions, based on the use of an AOD. A pivoted elliptical-Gaussian beam was used for imaging several mouse brain areas acquiring signals emitted by specific fluorophores.

In the proposed hybrid DSLM each scanning line was projected onto the sample, swept by a closed-loop galvo mirror and pivoted around the detection plane by the AOD (relative methods in chapter 5.2). The experiments were carried out in the confocal detection regime, obtained by defining a digital slit through a row of pixels simultaneously activated on the camera sensor.

The beam pivoting and the finite size of the digital slit used in confocal detection are inherently in conflict because a large part of the swivelling beam could rotate out of the confines. Here, a method to overcome this issue was proposed. It preserved the contrast enhancement linked to confocal detection while maintaining the axial illumination uniformity and simultaneously attenuated striping artifacts. In detail, two cylindrical lenses were used to design an optimized optical beam-shaping system. Those lenses generated an expanded elliptical-Gaussian beam that perfectly covered the whole aperture at each inclination during the pivoting. To fulfil this requirement, the second optical pathway was properly engineered in accordance with the following geometrical model.

The finite dimensions of the digital slit in the sample space were determined by the horizontal FOV and by the virtual slit width on the camera. The last was determined automatically when the rolling shutter speed and the line exposure time were chosen by the user. The dimension of the slit on the camera differs from the one on the sample space by a magnification factor of 10×.

Fig.6.1_1a shows a schematic of the beam pivoting geometry in confocal detection.

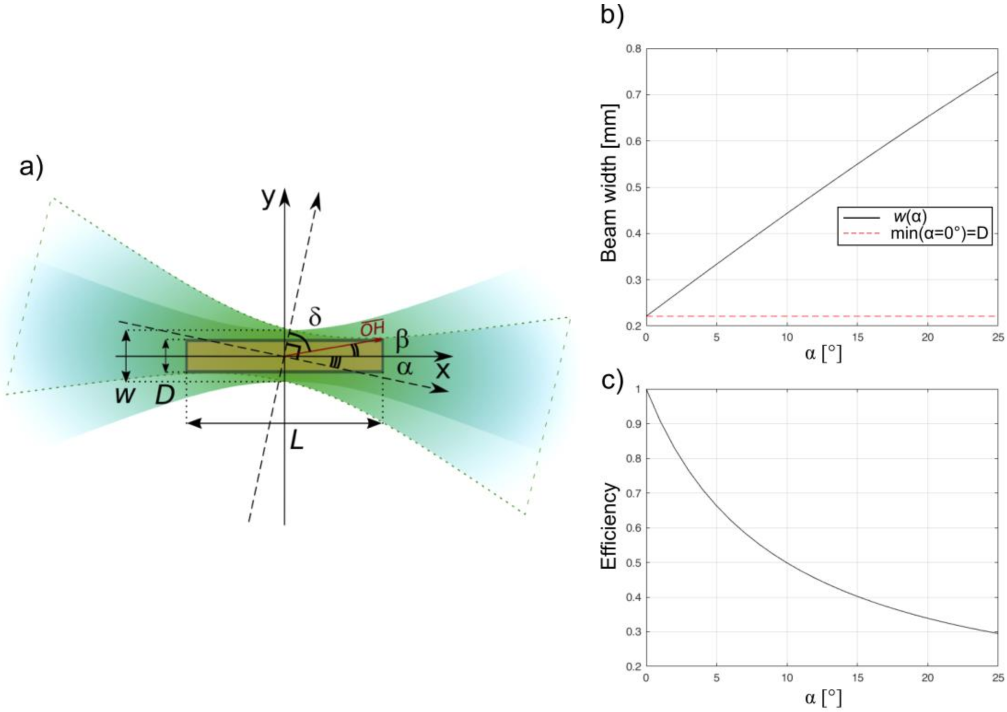

Figure 6.1_1: Geometrical model of the beam pivoting. **(a)** beam arrangement at the sample: *w* beam width; *D* virtual slit width; *L* length of the digital slit on the camera sensor (sepia rectangle); *α* pivoting angle which defines also the complementary angles $\beta + \delta = {}^{\pi}/_{2} - \alpha$. **(b)** and **(c)** show the simulated dependence, respectively, of the beam width *w* and of the detection efficiency *Eff* from the pivoting angle *α*, up to the maximum angle admitted by the excitation objective. The red dotted line indicates the minimum waist required, i.e., *D.* Modified from[142].

Here, *w* was the width of the beam tilted through the sample, *D* was the virtual slit width, *L* was the length of the digital slit (corresponding to the camera FOV) and *α* was the pivoting angle, which in turn defined also the complementary angles:

$$\beta + \delta = {}^{\pi}/_{2} - \alpha \qquad (6.1\_1)$$

The semi-diagonal of the slit, indicated with $\overline{\mathrm{OH}}$, could be easily calculated as:

$$\overline{OH} = \frac{1}{2}\sqrt{L^2 + D^2} \qquad (6.1\_2)$$

While the beam half width was:

$$\frac{w}{2} = \overline{OH}\,cos(\delta) = \overline{OH}\,cos(\frac{\pi}{2} - \beta - \alpha) = \overline{OH}\,sin(\beta + \alpha) \qquad (6.1\_3)$$

That indicates a strict dependence between the maximum pivoting angle α and the beam width w. The angle β can be found as:

$$\beta = arcsin(\frac{D}{2\,\overline{OH}}) \qquad (6.1\_4)$$

The detection efficiency was accounted for by considering the difference between the effective detection area, indicated with the small sepia rectangle in Fig.6.1_1a, and the area illuminated by the scanning beam through the sample, denoted by the green rays. The detection efficiency was then defined by the ratio between the two corresponding dimensions:

$$E = \frac{D}{w} \qquad (6.1\_5)$$

Fig.6.1_1b and 1c show the dependency of the beam width and of the detection efficiency on the pivoting angle *α.*

The digital slit dimension was D = 221 μm in camera space and the length of the digital slit was L = 1.3 mm, from which $\overline{\mathrm{OH}}$ = 0.66 mm. The total angular range determined by the AOD was $\Delta\theta = 2\alpha = 5°$. Using Eqs.6.1_3 and 6.1_4 the beam half-width required to fulfil the maximum demanded illumination was $\frac{w_y}{2} \approx 140$ μm, which led to an expected detection efficiency of *E = 79%*. For this reason, the optical path containing the AOD and the cylindrical lenses was developed according to these considerations.

Finally, those parameters were estimated also empirically. The beam-shaping relay produced an elliptical Gaussian beam profile with anisotropic dimensions along the detection direction $\hat{z}$ and the vertical one $\hat{y}$ (orthogonal to the propagation direction $\hat{x}$). As a consequence, the numerical apertures are NA_z = 0.022 and NA_y = 0.0015 respectively. The narrower beam waist along $\hat{z}$ was then $\frac{w_z}{2} \approx 8$ µm, which led to a Rayleigh length of the virtual light sheet of 530 µm along the illumination propagation direction, therefore guaranteeing an almost uniform illumination over the FOV. The waist along the pivoting direction was $\frac{w_y}{2} \approx 122$ µm, almost reaching the desired optimum value with a small beam divergence. The high degree of angular diversity required for an efficient shadowing suppression was brought by beam pivoting, which results in an effective numerical aperture of $NA_y^{EFF} = NA_y + n_{refr} \cdot sin(\alpha) = 0.063$. It was expected that this pivoting did not affect the beam waist but only the effective numerical aperture NA_{eff} within the sample, increasing the angular diversity.

Thus, to evaluate the light-sheet pivoting effect on striping artifacts, a setup with two alternative optical paths have been implemented. In the first option, the beam is neither optically elliptically formed nor pivoted, providing the classic illumination for the sample for a DSLM, that is a pencil-like Gaussian beam (this configuration is labelled NO AOD). On the other hand, following the indications derived from the former geometrical conclusions, two cylindrical lenses were inserted in the second path to shape the beam as mini light sheets, pivoting them by means of an AOD before the galvo head.

In practice, the FOV containing the sample was illuminated line by line by the galvo head, while the AOD rotated the excitation beam around its propagation axis at a much faster rate. In this regard, considering half scanning range $\alpha = 2.5° = 0.0436\, rad$, the focal distance behind the AOD of $f = 500mm$, the covered aperture $d = 2f \cdot tan(\alpha)$ and the sound wave propagation velocity of $V_{acoustic} =$

$650\, m/s$, it is possible to calculate finally the scanning time as $T_{scanning} = \frac{d}{V_{acoustic}} = 1.1\ \mu s$.

Then, the deflection induced by the AOD was characterized as a function of the radiofrequency (RF) used to drive the piezotranducer. In particular, the angular deflection felt by the laser beam was measured projecting the light inside the sample chamber filled by a 40% 2-2' Thiodiethanol solution in water. As the input RF frequency signal changed the corresponding tilt angle was measured using the angle tool of the open-source software ImageJ, averaging over three images for each configuration. A frequency of 70 MHz was chosen as the central reference, for which the beam entered into the sample chamber perfectly parallel to the optical axis. Then a frequency sweep spanning [-5; +5] MHz was defined around this value to cover a large enough pivoting angle to envelop the digital slit used in confocal detection. A linear model fitted to the data, with a R-square parameter of 0.9989, finding an angular coefficient $m = 1.25\ \pm\ 0.03\, {}^{\circ}MHz^{-1}$ between the deviation angle and the frequency shift.

After this calibration, the results obtained illuminating the sample without pivoting the beam were compared with several illumination modalities allowed by the layout with the AOD. The first of these was the multi-beam arrangement, where a user-defined number of the mini light sheet was redirected by the AOD at determined angulations, propagating simultaneously (in sequence one, three and five static beams, respectively denoted as 1LS, 3LS, 5LS). The second modality was dynamic, where a single mini light-sheet was pivoted over the entire angular range (labelled as scanning beam SB).

Several mouse brain areas were then imaged with the aforementioned approaches, observing real-time shadow suppression once pivoted the beam. A comparison between such scanning beam illumination and a standard static one was carried out also quantitatively, in terms of shadowing reduction and PSF response.

First of all, to quantify the optical performance of the DSLM, the PSF was measured for both the illumination path configurations, i.e., the one with and the one without the AOD. The specimen contained fluorescent beads included in 4% agarose gel. In detail, TetraSpeck microspheres (Invitrogen T7279, with radius r = 50 nm) were used at a final concentration of 0.0025%(vol/vol). The intensity profiles along the radial and axial directions of n=6 sub-micrometric fluorescent beads were computed using the open-source software ImageJ. Each was fitted with a Gaussian model to calculate the full width at half maximum (FWHM). The measurements and the analysis were repeated for three different configurations, NO AOD, 3LS and SB. **Fig.6.1_2** shows the raw data points and the Gaussian model computed with the mean FWHM, obtained respectively along the radial **(a), (c), (e)** and axial **(b), (d), (f)** directions, and from top to bottom respectively for the three mentioned illumination configurations. Panels **(g)** and **(h)** show the mean and the standard deviation of the FWHM extracted from these measurements.

As expected, the presence of the AOD, introduced to pivot the beam did not affect significantly the lateral and axial resolution. Panel **(i)** shows a representative frame containing the fluorescence signal produced by a fluorescent bead.

To test the advantages of beam pivoting over the static beam configuration in DSLM in terms of striping remotion, three cleared mouse brains expressing the fluorescent protein tdTomato were imaged. The right panels in **Fig.6.1_3** show the same frame taken in different modalities, while on the left are reported the normalized grey-scale intensity profiles taken along the vertical dotted red arrow.

As expected, there was no highlighted difference between the static configuration with NO AOD and the one obtained with a single mini-light sheet (1LS), directed centrally by the AOD through the second optical path. Those two illumination strategies were then demonstrated to be equivalent. However, increasing the number of mini light sheets simultaneously present into the sample approaching it from different directions, gradually reduced the shadow artifacts originally present in the former configurations (from the 3LS up to 5LS). This was due to an enhanced angular diversity guaranteed by the most tilted beams. The latter approach, with the larger angular diversity, presented results similar to the one obtained in SB mode, which was indeed the case of a single beam swivelled for the larger angular range.

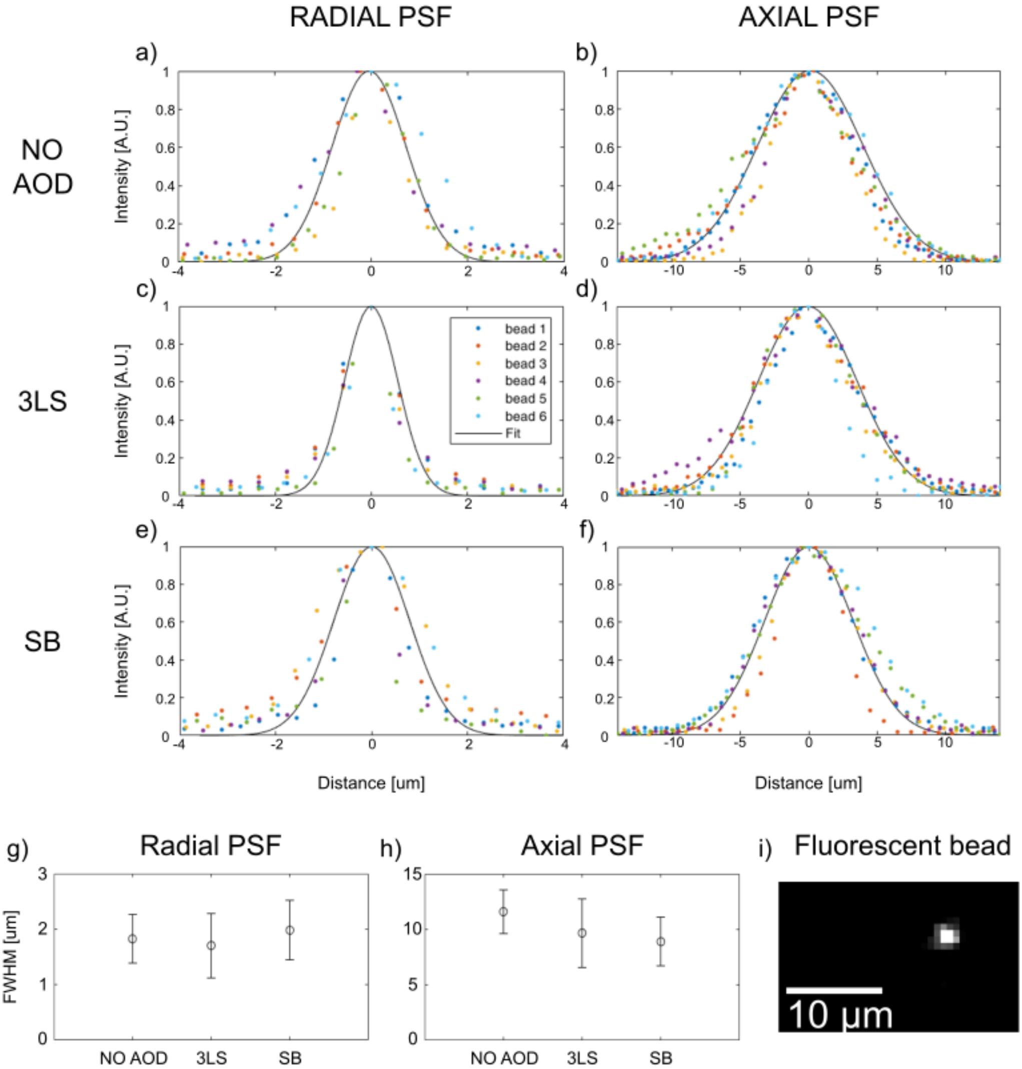

Figure 6.1_2: Radial and axial PSF in confocal DLSM. **(a)**, **(c)**, **(e)** and **(b)**, **(d)**, **(f)** raw data points (encoded by a different colour for each of the 6 measurements) and the average Gaussian fit (black line), obtained respectively in radial and axial direction. From the top to the bottom, the results were obtained respectively for the NO AOD, 3LS and SB configurations. **(g)** and **(h)** average FWHM and the standard deviation extracted from the measurements. **(i)** representative frame containing the fluorescence signal detected from a Tetraspeck fluorescent microsphere (r = 50 nm) embedded in agarose gel. Scale bar size: 10 µm. Modified from[142].

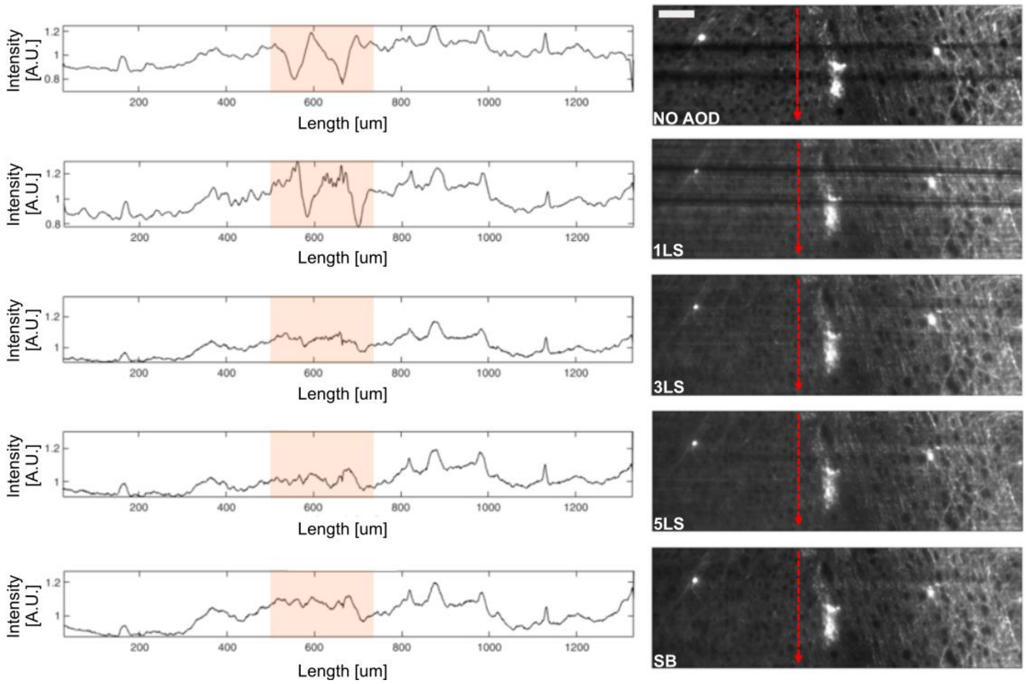

Figure 6.1_3: Image comparison between different pivoting dynamics. On the right LSFM images of a mouse brain with fluorescent protein tdTomato, obtained by pivoting the beam with different scanning configurations, respectively from up to down, NO AOD, 1LS, 3LS, 5Ls and SB. On the left, the normalized grey-scale intensity profiles are taken along the vertical directions; the orange squares indicate the area with stronger artifact suppression. Scale bar size: 100 μm. Modified from[142].

To quantify the shadowing suppression, three image stacks were taken from different areas of three mouse brains, illuminating them in SB and NO AOD. **Figs.6.1_4a-c** report single frames extracted from the three stacks acquired, comparing the results obtained with and without pivoting (NO AOD on the left, SB on the right). Red arrows indicate the areas where the shadow suppression was stronger.

The normalized intensity profiles were extracted from the frames displayed, obtained from a longitudinally averaged intensity projection. Then, the difference between the two profiles was calculated. The degree of shadowing suppression was estimated from the ratio R between the integrals of the absolute values of the intensity profile difference, and the SB one, taken as reference.

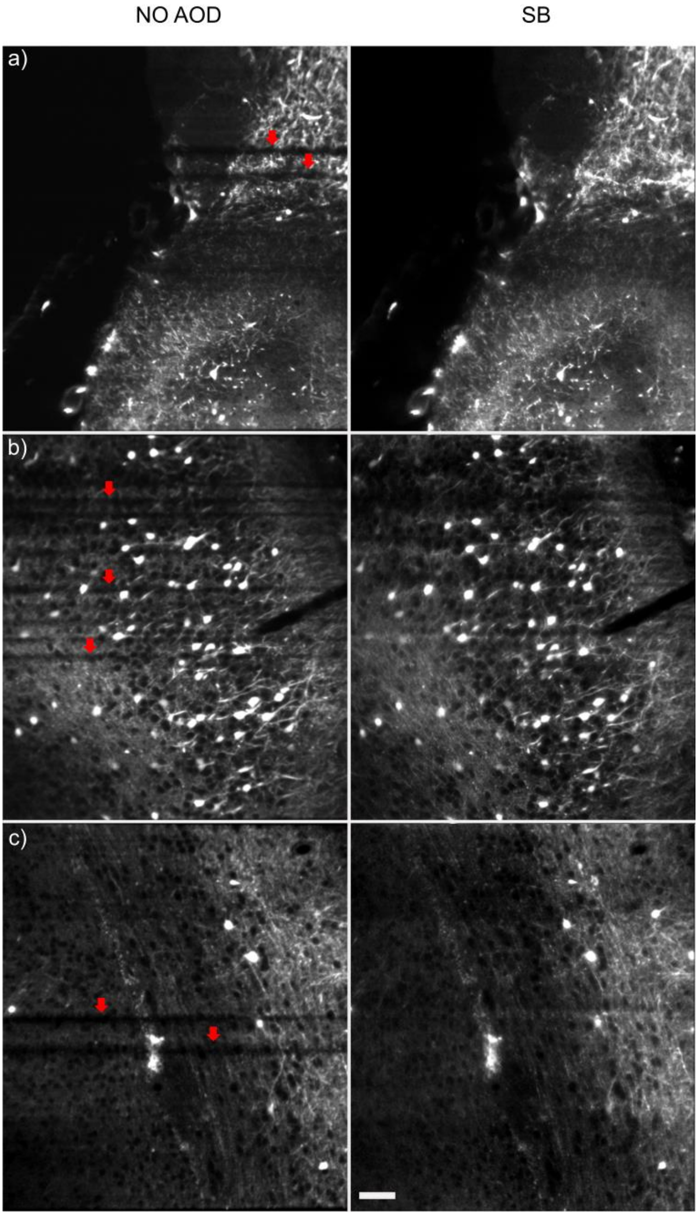

Figure 6.1_4: Shadowing suppression quantification. **(a)**, **(b)**, **(c)** Single frames acquired in three different mouse brains expressing fluorescent protein tdTomato, taken in NO AOD (left) and with SB (right) mode. Areas of larger striping attenuation are indicated by red arrows. Scale bar size: 100 μm. Modified from[142].

Substacks of ten consecutive frames were considered to calculate the mean and standard deviation of the ratio. The shadowing suppression ratio estimated for the samples **(a)**, **(b)**, and **(c)** were respectively of $R_a = (8.5 \pm 0.3)\%$, $R_b = (13.6 \pm 0.8)\%$ and $R_c = (5.3 \pm 0.2)\%$, showing an effective improvement provided by the beam pivoting.

Engineering the system with proper optics, following the model described, allowed to preserve the confocal detection and axial light uniformity. Then, to verify that confocal detection effectively improves the image contrast and that the beam pivoting did not affect this parameter, widefield acquisitions were also performed by leveraging the global shutter camera modality (that is the modality where all the pixels of the camera are simultaneously active and exposed).

Specifically, the same line exposure time was set to keep constant the per-row illumination intensity, while the digital slit height was expanded by about ten times via a corresponding reduction of the rolling shutter sweep pace (from 221 μm up to 2048 μm in camera space). The detection parameters used for imaging the fluorescent beads for the PSF and the mouse brain are reported in **Tab.6.1_1**.

It is worth noting that the scanning time $T_{scanning}$ previously found, was almost an order of magnitude lower than the minimum rolling shutter pace set on the sensor (up to two orders lower for confocal detection). It provided a pivoting dynamic much faster than the acquisition one to averaging out the shadowing.

Experiment	N. frames	Step size [μm]	Line exp. Time [ms]	Rolling shutter pace [μs]
PSF est. (confocal)	200	1	3	90.00
Brain imaging (confocal)	350	2	3	90.00
Brain imaging (widefield)	350	2	3	9.74

Table 6.1_1: Detection parameters for imaging in fast multidirectional DSLM

The image contrast ratio between the two main configurations (for SB and NO AOD) were calculated according to the normalized discrete cosine transform (DCT) Shannon entropy[61].

In **Tab.6.1_2**, the contrast ratios for both the pivoting modalities are reported, calculated as the ratio between the contrast evaluated on images taken with the digital slit and the one obtained on images without (widefield detection). The data were taken from several brain areas in three different samples, comparing each corresponding frame between the acquired stacks. Thus, the values refer to the mean and standard deviation calculated from all the contrasts. The P-value reported in the third column was calculated between the two data sets. These results indicated a statistically significant difference between the two data collection.

For both the pivoting modalities, the contrast resulted improved demonstrating that the beam pivoting did not affect the well-known benefit of confocal detection in DSLM. The relative contrast enhancement provided by a pivoted illumination (SB mode) was smaller than without (NO AOD) and this difference could be attributed to the not perfect confocality linked to pivoting. The beam could indeed excite some areas out of the digital slit while being swept for shadowing reduction.

Contrast ratio SB	Contrast ratio NO AOD	P-Value
1.11±0.03	1.20±0.02	<0.0001
1.11±0.03	1.15±0.07	<0.0001
1.10±0.02	1.28±0.07	<0.0001

Table 6.1_2: Contrast ratio calculated between confocal and widefield detection in SB and NO AOD modality.

6.2. Dual-beam confocal DSLM

Once showed how to suppress the shadowing in images taken by a DSLM, the next goal was to speed up the peak frame rate of acquisition. With respect to standards confocal detection, here is proposed a camera sensor with two rolling slits, coupled and synchronized with two beams independently controlled and generated by an AOD (relative methods in **chapter 5.3**).

Thus, the improvement due to this dual-confocal detection regime was tested and compared over the single modality in typical DSLM imaging applications. First, to probe this high-speed CDSLM, the zebrafish larvae's brain activity was imaged and monitored comparing the single and dual illumination and rolling shutter mode (**Figs.6.2_1a,b**). Second, several other rolling shutter readout modes were compared while imaging the mouse brain tissue (**Figa.6.2_1c-h**), while verifying the preservation of the contrast enhancement guaranteed by confocal detection.

No qualitative difference between the two detection regimes was observable. In highly transparent samples no cross-talk was observable in the sensor centre in the diverging or converging rolling shutter modes (**Fig.6.2_1e** and **6.2_1f** respectively). Furthermore, the acquisitions taken in the mouse brains were quantitatively compared by evaluating the contrast as in[163]. First of all, each image was normalized by its total intensity in order to avoid fluctuations correlated to different laser intensities. Then, from the image histogram, the standard deviation (std) was calculated to quantify the signal distribution width. Even if the std of the image histogram is not an exact estimator of the image contrast it is a correlated parameter that provides a direct comparison between the two methods.

In the end, the two values were normalized to the case of single beam illumination in a confocal regime. The resulting adimensional ratios are reported in **Tab.6.2_1**, showing no significant difference evident between the two imaging schemes.

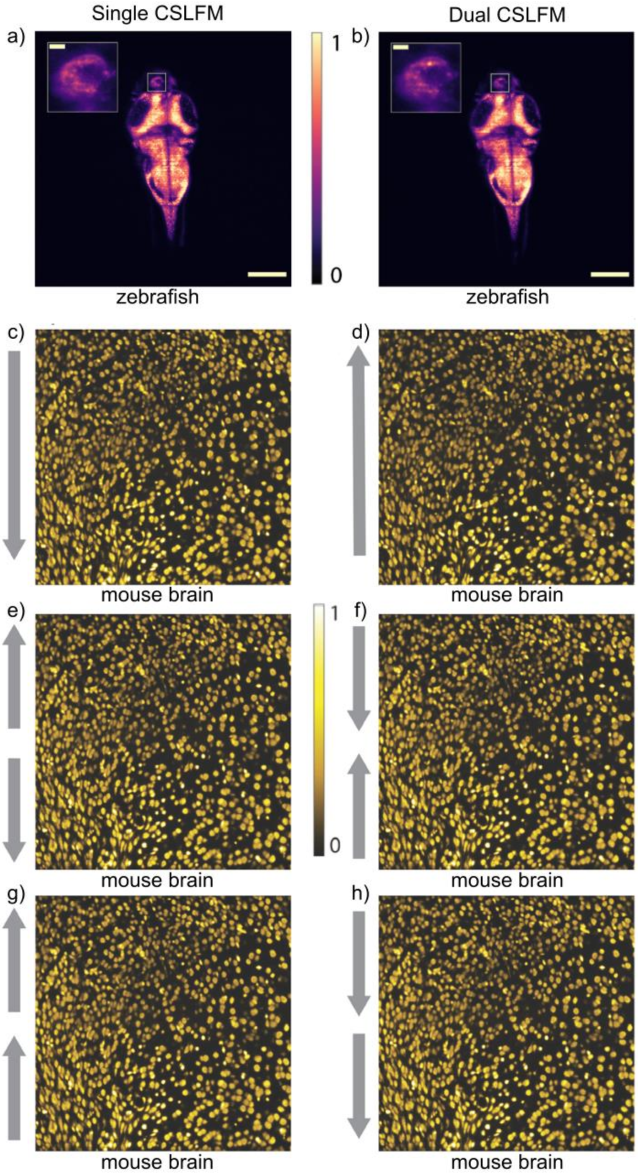

Figure 6.2_1: Single and dual beam acquisition. **(a)** Representative single (top to bottom readout) and **(b)** dual (diverging rolling shutter readout) beam CLSFM full-frame images neuron nuclei in a zebrafish larva brain, respectively, colour-coded purple. The inset shows a 4× magnified left habenula area within the diencephalon where neural activity can be observed. Scale bar size: 200 µm; 20 µm in the inset. **(c)**, **(d)** Single and **(e)**-**(h)** dual beam representative CLSFM full-frame images of cell nuclei within a mouse brain cortex area, acquired in the different rolling shutter readout direction modes of the sCMOS camera. No qualitative nor quantitative difference in the image quality is observable. Modified from[78].

This outcome was expected since the single row exposure time did not change during the sample vertical scanning. On the other hand, the concurrent readout of the two halves of the camera sensor allowed to halve the total exposure time, doubling the frame rate.

Modality	Norm. contrast	Frame $t_{exp}[ms]$	Fps
Single beam	1.000 ± 0.020	22	45
Dual beam	1.019 ± 0.015	11	90

Table 6.2_1: Contrast estimation between single and dual beam illumination. The adimensional ratios obtained normalizing to the single illumination case the standard deviation of the image histogram taken. Errors are calculated on n=4 different images. t_{exp}: exposition time; Fps: frame per second.

6.3. Light polarization effects on signal detection in 2P-LSFM

The last point addressed in the contest of LSFM performance optimization was fluorescence signal detection. In particular, the effect of light polarization excitation has been probed in a 2P LSFM over several fluorophores like fluorescein, enhanced GFP (EGFP) and the calcium sensor GCaMP6s with different diffusion dynamics once expressed in different samples (relative methods in **chapter 5.4**). The detected signals (A.U.) experimentally obtained in all the configurations have been summarized in **Tab.6.3_1** and discussed in the following one by one. In the end, these results have been also compared with the behaviour expected at priori (see **Eqs.2.2.2_7** and **2.2.2_8**).

The reference taken to describe the following results is the one reported in **Fig.5.4_1** in the methods. There, the camera detection axis has been labelled with $\hat{z}$, while the laser beam propagation direction after the illumination objective and the corresponding orthogonal orientation have been indicated with $\hat{x}$ and $\hat{y}$ respectively. The polarization direction of light excitation has been defined vertical or horizontal if parallel to $\hat{z}$ or $\hat{y}$ respectively. Coherently with this LSM configuration, the maximum signal detected is expected with a horizontal polarization.

Polarization	Circular	Vertical	Horizontal
Fluorescein	(375.4 ± 0.9) AU	(530.5 ± 0.8) AU	(545.6 ± 2.2) AU
EGFP fixed	(41.6 ± 15.3) AU	(45.0 ± 14.2) AU	(69.3 ± 20.4) AU
EGFP living	(53.4 ± 18.8) AU	(48.9 ± 17.5) AU	(75.2 ± 29.2) AU
GCaMP6s fixed	(14.5 ± 1.1) AU	(15.5 ± 1.3) AU	(26.5 ± 1.5) AU
GCaMP6s living	(3.6 ± 1.9) AU	(2.1 ± 1.4) AU	(4.8 ± 3.5) AU

Table 6.3_1: Detected signal obtained for circular, vertical and horizontal excitation polarization states for different fluorophores and sample configuration.

It is because in this photoselection case, the excited fluorophores would emit preferentially in the orthogonal direction, i.e. the one parallel to the detection.

However, by exciting small molecular-weight fluorophores in a medium where they can rotate completely unrestrained, the fluorescence emission is expected to be isotropic. Indeed, since in this condition the thermally induced rotation movements happen on time scales much shorter than fluorescence lifetime, all anisotropy induced by photoselection is washed out.

Thus, the first study case was a highly concentrated fluorescein solution, where the different detected signal was evaluated using linearly and circularly polarized light. Corresponding results have been shown in **Fig.6.3_1a**, normalized to the average value obtained in the circular polarization case (and so also for the next graphs). As expected, since the anisotropy is lost in this case, only small differences were evident in the two cases of linear polarization: a slightly enhanced signal (+3% larger) was detected employing a horizontal polarization with respect to vertical one showing a residual degree of spatial anisotropy induced by photoselection. Interestingly, a much larger increase (+45%) was observed for the two linear polarization conditions with respect to the circularly polarized light. This is consistent with the expected lower 2P excitation efficiency that characterizes circular polarization.

Nevertheless, it is worth noting that circular polarization can excite the dyes in a spatially homogeneous fashion, while the linearly-polarized light can excite, even if with a larger excitation probability, only the subset of dyes that have a component parallel to its polarization-plane. However, this result shows that in the case of isotropic emission (randomly distributed fluorophores) the widening of the group of possible target dyes is not sufficient to compensate for the decrease in excitation efficiency for the circular polarization with respect to the linear polarization.

The second case of study regarded the polarization effect on animal tissue where the fluorophores result constrained by being embedded in the anatomical structure. It makes the molecule less free to move and rotate, theoretically leading to a higher degree of photoselection-induced anisotropy in emission. To observe this, zebrafish larvae expressing EGFP have been imaged both in fixed and in living conditions. In this case, an arbitrary ROI has been selected for each larva (**Fig.6.3_1b**), measuring the mean fluorescence signal in the three depicted polarization conditions.

Differently from the former case study, there were no significant differences illuminating the sample with a circularly polarized light and a vertical one in fixed (**Fig.6.3_1c**) and the living tissues (**Fig.6.3_1d**).

On the other hand, a large and significant signal increase in the horizontal-polarization condition was recorded with respect to the circular and vertical one in fixed-condition (+67% and +54%, respectively) and in living conditions (+41% and +54%, respectively). Even though the fluorescent level difference between horizontal and vertical conditions is much more pronounced than in the former case study, a non-zero signal for all tested polarizations was still present. It implied that emission was not fully polarized in the animal tissue, with a significant degree of randomness in the fluorophore orientation.

However, the larger molecular weight of the EGFP fluorescent proteins with respect to fluorescein and the increased viscosity of the tissue allowed to preserve the emission anisotropy and enhanced the difference between the signal detected in the optimized horizontal polarization with respect to the vertical one.

Finally, the effect of the polarization photo selection was tested with the fluorescent calcium indicator GCaMP6s. Like in the previous study, for the fixed sample, the average fluorescence signal emitted by three arbitrarily selected ROIs was measured (**Fig.6.3_2a**). On the other hand, during live imaging of the indicator, the cellular calcium levels varied in time, and so did the emitted fluorescence, reflecting the time-dependent neuronal activity. In this case, ROIs were drawn around individual neurons, as shown in **Fig.6.3_2b**.

In the fixed sample, no significant difference was observed between the circular polarization and the vertical polarization, similarly to the EGFP case.

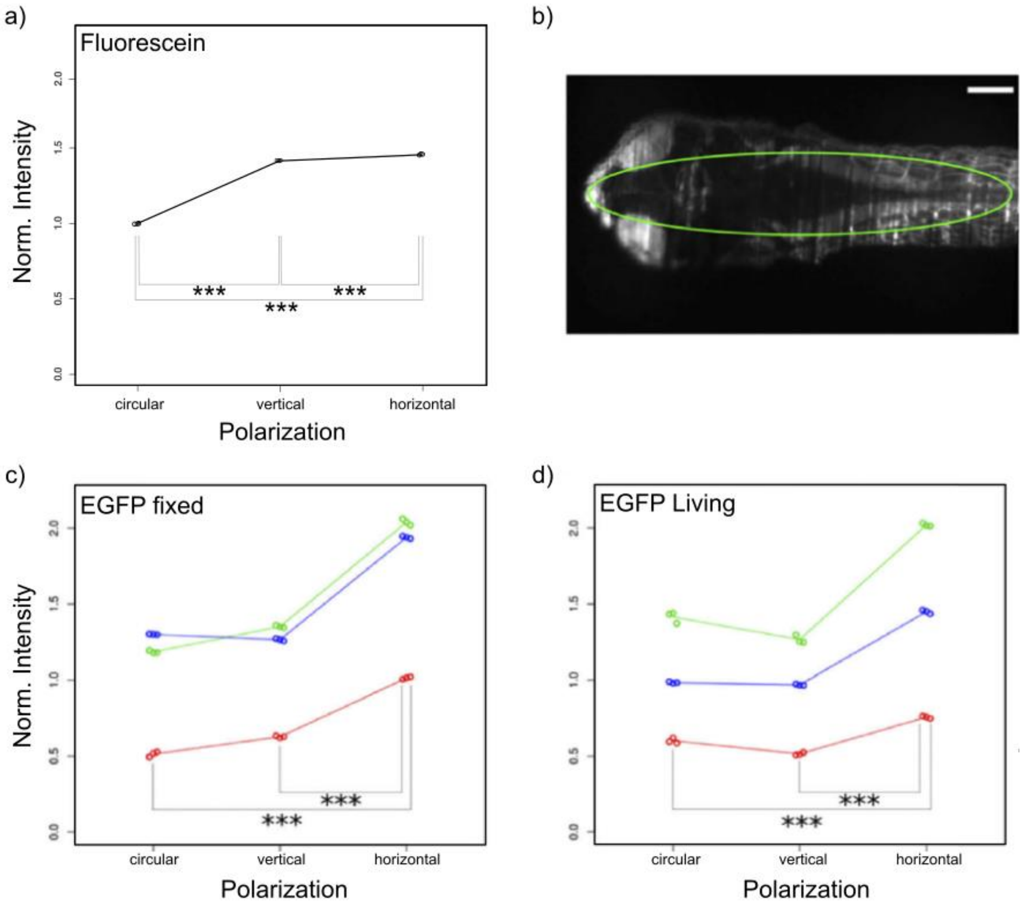

Figure 6.3_1: Effect of polarization state on fluorescein and Tg(actin: EGFP) larvae. **(a)** Scatter plot of the signal generated by a fluorescein solution excited with circularly, vertically or horizontally polarized light. Each condition was tested in triplicate and each point represents a single measure. The signal value is normalized to the average of the circular polarization case. Statistically, significant differences are indicated by three asterisks. **(b)** Z-slice extracted from a volumetric acquisition of larvae in fixed conditions. The green ovals indicate the ROI trace on this larva. Scale bars: 100 μm. **(c)**, **(d)** Scatter plots of the average signal measured from the ROIs as a function of the polarization condition in zebrafish larvae in fixed and living conditions respectively. Each point represents an individual acquisition, the points inherent to the same animal are indicated with the same colour in the respective graph. The average values for each animal and each condition are linked with lines of the same colour. In each graph, the signal value is normalized to the average of the circular polarization case. Statistically significant differences are indicated by three asterisks (p-value < 0.0001). Modified from[104].

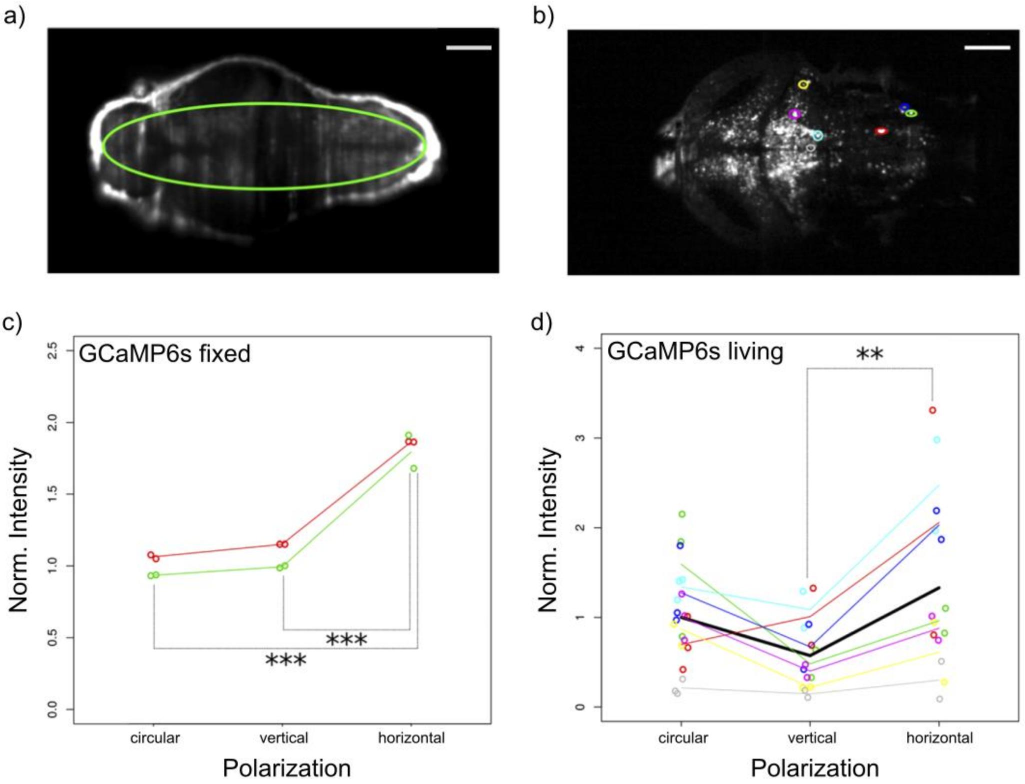

Figure 6.3_2: Effect of polarization state on Tg(elavl3:H2B-GCaMP6s) larvae in fixed and living condition. **(a)** Individual z-slice extracted from the volumetric acquisitions of a representative larva. The green oval indicates the ROI measured for this larva. **(b)** Maximum projection of a sub-volume of the volumetric stack (70 μm along the dorso-ventral direction from the original 150 μm) of the larva in live condition. The coloured ovals indicate the different ROIs. Scale bars: 100 μm. **(c)**, **(d)** Scatter plots of the average signal measured from the ROIs traced on the larvae as a function of the polarization condition in fixed and living conditions respectively. The signal value is normalized to the mean of the circular polarization case. Statistically significant differences are indicated by asterisks (***: p-value < 0.0001, **: p-value = 0.0016). In **(c)** each point represents an individual acquisition, the points inherent to the same animal are indicated with the same colour. The average values for each animal and each condition are linked with lines of the same colour. **(d)** Different colours indicate different ROIs, as shown in **(b)**. For each colour, each point represents an individual acquisition. The average values for each ROI and each condition are linked with lines of the same colour. The thick black line indicates the global averages for each condition. Modified from[104].

Again, the measured fluorescence signals in the horizontal-polarization condition showed a large and significant increase with respect to the circular (+83%) and the vertical-polarization (+71%) situation (**Fig.6.3_2c**). The conclusions were the same as before.

Interestingly, in the last case, i.e., the GCaMP6s living condition, no significant differences were observed between the circular-polarization condition and the vertical- and the horizontal-polarization conditions (**Fig.6.3_2d**). Anyway, a large and significant increase (+128.6%, p-value = 0.0016) in the fluorescence signal level in the horizontal-polarization condition with respect to the vertical polarization condition.

The slightly different trends observed for GCaMP6s between the fixed and the living conditions could be ascribed to several factors. The fixation procedure induces cross-linking between molecules that could alter the rotational mobility of the fluorophore. Moreover, the physicochemical properties of the cytosol change between the living and the fixed states and this medium alteration could affect the motion of the dye. Finally, the fine spatio-temporal biological control of the calcium distribution is completely abolished in the fixed state and therefore the distribution between the bound and the unbound states of the fluorescent sensor is altered in the two cases too, affecting its fluorescence characteristics.

At last, the aforementioned results were compared with the a priori estimations based on the anisotropy reduction factor computation (see **Eqs.2.2.2_7** and **2.2.2_8**). In **Tab.6.3_2,** the parameters used for the calculations of rotational correlation time α and of the anisotropy reduction factor β are reported for the different samples considered. While the lifetimes of these three fluorophores are similar, the volumes of EGFP and GCaMP6 are one to three hundred times larger than that of fluorescein, providing a reduced rotational diffusion capability and maintenance of emission anisotropy.

In detail, the small residual anisotropy empirically found in fluorescein (+3%) was consistent with the corresponding estimated value $\beta_{Fluorescein} = 2\%$. Much larger differences in emission intensity were found between horizontally and vertically polarized excitation for EGFP (+54% both in fixed and living condition) and

GCaMP6 (+71% and +128% in fixed and living condition respectively), congruously with the expected anisotropy reduction factors. In conclusion, the experimental observations agreed with these estimated trends.

Sample	Vol [nm^3]	τ [ns]	T [K]	η [Pa·s]	α [ns]	β
Fluorescein	0.34	4.1	293.15	$8.9 \cdot 10^{-4}$	$76 \cdot 10^{-3}$	2%
EGFP	33	2.6	293.15	$1.2 \cdot 10^{-3}$	10	79%
GCaMP6s	91	2.5	293.15	$1.2 \cdot 10^{-3}$	27	92%

Table 6.3_2: Macroscopic properties and parameters used to calculate the rotational correlation time and the anisotropy reduction factor of different fluorophores. V: volume; τ: fluorescent lifetime; T: room temperature; η: medium viscosity; α: rotational correlation time; β: anisotropy reduction.

7. Results for 3D Optogenetic Photostimulation

7.1. Hybrid scanning optical characterization

In order to achieve a fast light addressing and cellular manipulation of three-dimensionally distributed cells, an AOD-based scanning head has been implemented exploiting a near-infrared light source for 2PE for deep optical access. Moreover, a further GM-based scanning head has been coupled with the former for visualization of larger areas and to enable a specific selection of dislocated neuronal clusters (relative methods in **chapter 5.5**). This hybrid scanning head required a proper characterization and parameter calibration here reported in detail.

To obtain a fast beam focussing with four AODs, they require to be driven by properly chirped signals (see **chapter 3.3.**). Then, the first calibration phase regarded the effect of chirping on the beam focusing and lateral deflection.

To begin, the axial displacement ΔZ generated by chirping was estimated *a priori*. Recalling **Eq.5.5.1_1**, there is a linear relation between ΔZ and the chirp α, where the proportionality k depends only on an optic magnification factor, the acoustic properties of the AO crystal and the excitation wavelength: the estimation result was $k = (6.4 \pm 0.5)$ µm·µs/MHz.

To measure this factor empirically a thin layer of $BaTiO_3$ (Barium titanate powder, thickness <3µm, 99%, Sigma-Aldrich Corp., St. Louis, MO, USA) was first positioned at the inherent objective focal plane, in order to obtain a high-contrast signal. A reference volumetric image stack of the layer was acquired by moving the objective-lens stepper motor around this reference position. Then, the sample was imaged by performing a 2D raster scan with the AOD unit driven with unchirped acoustic waves.

Subsequently, the focal plane addressed by the excitation light was varied by changing the chirp parameter in each AOD. At this point, a second image stack was acquired by moving the objective with the stepper motor and 2D raster scanning this time with the AODs at a fixed chirp rate.

The whole procedure was repeated symmetrically varying the chirp α by discrete steps around 0 MHz/μs, i.e., the unchirped case.

In the sample, the same ROI was selected for each acquired stack; the axial intensity profile integrated over such ROI was then fitted with a Gaussian model to determine the axial position of the intensity peak. As displayed in **Fig.7.1_1a**, the linear regression fit of the observed response yields a slope of k = (7.70 ± 0.46) μm·μs/MHz. The slight discrepancy between the measured value and the theoretical estimation could be attributed to small inaccuracies in the positioning of the lenses, which therefore provided an actual magnification different from the nominal one used in calculations.

With four AODs, a light beam lateral deflection is induced precisely, defined by the difference between the central acoustic frequencies of the ramps applied in the coupled stages (recall **Eq.3.2_9**). Through the imaging of the same $BaTiO_3$ sample, a referenced translation of a fluorescent point-like spot enabled the evaluation of the conversion factor between the lateral displacement and the driving frequencies: it resulted in ε=1.75 μm/MHz.

Due to slight optical misalignments, a chirp-dependent error compensation was required wherever the coordinates of the target focal point resulted laterally shifted with respect to the centre of the FOV. Then, to quantify this effect, the FOV shift was measured as a function of the applied chirp.

Image stacks of a thin layer of BaTiO3 were acquired, moving the objective along the optical axis by means of the axial stepper motor, and illuminating with a 2D AOD-based raster scan. After, equal volumetric image stacks were acquired by progressively setting positive, null and negative chirp values. The whole distribution of the fluorescence peaks was tracked within the stack, quantifying the drift suffered by a reference target varying the chirp α. The frequencies to be applied to balance this drift were linearly fitted and reported in **Fig.7.1_1b** and **7.1_1c** for the *x* and *y* axes respectively, from which a drift slope was evaluated of m_x = (2.28 ± 0.07) μs and m_y = (1.17 ± 0.03) μs, at 95% confidence interval.

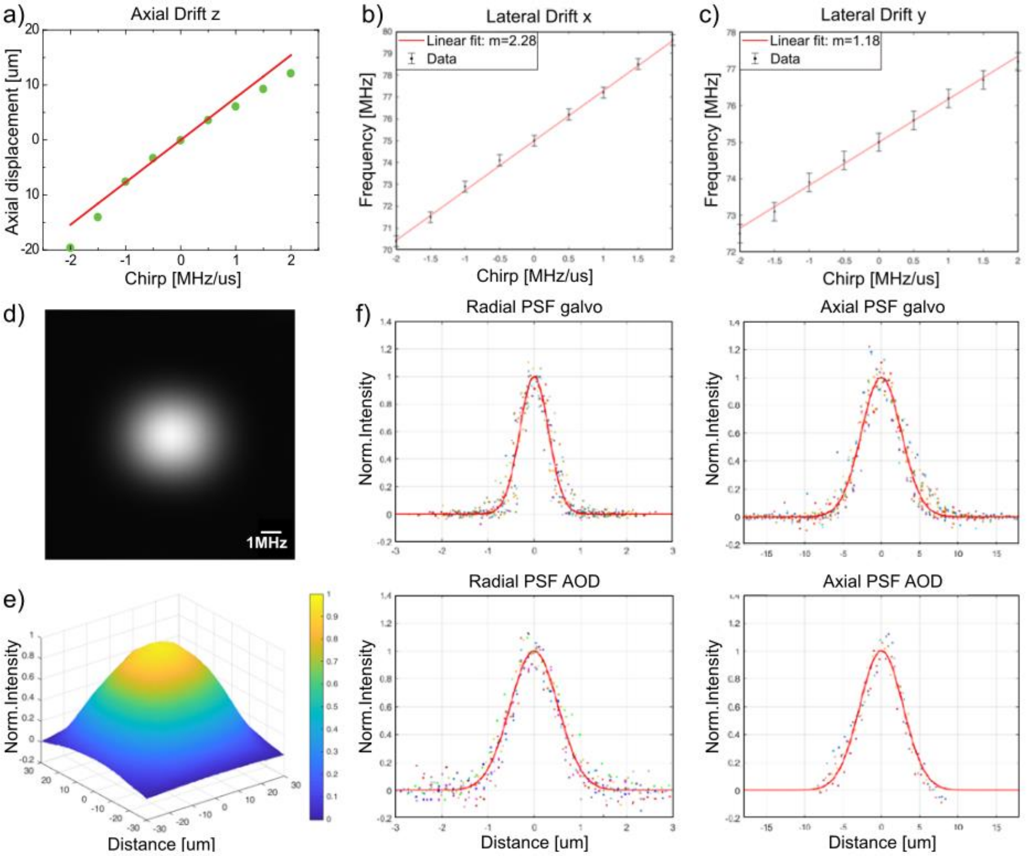

Figure 7.1_1: Optical characterization of the hybrid scanning unit. **(a)** Calibration of the AOD-generated axial displacement as a function of chirping rate, shown by linearly fitting the relative positions of fluorescence peaks collected from the separate planes addressed by AODs. **(b)**, **(c)** Frequency shift imposed as a function of the chirp along x and y, respectively, to dynamically balance the lateral drift induced by chirping (in respect to the centre frequency fc = 75 MHz). **(d)** The fluorescent signal collected by the PMT as a measure of the acceptance angle of the second AOD stage; the second stage was driven statically at fc = 75 MHz. **(e)** Normalized intensity map collected by the PMT as a measure of the transmission efficiency through the second AOD stage; the first stage was instead driven statically at fc = 75 MHz. **(f)** Radial (left) and axial (right) PSFs measured by scanning fluorescent beads with Galvos (top) and with AODs (bottom). Modified from Ricci et al. 2021.

Here, the error bars associated with the points denoted the lateral resolution of the AODs, in terms of frequency. In this regard, the AOD resolution depends on the effective access time required by the sound wave to cross the crystal, and the frequency bandwidth, $\Delta f = 30$ MHz. For an optical aperture with diameter D=7.5 mm and a propagation speed of the acoustic wave in TeO_2 of v=650 m/s, the maximum estimated access time was dt=11.5 μs. However, since the laser beam did not overfill the AOD aperture, as the $1/e^2$ spot diameter evaluated at its entrance was d = 2.5 ± 0.1 mm, then the acousto-optic interaction area was smaller, leading to an effective access time $dt_{eff} = 3.85 \pm 0.15$ μs. The number of distinguishable points can be calculated as $N_{Rayleigh} = dt_{eff} \cdot \Delta f = 117$, providing a frequency resolution of $\Delta f / N_{Rayleigh} = 0.25$ MHz.

The results of the fit were used to dynamically balance the lateral shift when chirping the driving RF for volumetric scanning AOD. In such a way, the frame stack acquired by varying the chirp parameter was consistent and laterally stable.

The second phase concerned the evaluation of the optical transmission through the second AOD couple as a function of the frequencies applied to the first one. In other words, since different frequencies correspond to different beam deflections, through the action of the first couple, this measure is meant to estimate the acceptance angle of the second stage in terms of frequencies.

In order to do this, the second AOD stage was set statically at f_c=75 MHz on both the axes, while the first stage was scanning the laser beam in full bandwidth range (Δf_{max}=30MHz). **Fig.7.1_1d** shows the intensity map collected from a homogeneous fluorescent sample (Autofluorescent Plastic Slides 92001 Chroma Technology Corp), in response to the described 2D raster scan. A Gaussian fit obtained along the transverse direction of the collected intensity profile resulted in a FWHM=(3.34±0.03)MHz, corresponding to an acceptance angle $\Delta\theta = \frac{\lambda \Delta F}{\nu} \cdot \frac{180}{\pi} = 0.313°$. It indicated a really low tolerance in the acceptance angle as input for the second stage, becoming critical. This determines a limit on the frequency range applicable to the first AOD couple, outside of which the transmission through the second stage drops significantly. For this reason, a trade-off between the optical transmission and the acceptance angle was found in order to maximize the lateral scan (FOV size).

Recalling **Eq.3.2_9**, the lateral deflection affecting the beam depends on the offset between the central acoustic frequencies driving the coupled AODs. Therefore, in static configuration for 2D scanning, the frequency of the first stage was set at $f_{1x}=f_{1y}=f_c$, while the second stage pivoted the beam in the full angular range allowed, i.e., addressing each point by different coordinates (f_{2x} ; f_{2y}).

However, when the chirped mode was activated for 3D random access or fast volumetric stacks, the dynamic slightly changed. In this case, the frequencies linearly swung around the centres formerly defined but in a limited frequency band: this had to be lower than the effective bandwidth measured by the aforementioned Gaussian fit. To maximize the power transmission from the second stage, the ramping band was constrained as much as possible within a very narrow high-efficiency frequency window Δf_{eff}=1 MHz. This expedient provided the smallest input incidence angle for the second couple maximizing the power transmission and the lateral FOV achieved by AOD scanning.

Then, the third phase concerned the transmission uniformity provided by pivoting with the second AOD stage. To this aim, the first couple was driven statically at f_c=75 MHz on both axes. It is worth highlighting that in this case, unlike what happens by scanning the laser beam using the first AOD stage, there were no further constraints on the applicable RFs other than the effective bandwidth of the deflectors, Δf_{max}=30MHz.

Fig.7.1_1e shows the fluorescent intensity map collected by the PMT from a homogeneous fluorescent sample (Autofluorescent Plastic Slides 92001 Chroma Technology Corp), in response to a 2D raster scan performed with the second pair of AODs. A quasi-homogeneous intensity distribution (>75%) was achieved for a lateral AOD-defined FOV of 30×30 μm^2. The reason for this relatively small FOV was attributable to the particular optical configuration, dictated by the constraints of the Leica microscope exploited for the experiments (see **chapter 5.5.** for details). To make the system able to work properly even with tilted beams, the spot width and the scanning dynamics were adapted to the optics downstream to the second AOD stage.

Lastly, the optical features of the GM and AOD beam-scanning systems were quantified and compared. To this end, their characteristic PSF was measured using specimens containing fluorescent beads (TetraSpeck microspheres, Invitrogen T7279, with radius r=50 nm) at a final concentration of 0.0025% (vol/vol), in 4% agarose gel. When using the AODs, the axial displacement of the focal plane originated from the modulation of the chirp parameter α whereas the image stacks acquired with the GMs were obtained by axially translating the microscope objective. The radial and axial intensity profiles of $n_{GM}=50$ and $n_{AOD}=25$ beads respectively imaged with the GM- and AOD-based scanning approaches were computed with the open-source software ImageJ (U.S. National Institute of Health, Bethesda, MD, USA). **Fig.7.1_1f** shows the raw data and the corresponding Gaussian models, which allowed to quantify the mean axial and radial FWHM values related to both techniques. In the radial direction they were respectively estimated (0.73 ± 0.03) μm and (1.21 ± 0.05) μm for GMs and AODs, while axially they were (6.3 ± 0.2) μm and (6.6 ± 0.3) μm, respectively. From a theoretical basis[26], they were expected $FWHM_{xy}$ = (0.465 ± 0.012) μm and $FWHM_z$ = (3.19 ± 0.11) μm. Nevertheless, the measured PSFs were reasonably compatible with the theoretical predictions: the slight inconsistency was ascribable to the aberrations introduced by the agarose gel. The small incongruences found between the two scanning methods were instead attributable to a non-ideal compensation of angular dispersions, which became particularly significant when chirping the AODs. Anyway, we could therefore conclude that the two scanning heads in the optical path did not significantly affect the lateral and axial resolution.

7.2. Multi-triggered light stimulation

Although AODs provide very fast inertia-free deflection and focusing, they also suffer from few limitations. The first intrinsic drawback is related to their diffraction efficiency. Indeed, even though the optical transmission of each separate AOD may be as large as 95% for the first diffracted order when assembled in the crossed XY geometry, the deflector stage overall light transmission efficiency is declared to be around 50%. This implies that the four-AOD beam-scanning-unit transmission efficiency is approximately 25%. Therefore, an adequate laser source, ensuring enough output power to compensate for these losses, is required for imaging and optostimulation applications.

Secondarily, the optical transmission is also a function of the radio-frequencies applied to the AOD. In detail, each AOD is characterized by a narrow input acceptance angle beyond which the output transmission efficiency drops considerably (Fig. 7.1_1d). In other words, the second stage transmission depends on the light deflection induced on the beam by the first stage.

When these devices are exploited to manipulate the beam focusing, chirped signals are sent to drive the AOD, with frequencies that span a certain bandwidth. More specifically, a restricted bandwidth around the centre would deviate the beam of a small amount, guaranteeing the maximum transmission efficiency through the second couple. Then, clearly, the time required to address a narrower frequency band will be proportionally shorter than the one necessary for a larger bandwidth. However, even if the ramp slope remains the same - and so also the chirp value $\alpha=\Delta f/\Delta t$ - the second case would involve also frequencies that provide a less efficient light transmission. Furthermore, the point-to-point dwell time ΔT cannot be freely modified but, as mentioned in 5.5.1., it is constrained by the commutation time of 20μs for the digital reconfiguration of the coordinates. This case is representative of what happens when a single signal - or single trigger ST - is sent to the AOD with no bandwidth optimization (**Fig.7.1_1d**). This configuration also implies that the energy deposited on different axially displaced planes is not constant but is inversely proportional to the chirp. Indeed, recalling **Eq. 5.5.1_1**, addressing distant planes requires large axial displacements of the AOL focus, which in turn requires steeper frequency ramps with shorter duration, leading to a progressive decrease in delivered power for increasing axial distance.

Here, to modulate the axial drift we developed a novel method of signal multitrigger MT. First, to maximize the power transmission from the second stage, we constrained as much as possible the first stage ramping dynamics within a very narrow high-efficiency frequency window, Δf_{eff} = 1 MHz, around the center of the AODs effective bandwidth (f_c = 75 MHz). Then, in order to tune the chirp, we varied the effective ramp time Δt_{chirp} that is the actual time required to sweep the AOD driving frequency between the limits of the high-efficiency window Δf_{eff}.

Through the fine configuration and repeated generation of the frequency ramps driving the AODs, the inhomogeneity in the axial power delivery is significantly reduced. Specifically, to raise the energy supplied to a given target volume within the dwell time, we envisaged illuminating it multiple times, instead of only once.

For each sequentially addressed coordinate, we compute how many repetitions of a single narrow frequency sweep completely fit the point dwell time. In detail, the number of applied triggers (rounded to the lower nearest integer) is $N_{trigger} = \Delta T/\Delta t_{chirp}$. In such a way, the total power delivered during ΔT is a multiple of the power conveyed in response to a single frequency ramp: $P_{MT} = P_{ST} \cdot N_{trigger}$.

A further consideration about the minimum frequency sweeping time is however required at this point. Namely, the resulting Δt_{chirp} must not be allowed to drop below the lower threshold represented by the AOD access time dt. It is the time required by the acoustic wave to cross the AOD internal crystal and interact with the beam spot, steering light towards the target position. More specifically, the access time is needed to prevent light from simultaneously interacting with consecutive frequency ramps. It would lead to a spurious splitting of the input laser beam and, consequently, to the parallel interaction with distinct spatial coordinates of the sample. In practice, if the above condition is not satisfied, “ghost images” would emerge during image acquisition. In our configuration, the effective access time is dt=4μs (see chapter **7.1.**).

An algorithm was implemented to compute the single ramp time Δt_{chirp} for each value of chirp. Given a set chirp value, the algorithm starts to compute the frequency bandwidth that would be addressed in the single trigger case, assuming the entire dwell time ΔT for light-targeting:

$$\Delta f_{ST} = \alpha \cdot \Delta T \quad (7.2\_1)$$

Then, depending on the input chirp, two scenarios may arise:

1. $\Delta f \leq \Delta f_{eff}$: for very low chirp values, the ramping frequency stays within the high-efficiency window and therefore $N_{trigger} = 1$ and $\Delta t_{chirp} \sim \Delta T$; this case corresponds to the maximum delivered power level (adopted as reference).
2. $\Delta f > \Delta f_{eff}$: for low chirp values, frequency sweeps exceed the available Δf_{eff} and in single trigger mode it would provide less transmission efficiency; the algorithm then iteratively looks for the highest submultiple of the frequency bandwidth, $\Delta f_{MT}=\Delta f/n$, fulfilling condition 1). When this is reached, the following relation holds:

$$\Delta t_{chirp} = \frac{\Delta f}{\alpha \cdot n} = \frac{\Delta T}{n} \quad (7.2\_2)$$

Then considering the access time constrain, a binary decision must be taken:

3. $\Delta t_{chirp} > dt$: in this case, the number of applied ramp triggers is simply provided by:

$$N_{trigger} = \frac{\Delta T}{\Delta T/n} = n \qquad (7.2\_3)$$

4. $\Delta t_{chirp} < dt$: for high chirp values. In this scenario, where ghost images would appear, the algorithm forces $\Delta t_{chirp}=dt=4\mu s$ and $N_{trigger}=\Delta T/\Delta t_{chirp}=5$, recomputing the ramping bandwidth $\Delta f = |\alpha|\cdot\Delta t_{chirp}$ accordingly. Exceeding the available high-efficiency Δf_{eff}, this configuration is inherently related to a lower power efficiency with respect to the maximum reference level.

For each chirp value, **Tab.7.2_1** reports the results of the calculations relative to the effective bandwidth addressable, the number of triggers and the chirping time once considered a dwell time of 20μs.

Chirp [MHz/μs]	Δf_{ST}[MHz]	Δf_{MT}[MHz]	$N_{trigger}$	Δt_{chirp} [μs]
0	0	0	1	20
0.05	1	1	1	20
0.1	2	1	2	10
0.15	3	1	3	6.66
0.2	4	1	4	5
0.25	5	1	5	4
>0.25	>5	>1	5	4
0.5	10	2	5	4
1	20	4	5	4
2	40	8	5	4

Tab.7.2_1: The results of algorithm calculation for each chirp value are reported together with the effective bandwidth addressed, the number of triggers and the corresponding chirping time. Dwell time ΔT =20μs. Colour code follows the cases described in the algorithm: blue cells refer to ST mode; red cells refer to the best configuration in terms of energy released, i.e., the very low chirp cases; orange cells refer to low-chirp cases; yellow cells refer to high chirp cases. Δt_{chirp} indicated in red are representative of the cases where time coercion is applied to the minimum access time dt=4μs.

Figs. 7.2_1a, **b** show the transmission efficiency of the second stage as a function of the frequency addressed (for further detail see **Fig.7.1_1d**). The areas coloured in blue and orange are relative to the ST and MT case, respectively. In the two panels are represented two different chirp cases: a low chirp case α=0.2 MHz/μs and a high chirp case α=0.5 MHz/μs for **Fig.7.2_1a** and **7.2_1b** respectively. The number of triggers is indicated for the MT modality. As it can be observed, the repetition of a shorter signal inside the high-transmission window is favourable with respect to a single scan in the whole dwell time because more energy will be released on the sample globally.

The driving RF signals used in the ST and MT scanning modes are schematized in **Fig. 7.2_c**, along with the simulated integrated signal on the PMT. It depicts the increase in delivered power to the target volume in MT mode as a function of time. It is worth recalling that the beam lateral deflection depends on the difference between the central frequencies of the chirped signals sent simultaneously to coupled AODs (these are the ones corresponding to the same axis in each stage) (**Eq.3.3_9**). Thus, even if the frequencies change as a function of time by chirping the signals, in each moment the frequency difference remains constant. This also means that during dwell time the beam position is univocally addressed. The RF frequency shown on the y-axis of the scheme refers to the frequency applied simultaneously to each AOD of both stages.

To demonstrate the improved photostimulation performance of the devised method, we light-targeted a homogeneous fluorescent sample (Autofluorescent Plastic Slides 92001, Chroma Technology Corp.) and detected the resulting fluorescent signal with the PMT. The measure was repeated varying the chirp symmetrically around 0 MHz/μs, alternating ST and MT configurations. For each considered chirp value, we illuminated a ROI located in the center of the optical FOV by means of a 10x10 points 2D raster scanning, i.e. n=100 planar coordinates, adopting a dwell time of 20 μs. For both the trigger modalities, the PMT integration time was set at 20μs, equal to the scanning dwell time. The results reported in **Fig.**

7.2_d reveal the different intensity trends obtained for the ST and MT modes, as a function of the chirp α.

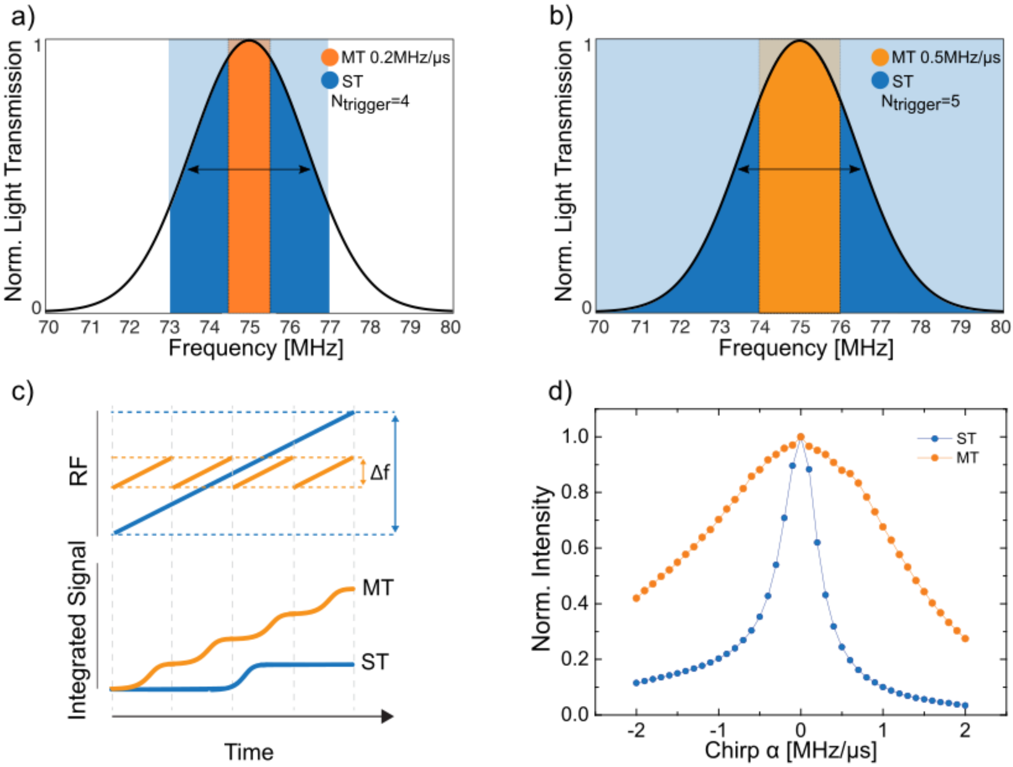

Figure 7.2_1*:* **(a), (b).** Transmission efficiency of the second stage as a function of the frequency addressed. The areas under the graph are coloured in blue and orange, relatively to the ST and MT mode respectively. **(a)** low chirp case α=0.2 MHz/μs; **(b)**, high chirp case α=0.5 MHz/μs. The number of triggers is indicated for the MT modality. **(c).** Top: schematic of the RF signals used to drive each AOD in single (blue) and multi-trigger (orange) modes. After the chirp α is defined, a frequency ramp is generated once (single-trigger) or repeated multiple times (multi-trigger) within a dwell time window. Bottom: the simulated integrated signal collected by the PMT. **(d).** Normalized fluorescence signal collected by PMT as a function of the applied chirp, addressing light in separate planes with single (blue) and multi-trigger (orange) configurations; 2D raster scans are obtained by illuminating 10×10 points with a dwell time of 20 μs. The integration time of the PMT was set coherently to 20 μs. Modified from Ricci et al. 2021.

The signal collected in the unchirped configuration, α=0 MHz/μs, exhibited no differences between the two triggering techniques since in both modes the AOD-driving RF could be maintained within the high-efficiency bandwidth for the entire point-to-point switching period. On the other hand, the relative enhancement of the collected fluorescence intensity due to the MT mode tended to grow with increasing absolute chirp values, in accordance with the progressive increase in the effective light-targeting time, with respect to the ST approach.

Furthermore, the results demonstrated an enhanced power distribution homogeneity. Indeed, the values obtained in MT varying the chirp between +1 MHz/μs and -1 MHz/μs are larger than 70% of the maximum power delivered in the nominal focal plane of the objective (no chirp).

Interestingly, in **Fig.7.2_1d** an asymmetry is observed: it was probably related to light scattering in the material which induced lower intensity levels attenuation in more superficial planes targeted by means of negative chirps, with respect to deeper ones.

7.3. 2P optogenetic stimulation with AODs in zebrafish larvae

To demonstrate the performance of the novel AOD-based *in-vivo* photo-stimulation method, optogenetic stimulation was performed in zebrafish larvae expressing the red-shifted Channelrhodopsins variant ReaChR. Electrophysiological recordings (local field potential, LFP) were used to read the neuronal activity from displaced planes involving clusters of cells. **Fig.7.3_1a** schematically shows the experimental setup adopted to optically stimulate and electrically record neuronal activity in zebrafish larvae. Within the volume defined by the AOD scanning constraints in this optical configuration (see **Fig.7.1_1e**), LFP responses were successfully evoked by light-targeting ROIs of 20×20 μm^2 at 50-70 mW (peak laser power recorded at the objective focal plane). During AOD axial scanning, the chirping frequencies which drove the devices varied modulating α from -2 MHz/μs to +2 MHz/μs (with 1 MHz/μs steps) (**Fig.7.3_1b**): it allowed to light-targeting axially-displaced planes of selected ROIs in the hindbrain area.

To exclude any non-optogenetic effect of the laser stimulation (i.e., photoinduced currents or thermal effects) a specific zebrafish larva was used, which lacked the optogenetic actuator but expressed the genetically encoded calcium indicator GCaMP6s. Exploiting the fluorescent indicator signal this model allowed indeed to orient light targeting and to address the reference ROI for stimulation.

Fig.7.3_1c reports two average activity traces recorded in the larva expressing GCaMP and ReaChR, relatively time-shifted to match the triggers. No evident potential changes were elicited in the GCaMP larva under light stimulation, while the ReaChR larva showed a clear evoked LFP response, under the same stimulation parameters. In particular, in this experiment the full stimulation time for both the case was ΔT_{tot}= 12.5 ms. This comparison proved the specificity of the stimulation system ruling out any artifacts due to photoinduced current on the microelectrode or any thermal effects correlated with infrared illumination warming of the sample.

Fluorescence of the reporter TagRFP was used to confirm the ReaChR expression; **Fig.7.3_1d** shows the fluorescence image of larval zebrafish hindbrain acquired using galvo scanning mode. Inside the orange square, which indicates the ROI selected for AOD light-targeting, the fluorescent electrode tip is visible. Given the size of the stimulation ROI of 400 μm^2 and considering the typical size of neuron bodies in larval zebrafish (5-7 μm), and since neurons are tightly packed in this organism, it can be estimated that the stimulated clusters were composed of 8-16 cells in each ROI. These are stimulated with beam spots that have a lateral size corresponding to the measured PSF of d=1.2 μm (**Fig.7.1_1f**).

To compare conventional single-trigger mode with our multi-trigger stimulation strategy, two different stimulation experiments were carried on zebrafish larvae expressing ReaChR in all neurons. First, the effect was evaluated by continuously stimulating a stack of overlayed planes through AOD axial scanning. The LFP amplitudes recorded were compared between the two triggering stimulation strategies (**Fig.7.3_1e**). It was observed that the MT configuration was associated with a significantly larger amplitude response with respect to the ST one (+54% between the average values of the two configurations, p-value<0.0001). This indicated a significant increase in neuronal activity response induced by volume photostimulation exploiting the multi-trigger modality. The latter, as expected, provided enhanced optogenetic neuronal stimulation efficiency since it delivered the excitation light for longer periods, within the same dwell time, compared to single-trigger mode.

Next, the effect of the two trigger modalities was tested on optogenetic stimulations within single planes addressed separately in the aforementioned range of chirp values (**Fig.7.3_1f**). With respect to the unchirped condition, amplitudes of events evoked with positive or negative chirp values were smaller. Nevertheless, amplitudes evoked in MT configuration were larger than those recorded with the

ST configuration for every chirp value, confirming the conclusions of the first experiment (p-value<0.0001 for each comparison between ST and MT).

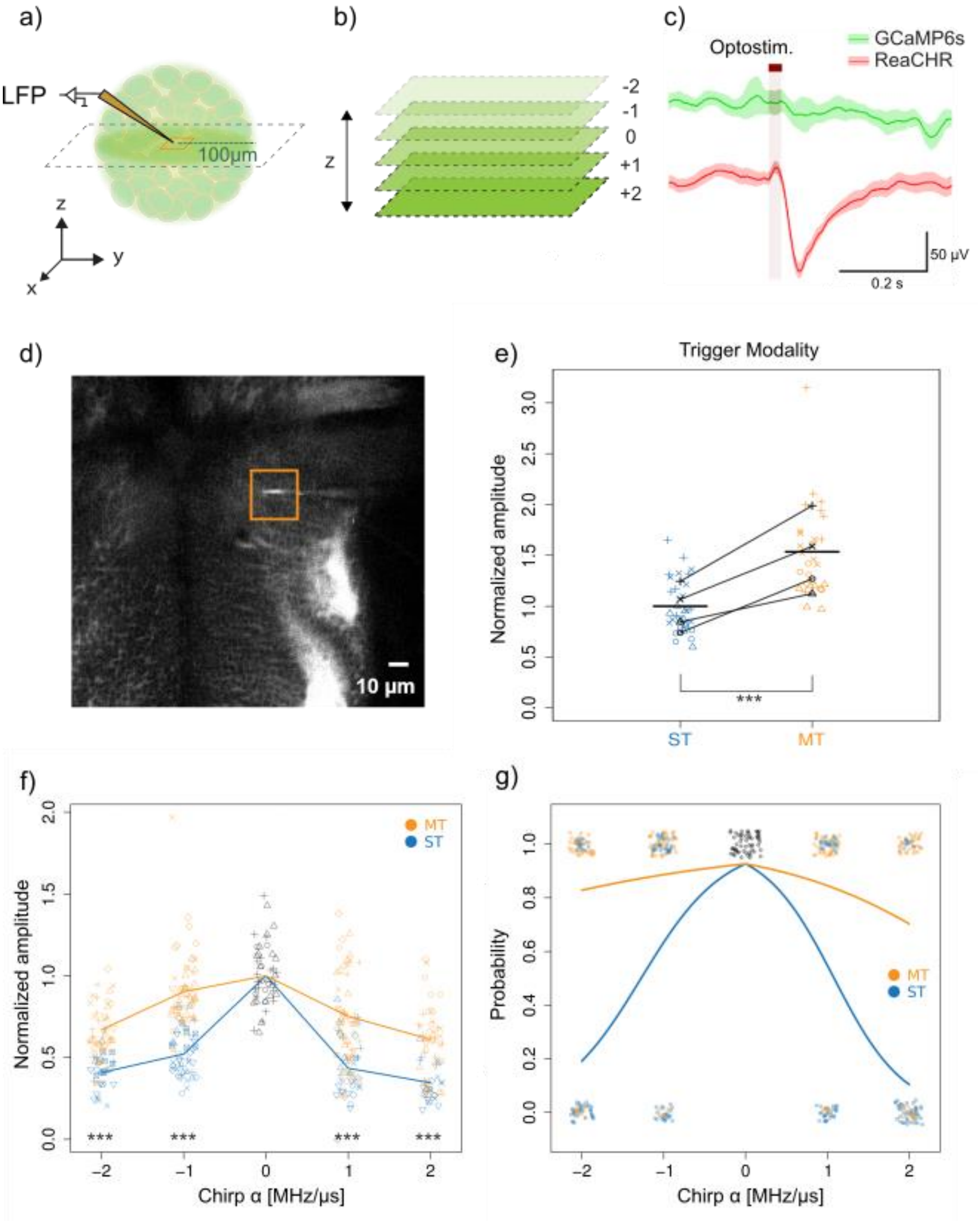

Figure 7.3_1: Optogenetic stimulation results. **(a)** Schematic of the electrophysiological recording setup. The pipette tip was positioned in the centre of the ROI (orange square) addressed by light

stimulation. The dashed grey square indicates the plane selected by the AOD scanning stage. 2D raster scans of 20×20 pts were repeated to reach the maximum evocable peak amplitudes, obtained after n=5 stimulation cycles with a dwell time ΔT = 20 µs. **(b)** Schematic of AOD axial scanning where the chirp parameter is modulated from -2 MHz/µs to +2 MHz/µs, addressing different planes. Each chirp unitary step corresponds to an axial shift of 7.70 µm with respect to the inherent objective focal position. **(c)** Representative average LFP traces were recorded in zebrafish larvae expressing GCaMP (green) and with ReaChR (red) in neurons, relatively time-shifted to match the stimulation trigger (brown). The test was repeated for N=3 larvae. The full stimulation time for both the case was ΔT_{tot}= 12.5 ms. **(d)** Fluorescence image of larval zebrafish hindbrain acquired using galvo scanning mode. The orange square highlights the ROI selected for AOD light-targeting. The fluorescent recording electrode tip is visible inside the ROI. **(e)** Normalized amplitudes of the electrophysiological responses induced in single trigger (ST, blue) or multi-trigger (MT, orange) conditions (n=1 scanning cycle for each plane). Data from N=4 zebrafish larvae are indicated by different symbols. Black lines join the average values for each animal. Thick horizontal black lines indicate the global average values in the two conditions. **(f)**. Normalized LFP amplitudes evoked in the two trigger conditions as a function of the chirp value. Different symbols indicate data from N=7 zebrafish larvae. Line segments join the mean values for each trigger condition and chirp value (n=5 scanning cycles each plane). **(g)**. The coloured curves indicate the estimated probability to observe an electrophysiological response evoked by light stimulation for the two trigger modalities as a function of the chirp values (n=5 scanning cycles for each plane). Positive and negative events recorded from all the N=7 zebrafish larvae with the two trigger modalities are reported by coloured spots, respectively in the top and bottom areas of the plot, for the corresponding chirp values. **(e)**, **(f)** Statistically significant differences between all the comparisons between ST and MT acquisition are indicated by three asterisks (p-value < 0.0001). Modified from Ricci et al. 2021.

The normalized average peak amplitude differences between events evoked in multi- and single-trigger configurations are reported in **Tab.7.3_1** for every chirp value.

Finally, the probabilities to observe an optogenetically-induced neuronal activation were compared as a function of the different chirp values, in the two trigger configurations (**Fig.7.3_1g**). The number of recorded events is reported in **Tab.7.3_2**. As in the former experiment, it was observed that positive or negative chirp values decreased the probability to observe an event with respect to the unchirped case (0 MHz/µs). However, the MT condition significantly compensated for this phenomenon with respect to the ST mode, greatly reducing the gap with the unchirped condition.

Notably, the probability curve was asymmetric, decreasing more rapidly for positive chirp values. This behaviour reflected the analogous trend found testing the fluorescent signal detected in a homogeneous fluorescent sample, where larger energy delivery was shown to be related to negative chirps with respect to the positive ones, due to shorter light propagation in the sample and lower scattering. Interestingly, in multi-trigger modality, it was found an activation probability always larger than 75% for all the chirp values, in opposition to the low efficacy in using single-trigger light stimulation with non-zero chirp values. It demonstrated that in MT there is an almost uniform probability distribution to optogenetically trigger the neuronal activation in all the volume addressable.

Overall, these results exhibited how the proposed method allowed unprecedented three-dimensional 2P optostimulation in zebrafish larvae by means of AODs. Pushing up the energy distribution deliverable in the volume, we observed remarkably increased neuronal response and uniform activation probability, validating the use of AODs for effective 3D photostimulation.

Chirp Values [MHz/ µs]	-2	-1	+1	+2
Norm. Amp. Differences MT-ST	(26.7±4.1)%	(37.3±3.5)%	(31.8±3.9)%	(24.8±4.5)%

Table 7.3_1: Difference values (and their standard errors) between the normalized average amplitudes of the electrophysiological responses evoked in the multi-trigger and single-trigger configurations with different chirp values. Amplitude values were normalized with respect to response at 0 MHz/µs. P-value < 0.0001 for all these differences.

Chirp [MHz/μs]	Observed events		Missed events		Total	
	ST	MT	ST	MT	ST	MT
+2	8	37	46	15	54	52
+1	21	43	29	7	50	50
0	57		0		57	
-1	28	48	22	7	50	55
-2	13	42	35	11	48	53

Table 7.3_2: Number of observed and missed events for each chirp value tested in single-trigger (ST) and multi-trigger (MT) modes for all the examined zebrafish larvae (N=7).

8. Discussion

Optical imaging and light triggering of neuronal activity in large volumes is a hard technological challenge to win. In order to achieve this goal, researchers need flexible and rapid devices to illuminate different targets displaced in the sample. Acousto-optic deflectors (AODs) are high-performance devices well suited to spatially control light beam propagation. AOD repetition accuracy, stability and fast dynamics allow microscopists to exploit them in several applications as a valuable alternative to other standard solutions, like galvanometric mirrors, spatial light modulators or digital micromirror devices. Indeed, with AODs it is possible to change the beam propagation direction by simply varying the acoustic frequency sent to a piezotransducer, reaching up to MHz repositioning dynamics[150].

This timing perfectly fits not only the biological dynamics of the neuronal activation but also other biological applications. For example, the latest advancement in bio-engineering provided fast responsive tools for imaging voltage using fluorescent-based sensors – the genetically encoded voltage indicators (GEVIs)[164,165]. Furthermore, recent technological progress in camera sensing[166] allowed the investigation of fast events such the calcium transients. For this reason, modern sCMOS sensors[167] are often coupled with fast scanning systems to keep up with the high frame rate of acquisition.

Within this panorama of applications, AODs are employed worldwide in several fields. In this thesis, the first application of AODs regards their implementation in the illumination path of a light-sheet fluorescence microscope.

LSFM is a planar illumination technique that brought a revolutionary contribution to optical imaging of biological specimens[70]. However, image quality degrades in presence of striping artifacts, correlated to the side illumination and originating during light propagation in samples containing scattering or absorbing structures. In this thesis, a novel method has been proposed to remove the artifacts, compatible with a DSLM configuration in confocal detection. The suggested AOD-based pivoting device controls the rotation of a tailored elliptical-Gaussian beam, obtained through a properly designed beam-shaping system. For this, it has been considered that the degree of striping artifact suppression is closely correlated with the effective numerical aperture used to illuminate the sample. This is because the size of the occluding objects defines the smallest incidence angles required for the light to circumvent them. Moreover, to preserve the possibility to combine this approach with confocal detection, the beam has been shaped to cover the detection slit in every orientation of the beam, while it is tilted through the vertical axis of propagation.

In this context, the advantage of using an AOD with respect to other scanning heads was that the obtained laser scanning rate (~1μs) was faster than the highest detector acquisition rate achievable today (~10μs)[166]. In this way, it was possible to average out over time the shadowing attenuation from different angles without imposing any constraint on the imaging rate. Three cleared mouse brains expressing the tdTomato fluorescent protein have been imaged observing an almost complete striping remotion from the images with respect to a classical not-pivoted Gaussian beam illumination. It has been also shown that the beam pivoting does not affect significantly the lateral and axial resolution.

At the same time, the relative image contrast enhancement provided by confocal detection resulted preserved in both the configuration.

From a comparison of the two contrast improvements, it was found to be slightly larger for the classical approach. To be sure of covering the digital slit during the pivoting, a larger beam was designed but, as a side effect, part of the illumination spread out. However, pivoting a beam larger than the one used in the unshaped/unpivoted configuration results in a lower average illumination power over a larger exciting volume.

Even if alternative beam shaping strategies could be adopted to increase the detection efficiency, the easiest solution is to increase either the laser excitation power or exposure time. Conversely, this solution unavoidably leads to larger photodamage for the sample. This pivoting configuration requires specific optical designs and hardware modifications of standard SPIM setup. However, even if the integration of bulky optoelectronic devices can result complex, demanding and expensive, it is still time effective with respect to the post-processing alternatives to remove the striping. In addition, this latter approach is sometimes affected by reconstruction artifacts, especially in cases when the detected signal becomes comparable to background noise level[74].

Alternative optical methods do not guarantee instead a complete striping removal[168,169], while other pivoting approaches, not AOD-based[68,91,170] are not that fast enough to completely attenuate the shadowing[92].

Oher excitation strategies, as infrared or NIR, may provide several benefits because particularly effective in reduce scattering and light absorption in respect to visible illumination. Interestingly, no evidence of striping artifacts is present in literature in 2P LSFM[7,43,44,46,63,171]. However, it is worth noting that a 2P excitation line is surely less cost-effective than a 1P apparatus and a complete optical redesign is required in order to account for the different wavelength bands.

In conclusion, it is the biological goal of the experiment that should drive the choice of the method to employ in a LSM, looking for the best compromise to improve the image quality by striping reduction.

Going over this application, the AOD potentialities are not limited to fast pivoting. They can be properly used for multibeam generation by supplying multiple signals at different frequencies to the piezotransducer. The impinging beam will interact simultaneously with all the generated sound waves that propagate inside the crystal. This peculiar feature has been used in a DSLM to generate and control simultaneously two light sheets, showing the compatibility with dual confocal detection.

In particular, this AOD-based dual Gaussian beam excitation system was synchronized with an sCMOS camera working in single and dual-rolling shutter readout mode. In this work, it has been demonstrated how the dual-confocal detection regime achieved a twofold improvement in imaging speed, with respect to traditional confocal DLSM. This enhancement has been probed in samples with small background levels such as optically cleared mouse brains and in zebrafish larvae, verifying that the image contrast did not change.

Even though the multibeam generation with AODs has been demonstrated in this thesis[78,142] and in other recent applications[92], the number of targets simultaneously addressable is limited to few elements by the electronics necessary to generate multiple wave signals.

The last study performed on a light-sheet microscope demonstrated how a proper choice of the polarization state of the light excitation improved the detection of the fluorescence signal in a 2P DSLM. Depending on the excitation polarization direction, only a fraction of the fluorophores is photoselected for light absorption, determining the emission direction[105]. Therefore, given the particular geometrical design of a light-sheet microscope, the fluorescence anisotropy of a fluorophore plays a crucial role in the signal collection.

The proposed theoretical model predicted the optimal configuration for signal detection to be the one where the polarization direction of the excitation field laid on the plane orthogonal to the detection direction (indicated as horizontal polarization state). It has been indeed confirmed by the results obtained illuminating different fluorophores (fluorescein, EGFP and GCaMP6s) in different samples tested.

It is worth noting that in cases where the fluorophore population is randomly oriented and no particular constraints affect the rotational diffusion of the molecules, the global emitted signal will result homogeneously distributed. On the contrary, where there is a pre-existent spatial order of the fluorophores, e.g., due to their binding to spatially-oriented biological structures, the direction of emission will result globally anisotropic. In highly ordered structures this could produce artifacts in the acquired images and uneven signal levels.

With this experiment, all the different strategies proposed to correct the main drawbacks of light-sheet microscopy and to enhance its features for fast acquisitions, signal detection and obtain artifact-free imaging have been reported.

Together with these improvements, in this thesis, it has been proposed also a novel method for fast 3D photostimulation, based once again on the use of AODs. 2P optogenetic stimulation requires appropriate tools to efficiently access spatially distributed neuronal populations and sufficient speed to address them quasi-simultaneously.

However, commonly used galvo-based scanning approaches are characterized by long commutation times due to their intrinsic inertia[131]. Possible solutions are those provided by holographic illumination through SLM, widely implemented to draw random-access trajectories and simultaneously stimulate multiple regions[17]. However, the refresh rate required to modulate the stimulation pattern remains slow (~100Hz) and this approach is hindered by laser power splitting between the different targets. In this contest, AODs have been recently implemented in light-targeting applications for their fast dynamics and low refresh rate[146,147,172]. Indeed, even if with AODs it is not possible to simultaneously illuminate numerous targets (more than few units), those deflectors provide a pixel dwell time much shorter (10-30 μs)[140] than the rate for the illumination pattern reconfiguration of the parallel alternatives (~10ms)[16]. For this reason, AODs are suitable for near-simultaneous multi-site access in distant brain districts.

Nevertheless, AODs have not been used yet in volume photostimulation applications, especially those exploiting 2P excitation. This is due to non-uniform light power delivery when stimulating axially dislocated regions with equal light-addressing time. To counteract this drawback, a compensation software module is frequently employed, which tunes the driving signal frequency and intensity for each addressed point. However, even if the axial power distribution will result flattened across the volume, with this method[25] the intensity is reduced to the minimum value addressable. In other words, the peak intensity released in the centre of the axial scan is lowered down to the level obtained at the borders to keep the distribution constant.

In the last part of the thesis, a novel solution has been presented to face this issue, which raises the axial power delivery homogeneity towards the maximum value obtainable on the objective reference focal plane. To improve the power released within the pixel dwell time, the AODs were triggered several times, effectively multiplying the minimum energy deposited as a function of the addressed plane. This improvement enables 2PE applications with AODs that were precluded until now. In this regard, the 2P-photoactivation of optogenetic actuators in 3D in zebrafish larvae has been achieved, demonstrating the advantages provided by the proposed multi-trigger stimulation strategy.

In particular, the probability to optogenetically elicit an electrophysiological response of a neuronal cluster was increased in all the several planes addressed thanks to the prolonged light delivery time.

2P photostimulation of cellular clusters in dislocated planes represents an unprecedented result with AODs, obtained here for the first time by overcoming the loss in light transmission in axial scanning.

The method we devised allows to extend the axial range where the light is efficiently addressed with AODs, independently of the different optical parameters used, without affecting the point spread function of the system. Anyway, particular attention has to be paid to what concerns the chromatic dispersion undergone by the diffracted beam. Here, the dispersion felt by the broadband laser impinging the AOD diffraction grating is partially compensated by placing the second pair of AODs symmetrically opposite to the first one. In such a way, the distortion affecting the beam is counterbalanced globally increasing the symmetry of the beam profile. However, to further compensate the spatial dispersion and the group velocity dispersion additional upgrades would regard the involvement of specific achromatic optics or compensating systems[146]. Nonetheless, all the experimental tests have been carried out addressing a uniform lateral FOV.

Even if in this work it has been demonstrated for the first time the photoactivation of optogenetic actuators in zebrafish larvae by means of four AODs, the potentialities of this scanning head are not limited to this application. This device can be indeed applicable to fast 3D imaging, patterned photostimulation, multi-site and random-access light targeting experiments. Interestingly, this system has been designed as a self-standing system, coupled in this case with a fixed stage microscope specifically tailored for electrophysiology applications and microscopy in the infrared range. However, such a system can represent an add-on module complementing other existing microscopes with different characteristics.

Finally, the proof of principle of this innovative method resides in the AOD module optimization and in the advanced digital control system driving these devices. It means that this approach can represent an upgrade for all those setups that already leverage AODs for fast axial scanning and volume imaging. Indeed, the method is not constrained by the excitation wavelength used, and beyond a different calibration of the optical parameters, this solution can be implemented also for other AOD brands.

9. Conclusions and future perspectives

Illuminating the “black-box” and shedding light on its inner mechanism are the main goals of neuroscientists willing to understand brain physiology, pathology and anatomy. In this direction, proper technologies are necessary to disentangle the contribution of single neurons on cluster activation[15,148], to monitor the action potential propagation between interconnected areas[143,146] and to image three-dimensional structures with high resolution[119]. For these aims, instruments specifically non-invasive for the tissues, cell-selective, wide-ranging and effective are required.

The first step forward to reach these results has been done thanks to genetic engineering. It revolutionised neuroscience introducing a new generation of optical probes as the genetically encoded fluorescent indicators[114,121] and the optogenetic actuators[33,34]. With them, it is possible today to reach cell-specific targets, monitor the neurons activity by intracellular calcium transients, and make these cells photo-responsive to external triggers.

Through the parallel development of novel forms of microscopy[17,140], all-optical approaches became today the most valuable alternatives to patch-clamp electrophysiology, which has been seen as a gold standard for neuronal signal investigation until now[173]. Advanced optical microscopies are today commonly used to image wide-spread neuronal populations throughout the brain with high spatial resolution and contrast[174], but also to directly stimulate dislocated areas by light addressing specific pattern[20]. Hence the idea to develop a system that enables simultaneous optical imaging and cellular manipulation is straightforward and necessary to fully exploit the cellular specificity guaranteed by the new electrophysiology tools.

In this contest, LSFM represents an optimal solution for the imaging of large three-dimensional volumes[175] allowing to measure the spatial correlation between distributed neuronal population[58], to track single molecule in living tissue[60], to map the anatomy of mesoscale brains[67] and obtain functional recording over extended areas[2,62,174]. LSFM also guarantees fast optical sectioning of the sample[176] with a low level of photodamage and photo-bleaching with respect to other confocal-like techniques. The several approaches proposed in this thesis aim to further enhance the characteristics of this type of microscopy in terms of acquisition speed, contrast and signal collection. In parallel, the AOD-based beam pivoting solution provides artifacts-free images for quantitative analysis devoid of possible misunderstandings.

On the other hand, the state of the art of light stimulation provides a panorama of optical implementations to be used for optogenetic applications. However, mechanical constraints, low efficiency in light delivery and slow dynamics have often limited the applicability of those devices in three-dimensional 2P excitation experiments.

The scanning head configuration proposed in this thesis, once coupled with a 2P excitation line, provides deep optical access to large areas and the possibility of light handling for a customizable stimulation pattern. In particular, the use of four AODs supports superior dynamics in 3D light targeting with respect to other scanning methods, enabling effective random-access stimulation with microseconds dwell time. Moreover, with the proposed multitrigger stimulation method, common AOD drawbacks have been overcome, demonstrating for the first time the applicability of these devices in a 3D optogenetic stimulation experiment. Therefore, applying this device as an add-on to a whole-brain imaging system would open to numerous further possibilities.

The coexpression of opsin and a genetically encoded calcium indicator in transgenic animals would guarantee the simultaneous two-photon optogenetic activation and calcium imaging of the circuits. With this combination would be possible to understand the causality between the neuronal pathway activation and the outcome behaviours registered by calcium imaging[13]. Furthermore, thanks to the advancement in computation technology, it is possible today to rapidly analyse observed activity patterns with a distributed computing system[2]. Those systems would pave the way to closed-loop experiments, where the light targeting is driven by the neuron response to external stimuli. It means that the obtained functional maps could guide and orient the optical perturbations of a specific cluster of neurons and circuitry[4] for an even more specific understanding of brain responsivity.

Furthermore, all-optical electrophysiology has been used to probe specific physiologic and pathologic conditions of small mammals[177–179]. The neural dynamics stability derives from the tight coupling of excitatory and inhibitory signals[180]. From the asymmetry and imbalance of these signals, neural disorders arise, like epilepsy, schizophrenia and autism. For instance, by optogenetically stimulating specific brain areas it would be possible to interface with the propagation of paroxysmal activity in epileptic conditions[118].

In conclusion for all these experiments, high selectivity and specificity in light addressing is essential, together with the possibility of fast acquisition of extended volumes. With those characteristics will be finally possible to highlight the relationships between different neuronal populations dislocated over large areas[181] and have a global vision of the brain entanglement. The contribution brought with this thesis could represent a significant step forward for this long-distance goal.

10. References

1. WHO | World Health Organization. https://www.who.int/.

2. Freeman, J. *et al.* Mapping brain activity at scale with cluster computing. *Nat. Methods* 11, 941–950 (2014).

3. Wang, H. *et al.* High-speed mapping of synaptic connectivity using photostimulation in Channelrhodopsin-2 transgenic mice. *Proc. Natl. Acad. Sci. U. S. A.* 104, 8143–8148 (2007).

4. Vladimirov, N. *et al.* Brain-wide circuit interrogation at the cellular level guided by online analysis of neuronal function. *Nat. Methods* 15, 1117–1125 (2018).

5. Issa, F. A. *et al.* Neural circuit activity in freely behaving zebrafish (Danio rerio). *J. Exp. Biol.* 214, 1028–1038 (2011).

6. O’Connor, D. H., Huber, D. & Svoboda, K. Reverse engineering the mouse brain. *Nature* 461, 923–929 (2009).

7. Lemon, W. C. *et al.* Whole-central nervous system functional imaging in larval Drosophila. *Nat. Commun.* 6, (2015).

8. Bhattacharya, M., Ghosh, S., Malick, R. C., Patra, B. C. & Das, B. K. Therapeutic applications of zebrafish (Danio rerio) miRNAs linked with human diseases: A prospective review. *Gene* 679, 202–211 (2018).

9. Friedrich, R. W., Jacobson, G. A. & Zhu, P. Circuit Neuroscience in Zebrafish. *Curr. Biol.* 20, R371–R381 (2010).

10. Santoriello, C., Zon, L. I., Santoriello, C. & Zon, L. I. Hooked ! Modeling human disease in zebrafish Find the latest version : Science in medicine Hooked ! Modeling human disease in zebrafish. *J. Clin. Invest.* 122, 2337–2343 (2012).

11. Costantini, I. *et al.* Large-scale, cell-resolution volumetric mapping allows layer-specific investigation of human brain cytoarchitecture. *Biomed. Opt. Express* 12, 3684 (2021).

12. Pesce, L., Scardigli, M., Gavryusev, V., bioRxiv, A. L.- & 2021, undefined. 3D molecular phenotyping of cleared human brain tissues with light-sheet fluorescence microscopy. *biorxiv.org*.

13. dal Maschio, M., Donovan, J. C., Helmbrecht, T. O. & Baier, H. Linking

Neurons to Network Function and Behavior by Two-Photon Holographic Optogenetics and Volumetric Imaging. *Neuron* 94, 774-789.e5 (2017).

14. Chen, I.-W. *et al.* In Vivo Submillisecond Two-Photon Optogenetics with Temporally Focused Patterned Light. *J. Neurosci.* 39, 3484–3497 (2019).

15. Douglass, A. D., Kraves, S., Deisseroth, K., Schier, A. F. & Engert, F. Escape Behavior Elicited by Single, Channelrhodopsin-2-Evoked Spikes in Zebrafish Somatosensory Neurons. *Curr. Biol.* 18, 1133–1137 (2008).

16. Ronzitti, E. *et al.* Recent advances in patterned photostimulation for optogenetics. *J. Opt. (United Kingdom)* 19, (2017).

17. Ronzitti, E., Emiliani, V. & Papagiakoumou, E. Methods for three-dimensional all-optical manipulation of neural circuits. *Front. Cell. Neurosci.* 12, (2018).

18. Carrillo-Reid, L., Yang, W., Kang Miller, J. E., Peterka, D. S. & Yuste, R. Imaging and Optically Manipulating Neuronal Ensembles. *Annu. Rev. Biophys.* 46, 271–293 (2017).

19. Zhang, Z., Russell, L. E., Packer, A. M., Gauld, O. M. & Häusser, M. Closed-loop all-optical interrogation of neural circuits in vivo. *Nat. Methods* 15, 1037–1040 (2018).

20. Emiliani, V., Cohen, A. E., Deisseroth, K. & Häusser, M. All-optical interrogation of neural circuits. *J. Neurosci.* 35, 13917–13926 (2015).

21. Helassa, N., Podor, B., Fine, A. & Török, K. Design and mechanistic insight into ultrafast calcium indicators for monitoring intracellular calcium dynamics. *Sci. Rep.* 6, 1–14 (2016).

22. Akerboom, J. *et al.* Optimization of a GCaMP calcium indicator for neural activity imaging. *J. Neurosci.* 32, 13819–13840 (2012).

23. Dana, H. *et al.* High-performance calcium sensors for imaging activity in neuronal populations and microcompartments. *Nat. Methods* 16, 649–657 (2019).

24. Grewe, B. F., Langer, D., Kasper, H., Kampa, B. M. & Helmchen, F. High-speed in vivo calcium imaging reveals neuronal network activity with near-millisecond precision. *Nat. Methods* 7, 399–405 (2010).

25. Katona, G. *et al.* Fast two-photon in vivo imaging with three-dimensional

random-access scanning in large tissue volumes. *Nat. Methods* 9, 201–208 (2012).

26. Zipfel, W. R., Williams, R. M. & Webb, W. W. Nonlinear magic: Multiphoton microscopy in the biosciences. *Nat. Biotechnol.* 21, 1369–1377 (2003).

27. Duemani Reddy, G., Kelleher, K., Fink, R. & Saggau, P. Three-dimensional random access multiphoton microscopy for functional imaging of neuronal activity. *Nat. Neurosci.* 11, 713–720 (2008).

28. Helmchen, F. & Denk, W. Deep tissue two-photon microscopy. *Nat. Methods* 2, 932–940 (2005).

29. Kobat, D., Horton, N. G. & Xu, C. In vivo two-photon microscopy to 1.6-mm depth in mouse cortex. *J. Biomed. Opt.* 16, 106014 (2011).

30. Ingaramo, M. *et al.* Two-photon excitation improves multifocal structured illumination microscopy in thick scattering tissue. *Proc. Natl. Acad. Sci. U. S. A.* 111, 5254–5259 (2014).

31. Yang, W., Carrillo-Reid, L., Bando, Y., Peterka, D. S. & Yuste, R. Simultaneous two-photon imaging and two-photon optogenetics of cortical circuits in three dimensions. *Elife* 7, 1–21 (2018).

32. Truong, T. V., Supatto, W., Koos, D. S., Choi, J. M. & Fraser, S. E. Deep and fast live imaging with two-photon scanned light-sheet microscopy. *Nat. Methods* 8, 757–762 (2011).

33. Deisseroth, K. Optogenetics. *Nat. Methods* 8, 26–29 (2011).

34. Yizhar, O., Fenno, L. E., Davidson, T. J., Mogri, M. & Deisseroth, K. Optogenetics in Neural Systems. *Neuron* 71, 9–34 (2011).

35. Prakash, R. *et al.* Two-photon optogenetic toolbox for fast inhibition, excitation and bistable modulation. *Nat. Methods* 9, 1171–1179 (2012).

36. Packer, A. M. *et al.* Two-photon optogenetics of dendritic spines and neural circuits. *Nat. Methods* 9, 1202–1205 (2012).

37. Chen, I. W. *et al.* Parallel holographic illumination enables sub-millisecond two-photon optogenetic activation in mouse visual cortex in vivo. *bioRxiv* 1–21 (2018) doi:10.1101/250795.

38. Girkin, J. M. & Carvalho, M. T. The light-sheet microscopy revolution. *J.*

Opt. (United Kingdom) **20**, (2018).

39. Gualda, E. J., Andilla, J., Olarte, O. E. & Loza-Alvarez, P. Light-sheet microscopy: a tutorial. *Adv. Opt. Photonics, Vol. 10, Issue 1, pp. 111-179* **10**, 111–179 (2018).

40. Huisken, J., Swoger, J., Del Bene, F., Wittbrodt, J. & Stelzer, E. H. K. Optical sectioning deep inside live embryos by selective plane illumination microscopy. *Science (80-.).* **305**, 1007–1009 (2004).

41. Stelzer, E. H. K. *et al.* Light sheet fluorescence microscopy. *Nat. Rev. Methods Prim. 2021 11* **1**, 1–25 (2021).

42. Yuste, R. Fluorescence microscopy today. *Nat. Methods* **2**, 902–904 (2005).

43. Lavagnino, Z., Cella Zanacchi, F., Ronzitti, E. & Diaspro, A. Two-photon excitation selective plane illumination microscopy (2PE-SPIM) of highly scattering samples: characterization and application. *Opt. Express* **21**, 5998 (2013).

44. Cella Zanacchi, F. *et al.* Two-photon fluorescence excitation within a light sheet based microscopy architecture. *Multiphot. Microsc. Biomed. Sci. XI* **7903**, 79032W (2011).

45. Lavagnino, Z. *et al.* 4D (x-y-z-t) imaging of thick biological samples by means of Two-Photon inverted Selective Plane Illumination Microscopy (2PE-iSPIM). *Sci. Rep.* **6**, 1–9 (2016).

46. Wolf, S. *et al.* Whole-brain functional imaging with two-photon light-sheet microscopy. *Nat. Methods* **12**, 379–380 (2015).

47. Palero, J., Santos, S. I. C. O., Artigas, D. & Loza-Alvarez, P. A simple scanless two-photon fluorescence microscope using selective plane illumination. *Opt. Express* **18**, 8491 (2010).

48. Denk, W., Strickler, J. H. & Webb, W. W. Two-photon laser scanning fluorescence microscopy. *Science (80-.).* **248**, 73–76 (1990).

49. Wang, K., Horton, N. G. & Xu, C. Going Deep: Brain Imaging with Multi-Photon Microscopy. *Opt. Photonics News* **24**, 32 (2013).

50. Kerr, J. N. D. & Denk, W. Imaging in vivo : watching the brain in action. **9**, 195–205 (2008).

51. Svoboda, K. & Yasuda, R. Principles of Two-Photon Excitation Microscopy and Its Applications to Neuroscience. *Neuron* 50, 823–839 (2006).

52. Göppert-Mayer, M. Über Elementarakte mit zwei Quantensprüngen. *Ann. Phys.* 401, 273–294 (1931).

53. Abella, I. D. Optical Double-Photon Absorption in Cesium Vapor. *Phys. Rev. Lett.* 9, 453 (1962).

54. Benninger, R. K. P. & Piston, D. W. Two-photon excitation microscopy for unit 4.11 the study of living cells and tissues. *Curr. Protoc. Cell Biol.* (2013) doi:10.1002/0471143030.CB0411S59.

55. Young, A. T. 8 Rayleigh scattering - A T Young - Appl Opt 1981. *Appl. Opt.* 20, 533–535 (1981).

56. VOIE, A. H., BURNS, D. H. & SPELMAN, F. A. Orthogonal-plane fluorescence optical sectioning: Three-dimensional imaging of macroscopic biological specimens. *J. Microsc.* 170, 229–236 (1993).

57. Chatterjee, K., Pratiwi, F. W., Wu, F. C. M., Chen, P. & Chen, B. C. Recent Progress in Light Sheet Microscopy for Biological Applications. *Appl. Spectrosc.* 72, 1137–1169 (2018).

58. Keller, P. J., Ahrens, M. B. & Freeman, J. Light-sheet imaging for systems neuroscience. *Nat. Methods* 12, 27–29 (2014).

59. Keller, P. J. & Dodt, H. U. Light sheet microscopy of living or cleared specimens. *Curr. Opin. Neurobiol.* 22, 138–143 (2012).

60. Ritter, J. G., Veith, R., Veenendaal, A., Siebrasse, J. P. & Kubitscheck, U. Light sheet microscopy for single molecule tracking in living tissue. *PLoS One* 5, 1–9 (2010).

61. Royer, L. A. *et al.* Adaptive light-sheet microscopy for long-term, high-resolution imaging in living organisms. *Nat. Biotechnol.* 34, 1267–1278 (2016).

62. Keller, P. J. & Ahrens, M. B. Visualizing whole-brain activity and development at the single-cell level using light-sheet microscopy. *Neuron* 85, 462–483 (2015).

63. Tomer, R., Khairy, K., Amat, F. & Keller, P. J. Quantitative high-speed imaging of entire developing embryos with simultaneous multiview light-

sheet microscopy. *Nat. Methods* 9, 755–763 (2012).

64. Wan, Y., McDole, K. & Keller, P. J. Light-sheet microscopy and its potential for understanding developmental processes. *Annu. Rev. Cell Dev. Biol.* 35, 655–681 (2019).

65. Weber, M. & Huisken, J. Light sheet microscopy for real-time developmental biology. *Curr. Opin. Genet. Dev.* 21, 566–572 (2011).

66. Huisken, J. & Stainier, D. Y. R. Selective plane illumination microscopy techniques in developmental biology. *Development* 136, 1963–1975 (2009).

67. Tomer, R. *et al.* SPED Light Sheet Microscopy: Fast Mapping of Biological System Structure and Function. *Cell* 163, 1796–1806 (2015).

68. Pampaloni, F., Ansari, N., Girard, P. & Stelzer, E. H. K. Light sheet-based fluorescence microscopy (LSFM) reduces phototoxic effects and provides new means for the modern life sciences. *Opt. InfoBase Conf. Pap.* 8086, 1–6 (2011).

69. Engelbrecht, C. J. & Stelzer, E. H. Resolution enhancement in a light-sheet-based microscope (SPIM). *Opt. Lett.* 31, 1477 (2006).

70. Santi, P. A. Light sheet fluorescence microscopy: A review. *J. Histochem. Cytochem.* 59, 129–138 (2011).

71. Dodt, H. U. *et al.* Ultramicroscopy: Three-dimensional visualization of neuronal networks in the whole mouse brain. *Nat. Methods* 4, 331–336 (2007).

72. Keller, P. J., Schmidt, A. D., Wittbrodt, J. & Stelzer, E. H. K. Reconstruction of zebrafish early embryonic development by scanned light sheet microscopy. *Science (80-.).* 322, 1065–1069 (2008).

73. Lvarez, P. A. L. O. Z. A. Light-sheet microscopy : a tutorial. 10, 111–179 (2018).

74. Ricci, P. *et al.* Removing striping artifacts in light-sheet fluorescence microscopy: A review. *Prog. Biophys. Mol. Biol.* (2021) doi:10.1016/J.PBIOMOLBIO.2021.07.003.

75. Silvestri, L., Bria, A., Sacconi, L., Iannello, G. & Pavone, F. S. Confocal light sheet microscopy: micron-scale neuroanatomy of the entire mouse

brain. *Opt. Express* 20, 20582 (2012).

76. Medeiros, G. De *et al.* Confocal multiview light-sheet microscopy. *Nat. Commun.* 6, 1–8 (2015).

77. Fahrbach, F. O. & Rohrbach, A. Propagation stability of self-reconstructing Bessel beams enables contrast-enhanced imaging in thick media. *Nat. Commun.* 3, (2012).

78. Gavryusev, V. *et al.* Dual-beam confocal light-sheet microscopy via flexible acousto-optic deflector. *J. Biomed. Opt.* 24, 1 (2019).

79. Mickoleit, M. *et al.* High-resolution reconstruction of the beating zebrafish heart. *Nat. Methods* 11, 919–922 (2014).

80. Costantini, I. *et al.* A versatile clearing agent for multi-modal brain imaging. *Sci. Rep.* 5, 1–9 (2015).

81. Silvestri, L., Costantini, I., Sacconi, L. & Pavone, F. S. Clearing of fixed tissue: a review from a microscopist's perspective. *J. Biomed. Opt.* 21, 081205 (2016).

82. Ueda, H. R. *et al.* Tissue clearing and its applications in neuroscience. *Nat. Rev. Neurosci.* 21, 61–79 (2020).

83. Tainaka, K. *et al.* Whole-body imaging with single-cell resolution by tissue decolorization. *Cell* 159, 911–924 (2014).

84. Müllenbroich, M. C. *et al.* High-fidelity imaging in brain-wide structural studies using light-sheet microscopy. *eNeuro* 5, (2018).

85. Durnin, J., Miceli, J. & Eberly, J. H. Diffraction-free beams. *Phys. Rev. Lett.* 58, 1499–1501 (1987).

86. Herman, R. M. & Wiggins, T. A. Production and uses of diffractionless beams. *J. Opt. Soc. Am. A* 8, 932 (1991).

87. Ding, Z., Ren, H., Zhao, Y., Nelson, J. S. & Chen, Z. High-resolution optical coherence tomography over a large depth range with an axicon lens. *Opt. Lett.* 27, 243 (2002).

88. Fahrbach, F. O., Gurchenkov, V., Alessandri, K., Nassoy, P. & Rohrbach, A. Self-reconstructing sectioned Bessel beams offer submicron optical sectioning for large fields of view in light-sheet microscopy. *Opt. Express*

21, 11425 (2013).

89. Planchon, T. A. *et al.* Bessel beam plane illumination. *Nat. Methods* **8**, 417–423 (2011).

90. Fahrbach, F. O., Simon, P. & Rohrbach, A. Microscopy with self-reconstructing beams. *Nat. Photonics* **4**, 780–785 (2010).

91. Huisken, J. & Stainier, D. Y. R. Even fluorescence excitation by multidirectional selective plane illumination microscopy (mSPIM). *Opt. Lett.* **32**, 2608 (2007).

92. Sancataldo, G. *et al.* Flexible multi-beam light-sheet fluorescence microscope for live imaging without striping artifacts. *Front. Neuroanat.* **13**, 1–8 (2019).

93. Glaser, A. K. *et al.* Multidirectional digital scanned light-sheet microscopy enables uniform fluorescence excitation and contrast-enhanced imaging. *Sci. Rep.* **8**, 2–12 (2018).

94. Uddin, M. S., Lee, H. K., Preibisch, S. & Tomancak, P. Restoration of uneven illumination in light sheet microscopy images. *Microsc. Microanal.* **17**, 607–613 (2011).

95. Leischner, U., Schierloh, A., Zieglgänsberger, W. & Dodt, H. U. Formalin-induced fluorescence reveals cell shape and morphology in biological tissue samples. *PLoS One* **5**, (2010).

96. Münch, B., Trtik, P., Marone, F. & Stampanoni, M. Stripe and ring artifact removal with combined wavelet-Fourier filtering. *EMPA Act.* **17**, 34–35 (2009).

97. Swoger, J., Verveer, P., Greger, K., Huisken, J. & Stelzer, E. H. K. Multi-view image fusion improves resolution in three-dimensional microscopy. *Opt. Express* **15**, 8029 (2007).

98. Preibisch, S., Saalfeld, S., Schindelin, J. & Tomancak, P. Software for bead-based registration of selective plane illumination microscopy data. *Nat. Methods* **7**, 418–419 (2010).

99. Zhang, S. *et al.* Mechanism of polarization-induced single-photon fluorescence enhancement. *J. Chem. Phys.* **133**, 1–4 (2010).

100. Vivas, M. G., De Boni, L., Bretonniere, Y., Andraud, C. & Mendonca, C. R.

Polarization effect on the two-photon absorption of a chiral compound. *Opt. Express* 20, 18600 (2012).

101. Nag, A. & Goswami, D. Polarization induced control of single and two-photon fluorescence. *J. Chem. Phys.* 132, (2010).

102. Mojzisova, H. *et al.* Polarization-sensitive two-photon microscopy study of the organization of liquid-crystalline DNA. *Biophys. J.* 97, 2348–2357 (2009).

103. O'Holleran, K. & Shaw, M. Polarization effects on contrast in structured illumination microscopy. *Opt. Lett.* 37, 4603 (2012).

104. de Vito, G. *et al.* Effects of excitation light polarization on fluorescence emission in two-photon light-sheet microscopy. *Biomed. Opt. Express* 11, 4651 (2020).

105. Lakowicz, J. Principles of fluorescence spectroscopy. (2013) doi:10.1007/978-0-387-46312-4.

106. Brasselet, S. Polarization-resolved nonlinear microscopy: application to structural molecular and biological imaging. *Adv. Opt. Photonics* 3, 205 (2011).

107. Poledna, J. Mechanism of intracellular calcium transients. *Gen. Physiol. Biophys.* 10, 475–484 (1991).

108. Zhong, C. & Schleifenbaum, J. Genetically Encoded Calcium Indicators: A New Tool in Renal Hypertension Research. *Front. Med.* 6, 1–6 (2019).

109. Russell, J. T. Imaging calcium signals in vivo: A powerful tool in physiology and pharmacology. *Br. J. Pharmacol.* 163, 1605–1625 (2011).

110. McCombs, J. E. & Palmer, A. E. Measuring calcium dynamics in living cells with genetically encodable calcium indicators. *Methods* 46, 152–159 (2008).

111. Grienberger, C. & Konnerth, A. Imaging Calcium in Neurons. *Neuron* 73, 862–885 (2012).

112. Adams, S. R. How calcium indicators work. *Cold Spring Harb. Protoc.* 5, (2010).

113. Göbel, W. & Helmchen, F. In vivo calcium imaging of neural network

function. *Physiology* 22, 358–365 (2007).

114. Broussard, G. J., Liang, R. & Tian, L. Monitoring activity in neural circuits with genetically encoded indicators. *Front. Mol. Neurosci.* 7, (2014).

115. Mank, M. & Griesbeck, O. Genetically encoded calcium indicators. *Chem. Rev.* 108, 1550–1564 (2008).

116. Direnberger, stephan *et al.* Biocompatibility of a genetically encoded calcium indicator in a transgenic mouse model. (2012) doi:10.1038/ncomms2035.

117. Chen, T. W. *et al.* Ultrasensitive fluorescent proteins for imaging neuronal activity. *Nature* 499, 295–300 (2013).

118. Turrini, L. *et al.* Optical mapping of neuronal activity during seizures in zebrafish. *Sci. Rep.* 7, 1–12 (2017).

119. Dunn, T. W. *et al.* Brain-wide mapping of neural activity controlling zebrafish exploratory locomotion. *Elife* 5, 1–29 (2016).

120. Lu, R. *et al.* Rapid mesoscale volumetric imaging of neural activity with synaptic resolution. *Nat. Methods* 17, 291–294 (2020).

121. Lin, M. Z. & Schnitzer, M. J. Genetically encoded indicators of neuronal activity. 19, (2016).

122. Nagel, G. *et al.* Channelrhodopsin-1: A light-gated proton channel in green algae. *Science (80-.).* 296, 2395–2398 (2002).

123. Lin, J. Y., Knutsen, P. M., Muller, A., Kleinfeld, D. & Tsien, R. Y. ReaChR: A red-shifted variant of channelrhodopsin enables deep transcranial optogenetic excitation. *Nat. Neurosci.* 16, 1499–1508 (2013).

124. Peter, J. & Tank, D. W. Two-photon excitation of channelrhodopsin-2. 1–6 (2009).

125. Nagel, G. *et al.* Cation-Selective Membrane Channel. *Pnas* 100, 13940–13945 (2003).

126. Klapoetke, N. C. *et al.* Independent optical excitation of distinct neural populations. *Nat. Methods* 11, 338–346 (2014).

127. Grossman, N. *et al.* Multi-site optical excitation using ChR2 and micro-LED array. *J. Neural Eng.* 7, (2010).

128. Lin, J. Y. A user's guide to channelrhodopsin variants: Features, limitations and future developments. *Exp. Physiol.* 96, 19–25 (2011).

129. Miesenböck, G. & Kevrekidis, I. G. Optical imaging and control of genetically designated neurons in functioning circuits. *Annu. Rev. Neurosci.* 28, 533–563 (2005).

130. Grewe, B. F. & Helmchen, F. Optical probing of neuronal ensemble activity. *Curr. Opin. Neurobiol.* 19, 520–529 (2009).

131. Petreanu, L., Mao, T., Sternson, S. M. & Svoboda, K. The subcellular organization of neocortical excitatory connections. *Nature* 457, 1142–1145 (2009).

132. Gasparini, S. & Magee, J. C. State-Dependent Dendritic Computation in Hippocampal CA1 Pyramidal Neurons. *J. Neurosci.* 26, 2088–2100 (2006).

133. Rickgauer, J. P. & Tank, D. W. Two-photon excitation of channelrhodopsin-2 at saturation. *Proc. Natl. Acad. Sci.* 106, 15025–15030 (2009).

134. Wang, S. *et al.* All optical interface for parallel, remote, and spatiotemporal control of neuronal activity. *Nano Lett.* 7, 3859–3863 (2007).

135. Zhu, P., Fajardo, O., Shum, J., Zhang Schärer, Y. P. & Friedrich, R. W. High-resolution optical control of spatiotemporal neuronal activity patterns in zebrafish using a digital micromirror device. *Nat. Protoc.* 7, 1410–1425 (2012).

136. Stirman, J. N. *et al.* Real-time multimodal optical control of neurons and muscles in freely behaving Caenorhabditis elegans. *Nat. Methods* 8, 153–158 (2011).

137. Chaigneau, E. *et al.* Two-photon holographic stimulation of ReaChR. *Front. Cell. Neurosci.* 10, (2016).

138. Papagiakoumou, E. *et al.* Scanless two-photon excitation of channelrhodopsin-2. *Nat. Methods* 7, 848–854 (2010).

139. Picot, A. *et al.* Temperature Rise under Two-Photon Optogenetic Brain Stimulation. *Cell Rep.* 24, 1243-1253.e5 (2018).

140. Duocastella, M., Surdo, S., Zunino, A., Diaspro, A. & Saggau, P. Acousto-optic systems for advanced microscopy. *JPhys Photonics* 3, (2021).

141. Duocastella, M. *et al.* Fast Inertia-Free Volumetric Light-Sheet Microscope. *ACS Photonics* 4, 1797–1804 (2017).

142. Ricci, P. *et al.* Fast multi-directional DSLM for confocal detection without striping artifacts. *Biomed. Opt. Express* 11, 3111 (2020).

143. Cotton, R. J., Froudarakis, E., Storer, P., Saggau, P. & Tolias, A. S. Three-dimensional mapping of microcircuit correlation structure. *Front. Neural Circuits* 7, 1–13 (2013).

144. Fernández-Alfonso, T. *et al.* Monitoring synaptic and neuronal activity in 3D with synthetic and genetic indicators using a compact acousto-optic lens two-photon microscope. *J. Neurosci. Methods* 222, 69–81 (2014).

145. Szalay, G. *et al.* Fast three-dimensional two-photon scanning methods for studying neuronal physiology on cellular and network level. *Orv. Hetil.* 156, 2120–2126 (2015).

146. Szalay, G. *et al.* Fast 3D Imaging of Spine, Dendritic, and Neuronal Assemblies in Behaving Animals. *Neuron* 92, 723–738 (2016).

147. Marosi, M., Szalay, G., Katona, G. & Rózsa, B. High-speed, random-access multiphoton microscopy for monitoring synaptic and neuronal activity in 3D in behaving animals. *Neuromethods* 148, 335–362 (2019).

148. Iyer, V., Hoogland, T. M. & Saggau, P. Fast functional imaging of single neurons using random-access multiphoton (RAMP) microscopy. *J. Neurophysiol.* 95, 535–545 (2006).

149. Otsu, Y. *et al.* Optical monitoring of neuronal activity at high frame rate with a digital random-access multiphoton (RAMP) microscope. *J. Neurosci. Methods* 173, 259–270 (2008).

150. Reddy, G. D. & Saggau, P. Fast three-dimensional laser scanning scheme using acousto-optic deflectors. *J. Biomed. Opt.* 10, 064038 (2005).

151. You, A., Be, M. A. Y. & In, I. Instrumentation of a compact random- access photostimulator based on acousto- optic deflectors. 025116, (2016).

152. Wang, K. *et al.* Precise spatiotemporal control of optogenetic activation using an acousto-optic device. *PLoS One* 6, (2011).

153. Guenthner, C. J., Miyamichi, K., Yang, H. H., Heller, H. C. & Luo, L. Permanent genetic access to transiently active neurons via TRAP:

Targeted recombination in active populations. *Neuron* 78, 773–784 (2013).

154. Vladimirov, N. *et al.* Light-sheet functional imaging in fictively behaving zebrafish. *Nat. Methods* 11, 883–884 (2014).

155. Müllenbroich, M. C. *et al.* Bessel Beam Illumination Reduces Random and Systematic Errors in Quantitative Functional Studies Using Light-Sheet Microscopy. *Front. Cell. Neurosci.* 12, 1–12 (2018).

156. Maderspacher, F. & Nüsslein-Volhard, C. Formation of the adult pigment pattern in zebrafish requires leopard and obelix dependent cell interactions. *Development* 130, 3447–3457 (2003).

157. WESTERFIELD & M. The Zebrafish Book : A Guide for the Laboratory Use of Zebrafish. *http://zfin.org/zf_info/zfbook/zfbk.html* (2000).

158. Dunn, T. W. *et al.* Neural Circuits Underlying Visually Evoked Escapes in Larval Zebrafish. *Neuron* 89, 613–628 (2016).

159. Müllenbroich, M. C. *et al.* Comprehensive optical and data management infrastructure for high-throughput light-sheet microscopy of whole mouse brains. *Neurophotonics* 2, 041404 (2015).

160. Gałecki, A. & Burzykowski, T. *Linear Mixed-Effects Models Using R*. (Springer New York, 2013). doi:10.1007/978-1-4614-3900-4.

161. Searle, S. R., Speed, F. M. & Milliken, G. A. Population marginal means in the linear model: An alternative to least squares means. *Am. Stat.* 34, 216–221 (1980).

162. Berkson, J. Application of the Logistic Function to Bio-Assay. *J. Am. Stat. Assoc.* 39, 357–365 (1944).

163. Keller, P. J. *et al.* Fast, high-contrast imaging of animal development with scanned light sheet-based structured-illumination microscopy. *Nat. Methods* 7, 637–642 (2010).

164. Bando, Y., Sakamoto, M., Kim, S., Ayzenshtat, I. & Yuste, R. Comparative Evaluation of Genetically Encoded Voltage Indicators. *Cell Rep.* 26, 802-813.e4 (2019).

165. Storace, D. *et al.* Toward Better Genetically Encoded Sensors of Membrane Potential. *Trends Neurosci.* 39, 277–289 (2016).

166. Sasaki, M., Kawahito, S., Mase, M. & Tadokoro, Y. A wide dynamic range CMOS image sensor with multiple short-time exposures. *Proc. IEEE Sensors* 2, 967–972 (2004).

167. Baumgart, E. & Kubitscheck, U. Scanned light sheet microscopy with confocal slit detection. *Opt. Express* 20, 21805 (2012).

168. Liu, Y., Lauderdale, J. D. & Kner, P. Stripe artifact reduction for digital scanned structured illumination light sheet microscopy. *Opt. Lett.* 44, 2510 (2019).

169. Dean, K. M. *et al.* Diagonally Scanned Light-Sheet Microscopy for Fast Volumetric Imaging of Adherent Cells. *Biophys. J.* 110, 1456–1465 (2016).

170. Di Battista, D., Merino, D., Zacharakis, G., Loza-Alvarez, P. & Olarte, O. E. Enhanced light sheet elastic scattering microscopy by using a supercontinuum laser. *Methods Protoc.* 2, 1–12 (2019).

171. Lavagnino, Z. *et al.* 4D (x-y-z-t) imaging of thick biological samples by means of Two-Photon inverted Selective Plane Illumination Microscopy (2PE-iSPIM). *Sci. Rep.* 6, 1–9 (2016).

172. Sakaki, K. D. R., Podgorski, K., Dellazizzo Toth, T. A., Coleman, P. & Haas, K. Comprehensive Imaging of Sensory-Evoked Activity of Entire Neurons Within the Awake Developing Brain Using Ultrafast AOD-Based Random-Access Two-Photon Microscopy. *Front. Neural Circuits* 14, 1–18 (2020).

173. Verkhratsky, A., protocols, V. P.-P. methods and & 2014, undefined. History of electrophysiology and the patch clamp. *Springer* 1183,.

174. Ahrens, M. B., Orger, M. B., Robson, D. N., Li, J. M. & Keller, P. J. Whole-brain functional imaging at cellular resolution using light-sheet microscopy. *Nat. Methods* 10, 413–420 (2013).

175. Hillman, E. M. C., Voleti, V., Li, W. & Yu, H. Light-Sheet Microscopy in Neuroscience. *Annu. Rev. Neurosci.* 42, 295–313 (2019).

176. Daetwyler, S. & Huisken, J. Fast fluorescence microscopy with light sheets. *Biol. Bull.* 231, 14–25 (2016).

177. Adam, Y. All-optical electrophysiology in behaving animals. *J. Neurosci. Methods* 353, 109101 (2021).

178. Hochbaum, D. R. *et al.* All-optical electrophysiology in mammalian neurons

using engineered microbial rhodopsins. *Nat. Methods 2014 118* 11, 825–833 (2014).

179. Werley, C. A. *et al.* All-optical electrophysiology for disease modeling and pharmacological characterization of neurons. *Curr. Protoc. Pharmacol.* 2017, 11.20.1-11.20.24 (2017).

180. Fan, L. All-Optical Electrophysiology of Excitation and Inhibition in Neural Circuits. (2019).

181. Adoff, M. D. *et al.* The functional organization of excitatory synaptic input to place cells. *Nat. Commun.* 12, 1–15 (2021).

Acknowledgements

I would like to thank Francesco Pavone - the supervisor of my thesis - for the opportunity that he gave me and for having allowed me to reach this goal. I would like to thank him for the trust expressed in recent years and the continuous esteem and appreciation showed towards me.

I would like to thank Ludovico Silvestri - the co-supervisor of my thesis - for the continuous support and patience shown over the years. I would like to thank him for having been a reference for me, for having been always available for any doubt, uncertainty, perplexity and for having given me plenty of advice. I would like to thank him for everything he taught me.

I would like to thank Dr. Martì Duocastella and Dr. Ulrich Kubitscheck for having read and revised my thesis. I would like to thank them for their time and availability.